EXPERIMENTAL STUDY OF ^{19}C VIA GAMMA-RAY LIFETIME AND KNOCKOUT MEASUREMENTS

By

Kenneth Aaron Whitmore

A DISSERTATION

Submitted to
Michigan State University
in partial fulfillment of the requirements
for the degree of

Physics — Doctor of Philosophy

2016

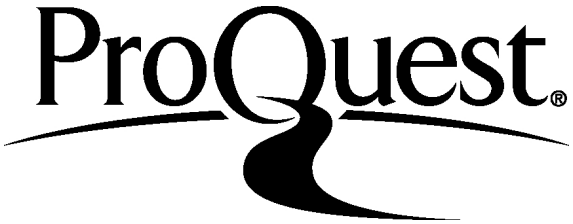

ABSTRACT

EXPERIMENTAL STUDY OF ^{19}C VIA GAMMA-RAY LIFETIME AND KNOCKOUT MEASUREMENTS

By

Kenneth Aaron Whitmore

The nuclear halo is a unique phenomenon occurring at the limit of nuclear stability. Previous studies have established an enhanced low-energy electric dipole strength as a characteristic feature of halo nuclei. Despite such extensive work on the electric response, there is no experimental evidence on the magnetic response of halos. A gamma-ray lifetime measurement has been performed on the one-neutron halo nucleus ^{19}C, which represents the first measurement of a magnetic transition between bound states in a halo nucleus. This measurement also serves as a means to constrain the spin-parities of the states in ^{19}C. The lifetime of the first excited state in ^{19}C has been measured using both the line-shape method and the Recoil Distance Method. The deduced $B(M1; 3/2^+ \rightarrow 1/2^+)$ transition strength represents one of the most hindered $M1$ transitions among light nuclei. The result is compared to large-scale shell model calculations, which predict a strong hindrance due to the degeneracy of the $1s_{1/2}$ and $0d_{5/2}$ neutron orbitals. The result establishes the $M1$ hindrance as another feature of halo nuclei which are dominated by s-wave configurations.

The one-proton knockout reaction of ^{20}N is used to study the structure of the bound states in ^{19}C as well as the ground state in ^{20}N. Eikonal reaction model calculations are compared to the measured inclusive cross section. The small inclusive cross section indicates the significant difference between the wave functions of the low-lying states of ^{20}N and ^{19}C. The results support the spin-parity assignment of the excited state in ^{19}C obtained from the lifetime measurement. The coupling of the proton $0p_{1/2}$ orbital to a $5/2^+$ core within ^{20}N

is suggested from large-scale shell-model calculations performed for the 2^- ground state in ^{20}N, indicating that the degeneracy of the $1s_{1/2}$ and $0d_{5/2}$ orbitals that occurs in ^{19}C does not persist in ^{20}N. Both the lifetime and knockout reaction analyses support the exclusion of a bound $5/2^+$ state in ^{19}C. The combined results present a consistent picture of the structure of ^{19}C and provide important data to establish trend of the $1s_{1/2}$ and $0d_{5/2}$ single particle energies for the $N = 13$ isotones.

ACKNOWLEDGMENTS

It is impossible for me to fully express my gratitude to all of the people who have contributed to my success at MSU. I will try to use this space to give as much thanks as I can.

First, I would like to express my deepest gratitude to my research advisor, Prof. Hironori Iwasaki. He has inspired and challenged me, and I know I am a better scientist because of him. His endless patience and optimism have kept me going, even when I get bogged down in stress of work. I would also like to thank the members of my thesis committee, Profs. Morten Hjorth-Jensen, Artemis Spyrou, Carl Schmidt, and Megan Donahue. They have provided extremely valuable insight over the years. I must also acknowledge the contributions of many other scientists at the NSCL, including the staff scientists who kept this and other experiments running smoothly, as well as the professors whose classes I've had the privelege of taking.

I also give credit to my professors at William Jewell College. They encouraged me to explore many research opportunities, and ultimately allowed me to discover my enthusiasm for nuclear physics.

I am especially grateful to the various members of the Lifetime group: Antoine Lemasson, Duane Smalley, Nobuyuki Kobayashi, Charles Loelius, Rob Elder, Mara Grinder, and of course, Christopher Morse, who served as an excellent leader as the pioneer Lifetime graduate student. I am also grateful to the members of the Gamma group who provided me with technical experience and expertise. I also am very grateful for all of the other MSU graduate students who made living in Michigan fun, and with whom I am very lucky to be friends.

Finally, I would like to thank my family, who has been nothing but supportive through all

of my educational endeavors. Our weekly chats helped to keep me sane and lifted my spirits during the most difficult times. Without their support, none of this would be possible.

TABLE OF CONTENTS

LIST OF TABLES

LIST OF FIGURES

Chapter 1

Introduction

1.1 The Nuclear Landscape

All of the observable matter in the universe is composed of protons, neutrons, and electrons. In the center of an atom, positively charged protons and uncharged neutrons are located inside the nucleus, while negatively charged electrons orbit around the nucleus. All of the positive charge inside of an atom is contained inside the nucleus, while the negative charge is spread out by the motion of electrons. The identity of an atom, which is its element, is determined by the number of protons inside the nucleus. This is the basis of the chemical periodic table of the elements, which arranges all the elements in order of the number of protons. Unlike the atom, the nucleus is defined by both the number of protons and neutrons present. This forms the basis for the chart of the nuclides, shown in Figure 1.1. In this chart, each square represents a nucleus with a given number of protons and neutrons. The proton number, Z, is shown on the y-axis, and the neutron number, N, is shown on the x-axis. The mass number, A, is defined as the sum $A = Z + N$ of the proton and neutron numbers, because protons and neutrons have approximately the same mass (1.673×10^{-27} kg for protons and 1.675×10^{-27} kg for neutrons), while the mass of electrons is much smaller (9.109×10^{-31} kg). Thus the mass of an atom is nearly equal to the sum of the number of protons and neutrons, which are jointly called nucleons. A given nucleus is fully specified by four terms: the element (X), proton number (Z), neutron number (N), and mass number

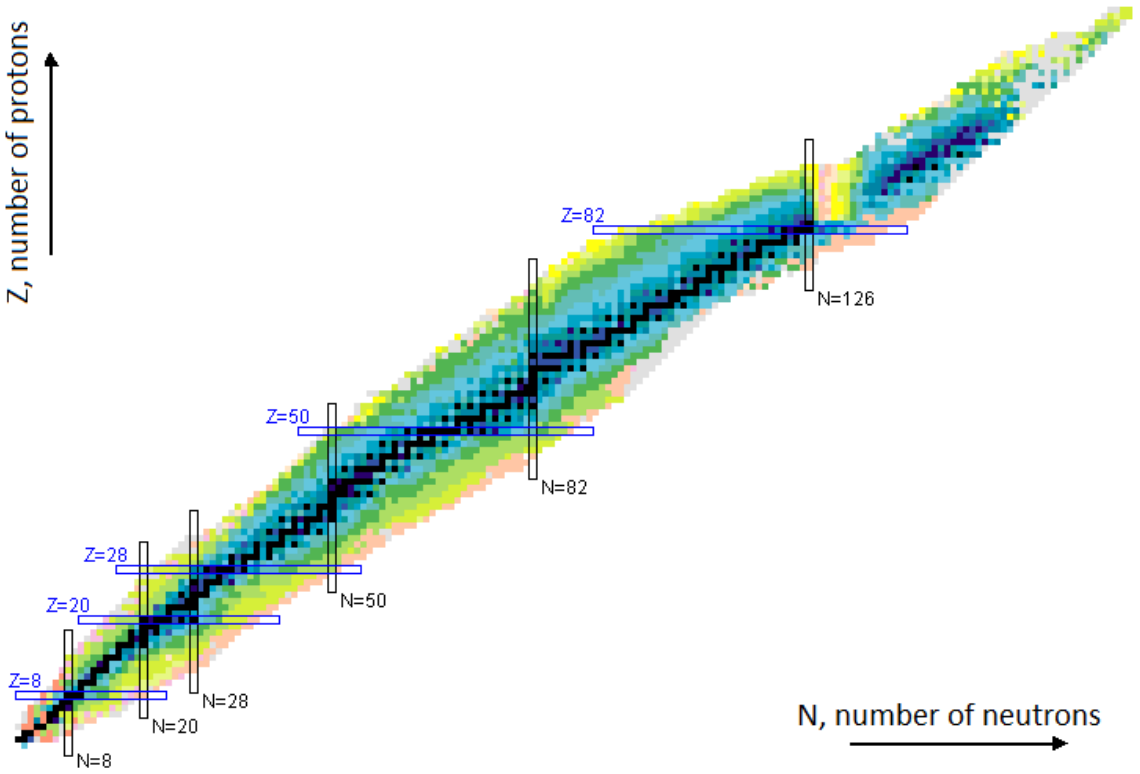

Figure 1.1: The chart of the nuclides, which displays all known nuclei. Each square represents an isotope with a specific combination of protons and neutrons. Black squares show the locations of stable nuclei, while other colors represent the half-lives for unstable nuclei. Figure adapted from Ref. [1]

(A). These are used to notate the nucleus as ${}^{A}_{Z}X_{N}$ which identifies all these terms at once. However, this full notation is not always necessary, because the element is determined by the proton number, and the neutron number can be solved from the mass number as $N = A - Z$. Thus the typical notation used in nuclear physics is ${}^{A}X$, which fully describes the nucleus.

Although almost all of the mass of an atom is contained within the nucleus, the nuclear size is much smaller than the atomic size. The size of the nucleus depends on the total number of protons and neutrons present, and is typically on the order of several femtometers, or 10^{-15} meters. In contrast, the radius of the atom is determined by the orbits of electrons around the nucleus and is on the order of 0.1 nanometers, or 10^{-10} meters.

There are several terms which are useful in describing nuclides with specific combinations

of proton and neutron numbers. Nuclei which have the same number of protons but different numbers of neutrons are called *isotopes*. These appear as horizontal lines in Figure 1.1. Nuclei with the same number of neutrons but different numbers of protons are called *isotones*, and appear as vertical lines. Finally, nuclei with the same mass number, but different numbers of protons and neutrons are called *isobars*. Isobars form diagonal lines in Figure 1.1, moving from the upper left to the bottom right. One feature that is shown prominently in Figure 1.1 is the stability of individual nuclei. Stable nuclei are shown by black squares, while unstable, or radioactive, nuclei are shown by other colors based on their half-lives [1]. It is clear from the chart that there is a pattern in the positions of stable nuclei. The location of the stable nuclei across the entire chart is called the valley of stability. For light nuclei with small Z and N, stability occurs when the proton and neutron numbers are nearly equal, and $N/Z \approx 1$. Heavier nuclei, however, experience a stronger repulsive Coulomb force due to the large number of protons, and additional neutrons are necessary for the nuclei to remain stable. The heaviest nuclei can reach ratios of $N/Z \approx 1.5$. In addition, a further distinction is made in the chart. There are combinations of Z and N at the edges of the chart which do not form nuclei; these are called unbound because the extreme numbers of protons or neutrons prevent a nuclear compound from forming for any finite amount of time. The boundaries between the bound and unbound nuclei are called the drip lines. The proton drip line is located to the left of the valley of stability, and the neutron drip line is located to the right.

As shown in Figure 1.1, there are more than 3000 unstable nuclei, which form the majority of all known nuclei. These nuclei decay into more stable nuclei, and can do so in a wide variety of ways. The most common types of radioactive decay are alpha decay, beta decay, gamma decay, and fission.

The first type of radioactive decay, alpha decay, also called alpha emission, occurs only for the heaviest nuclei, typically with mass numbers above $A = 200$. In this process, a nucleus ejects two protons and two neutrons together as a $^{4}_{2}$He nucleus, which is also called an alpha particle. Because of the loss of two protons from the nucleus, the element is changed during the alpha emission. Through this process, heavy unstable nuclei located in the top-right corner of the chart of nuclides move toward the stable nuclei by moving down and to the left on the chart. The alpha particle is typically emitted with energy in the range 2–5 MeV. Due to conservation of momentum, the remaining large nucleus obtains a small kick during the decay and shares some of the decay energy as kinetic energy.

The second type of radioactivity, beta decay, occurs in the majority of nuclei which are not stable. There are actually two types of beta decay, denoted β^+ decay and β^- decay. In β^- decay, a neutron is transformed into a proton through the emission of an energetic electron as well as an antineutrino. The opposite occurs in β^+ decay, in which a proton transforms into a neutron, emitting a positron (the positively charged antiparticle of an electron) and a neutrino. An alternative to β^+ decay is electron capture, in which an atomic electron is absorbed by the nucleus while a proton is changed into a neutron. In all three decays, the proton number of the nucleus is changed, while the mass number is unchanged, because the total number of nucleons, and therefore the mass number, remains unchanged. These decays allow nuclei to move towards the stable nuclei. For β^- decay, nuclei with excess neutrons approach stability by moving up and to the left in the chart of nuclides. In β^+ decay and electron capture, proton-rich nuclei are moved down and to the right in the chart of nuclides.

The third type of decay, gamma decay, occurs through the emission of a photon. In the gamma-decay process, all nucleons remain in the nucleus. The gamma ray only carries away

energy as the nucleus de-excites into a lower energy state. Typically, gamma decay occurs after another form of radioactive decay which leaves the nucleus in an excited state. Most gamma rays are emitted with energies in the range 0.1–10 MeV.

The fission process occurs when a heavy nucleus splits apart into two smaller nuclei. During the fission process, a large amount of energy is released, about 200 MeV, which is mostly given to the daughter nuclei as kinetic energy. Unlike the previous types of decay, the final products are not fixed, but are distributed among the medium-mass nuclei. These products tend to be neutron-rich because of the relative neutron excess for heavy nuclei. After being created, the daughter nuclei may then beta decay towards stability.

In addition to the aforementioned decay processes, other types of radiation are possible, although much less common. Proton radioactivity results in the emission of a proton from the nucleus, and occurs for proton-rich nuclei. This can happen when a nucleus is in an excited state with an energy larger than the proton separation energy S_p. This is defined as the binding energy of the least-bound proton and can be calculated from

$$S_p = [-m(Z,N) + m(Z-1,N) + m_{^1\mathrm{H}}]c^2 \tag{1.1}$$

where $m(Z,N)$ and $m(Z-1,N)$ are the atomic masses of nuclei with proton numbers Z and $(Z-1)$, and neutron number N. The atomic mass of Hydrogen $m_{^1\mathrm{H}}$ is the sum of the proton mass $m_p = 938.3$ MeV/c^2 and electron mass $m_e = 0.511$ MeV/c^2. Emission of one or two protons also occurs from the ground state of nuclei beyond the proton drip line, where the proton separation energy is less than zero. Similarly, the neutron separation energy S_n is defined as

$$S_n = [-m(Z,N) + m(Z,N-1) + m_n]c^2 \tag{1.2}$$

where $m_n = 939.6$ MeV/c^2 is the neutron mass.

1.2 Nuclear Shell Model

One feature which is highlighted in Figure 1.1 is the existence of magic numbers. These are shown in the horizontal and vertical boxes for proton and neutron numbers of 8, 20, 28, 50, 82, and 126. Though not shown in Figure 1.1, 2 is also considered as one of the magic numbers. These values are called magic because nuclei which have this many protons or neutrons exhibit increased stability. This stability is evident in the form of higher binding energies, higher separation energies, and higher-lying excited states compared to neighboring stable nuclei. The observation of magic numbers has led to the development of the nuclear shell model [2]. Within the shell model, nucleons fill up the nucleus by first occupying single-particle states with the lowest energies. The presence of a large gap in energy between orbitals creates a shell, and the number of nucleons within each shell corresponds to the magic numbers.

The simplest form of the nuclear potential is the harmonic oscillator (H.O.) potential [3]:

$$V_{HO}(r) = \frac{1}{2} m\omega^2 r^2 \ . \tag{1.3}$$

which gives the potential V_{HO} as a function of radius r with the frequency parameter ω. In three dimensions, this potential leads to single-particle states characterized by quantum numbers n and ℓ. Here, n is the number of radial nodes in the wave function, and ℓ is the orbital angular momentum of the wave function. The energy of a nucleon with quantum

numbers n and ℓ is given by:

$$E(n,\ell) = (2n + \ell + 3/2)\hbar\omega \ . \tag{1.4}$$

Here there is a degeneracy in the energy for different combinations of n and ℓ. Thus, it is customary to define the major oscillator quantum number $N = 2n + \ell$ which determines the energy of all degenerate wave functions. This is shown on the left side of Figure 1.2, where the energy levels for each N are plotted. Each ℓ contains $2(2\ell + 1)$ degenerate wave functions, so that the total degeneracy for each oscillator number N=0, 1, 2... is 2, 8, 20, 40, 70, 112... [3]. This reproduces the smaller magic numbers (2, 8, and 20), but fails to account for the larger magic numbers.

The harmonic oscillator potential presents inherent problems in describing the nucleus because the strength diverges for large radius, creating an infinite-range force. Because the nuclear force is known to have a finite range, a more realistic form of the nuclear potential which takes into account the finite range is necessary to better explain nuclear properties. One example of such a potential comes from the Woods-Saxon form [3]:

$$V_{WS}(r) = \frac{V_0}{1 + \exp((r - R_0)/a)} \ . \tag{1.5}$$

Here, $R_0 = 1.25A^{1/3}$ fm is the radius of the potential, and $a = 0.67$ fm is the diffuseness of the potential. The primary advantage over the harmonic oscillator potential is that this potential does not diverge at infinity. In this case, energy levels are again determined by n and ℓ, and form major oscillator shells. However, different ℓ values are not degenerate, and higher-ℓ orbitals have lower energies than lower-ℓ orbitals within the same shell. This

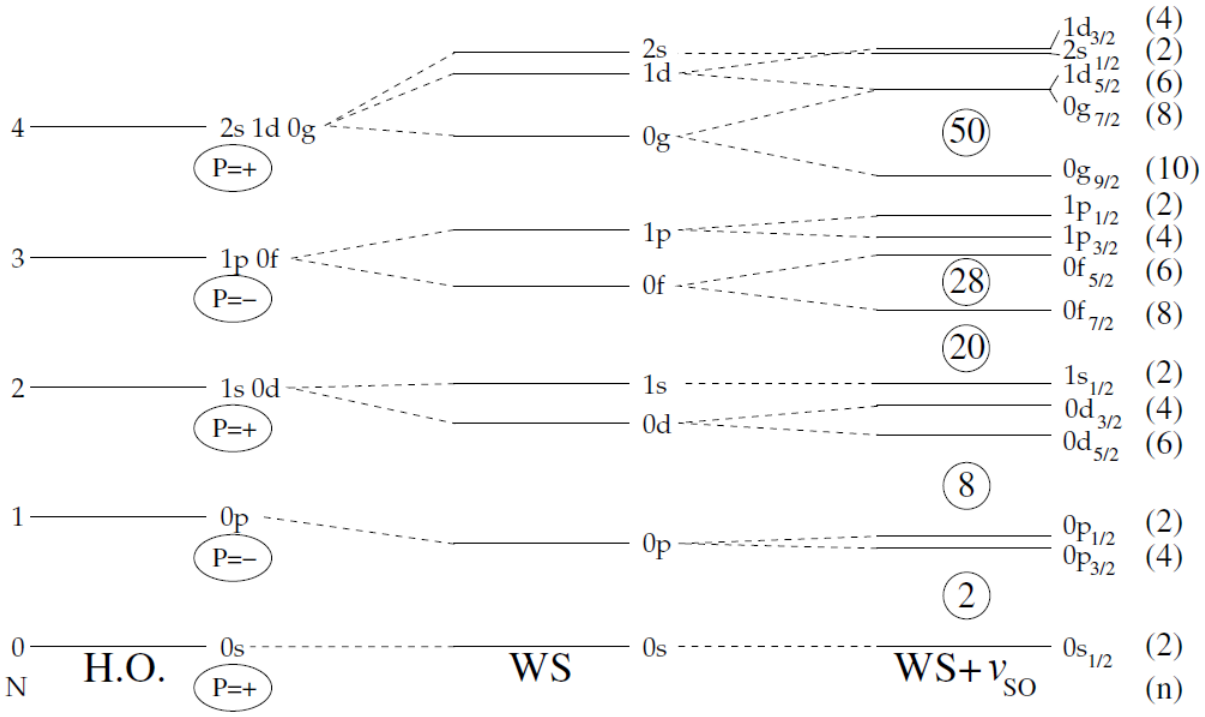

Figure 1.2: A diagram showing the splitting of energy levels within the nuclear shell model. The left column shows the relative energy levels of the major shells using a harmonic oscillator (H.O.) potential. The middle column shows how the levels change when a Woods-Saxon (WS) potential is used. Here, the levels are split according to the orbital momentum quantum number ℓ. The right column shows the changes when a spin-orbital term ($\mathcal{V}_{SO}$) is included in the potential, and shows further splitting according to the total angular momentum quantum number $j = \ell \pm 1/2$. In all cases, a large gap between levels indicates a shell closure, but only the right column reproduces the observed magic numbers. Figure from Ref. [4]

is shown by the center of Figure 1.2, where the splitting of the orbital angular momentum relative to the harmonic oscillator is evident.

The important term in the potential which allows for the correct prediction of magic numbers is the spin-orbit term. This was first introduced by Hans Jensen [5] and Maria Goeppert-Mayer [2], who shared the Nobel Prize in physics for discovery of this term. The spin-orbit coupling term in the potential has the form

$$V_{SO}(r) = V_{\ell s}\frac{d}{dr}\left(\frac{1}{1+\exp((r-R_0)/a)}\right)\vec{\ell}\cdot\vec{s}\,. \tag{1.6}$$

This term is added to the radial term of Equation 1.5 [3], and the results are shown on the right side of Figure 1.2. With this term, the energy levels for each ℓ are split by the quantum number j, the total angular momentum. The total angular momentum is formed by the vector addition of the orbital angular momentum $\vec{\ell}$ and the spin $\vec{s}$ of every nucleon. Because the intrinsic spin s is $1/2$ for protons and neutrons, $j = \ell \pm 1/2$. The strength of the spin-orbit term $V_{\ell s}$ is negative, which means that the energy is lower for $j = \ell + 1/2$ states, when $\vec{\ell}$ and $\vec{s}$ are parallel. The splitting of the energy increases with increasing j, so that for large j, the orbitals can move across the major shells to create new energy gaps and therefore new magic numbers. As shown in Figure 1.2, the addition of the spin-orbit term correctly produces the magic numbers 28 and 50. The magic number 28 occurs when the $\ell = 3, j = 7/2$ orbital (denoted $0f_{7/2}$) is lowered in energy below the $N = 3$ shell. Similarly, the gap at 50 is formed when the $\ell = 4, j = 9/2$ orbital ($0g_{9/2}$) moves below the $N = 4$ shell. The inclusion of the spin-orbit term also predicts the magic numbers 82 and 126, which complete all known magic numbers as shown in Figure 1.1.

The nuclear shell model has been very successful in predicting properties of many nuclei.

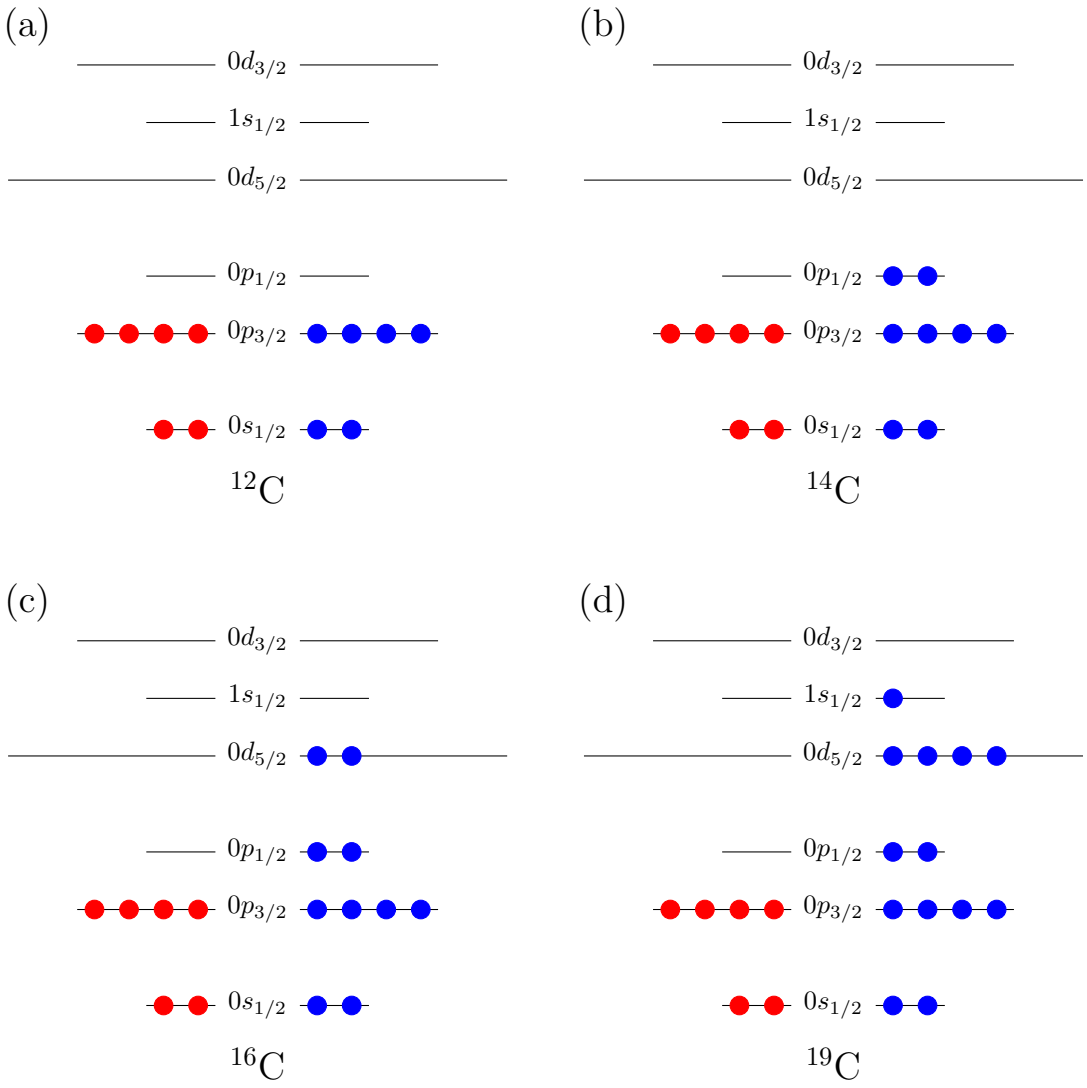

Figure 1.3: A illustration of the naïve shell-model configurations for the ground states of several carbon isotopes. The orbitals for the s, p, and sd shells are shown in the standard ordering, similar to Figure 1.2. Protons are shown in red, and neutrons in blue. In the stable nucleus ^{12}C (a), all six protons and six neutrons fill the $0s_{1/2}$ and $0p_{3/2}$ orbitals. In the near-stable nuclei ^{14}C (b) and ^{16}C (c), the additional neutrons first fill the $0p_{1/2}$ orbital, and then begin to occupy the $0d_{5/2}$ orbital. In ^{19}C, however, the thirteenth neutron occupies the $1s_{1/2}$ orbital. The $1s_{1/2}$ orbital in ^{19}C is important in the formation of the ground-state halo structure.

However, there are several challenges associated with the shell model. One such example is heavy nuclei with non-spherical shapes. Calculation of properties of these nuclei are better served by other models, such as the Nilsson model or a collective model [6]. For nuclei away from stability, the energies of single-particle states can change rapidly, causing the ordering of orbitals to deviate from the standard picture shown in Figure 1.2. An example of this deviation is shown in Figure 1.3, which shows the primary configurations of protons and neutrons in several carbon isotopes. For the nuclei ^{12}C, ^{14}C, and ^{16}C, the neutrons fill orbitals as expected by the standard picture, but for the drip-line nucleus ^{19}C, the $0d_{5/2}$ and $1s_{1/2}$ orbitals are occupied simultaneously. The present work provides insight to the shell-model configurations in ^{19}C by measuring the gamma-ray transition strength between the bound states. The changes in single-particle energies also creates energy gaps between different orbitals. This can cause new magic numbers to appear, such as $N = 16$ [7] and $N = 32$ [8], while other conventional magic numbers may disappear, such as $N = 8$ [9, 10], $N = 20$ [11].

1.3 Halo Nuclei

One of the challenges to the shell model description of nuclei is the appearance of exotic structures in radioactive nuclei. Near the limits of stability, as the energy levels of valence nucleons approach the particle decay threshold, a new structure called a halo can emerge. A halo consists of weakly bound neutron or proton that is largely decoupled from the nuclear core and has a wave function with an enhanced radius. Formation of the halo is favored for neutrons in low angular momentum orbitals, where there is little or no centrifugal or Coulomb barrier arising in the potential. This allows the neutron to tunnel outside of the nuclear core

and form a low-density "cloud" around the core. For example, the density of the protons and neutrons for the two-neutron halo ^{22}C [12] is shown in Figure 1.4. The existence of a neutron cloud is apparent from the neutron density, which decreases at large radius much more slowly than the proton density. Experimental identification of halo nuclei has been made through three types of measurements: interaction cross section [13, 14], momentum distribution following nucleon removal [15, 16], and Coulomb breakup reactions [17–19]. Each of these measurements is associated with a different feature of halo nuclei, and together they establish the halo as a unique phenomenon of weakly bound nuclei. The earliest halo nucleus to be identified was ^{11}Li, which exhibits a two-neutron halo around a ^{9}Li core. The first indication of an unusual structure came from the observation of an enhanced interaction cross section [13]. This is demonstrated in Figure 1.5, which plots the rms radius deduced from interaction cross sections for several light nuclei. The large enhancement for ^{11}Li compared to the other lithium isotopes is apparent. Subsequent measurements of the momentum distribution of ^{9}Li recoils following two-neutron removal [15], and the electromagnetic dissociation of ^{11}Li [20] firmly established ^{11}Li as a halo nucleus. Since the first discovery of the halo structure, several other halo nuclei have been identified, up to the medium-mass nucleus ^{37}Mg [21]. The present work describes a measurement of the gamma-ray transition in ^{19}C, which exhibits a halo structure in its ground state. The $1s_{1/2}$ orbital, which is responsible for the halo formation, is shown to be an important factor in the observed transition rate.

The primary feature present in halo nuclei is an enhanced radius compared to neighboring nuclei. Measurement of the radius has primarily come from measurements of the interaction cross section. The interaction cross section σ_I is the cross section to change either the proton or neutron number when a projectile nucleus is incident on a target. The relation between

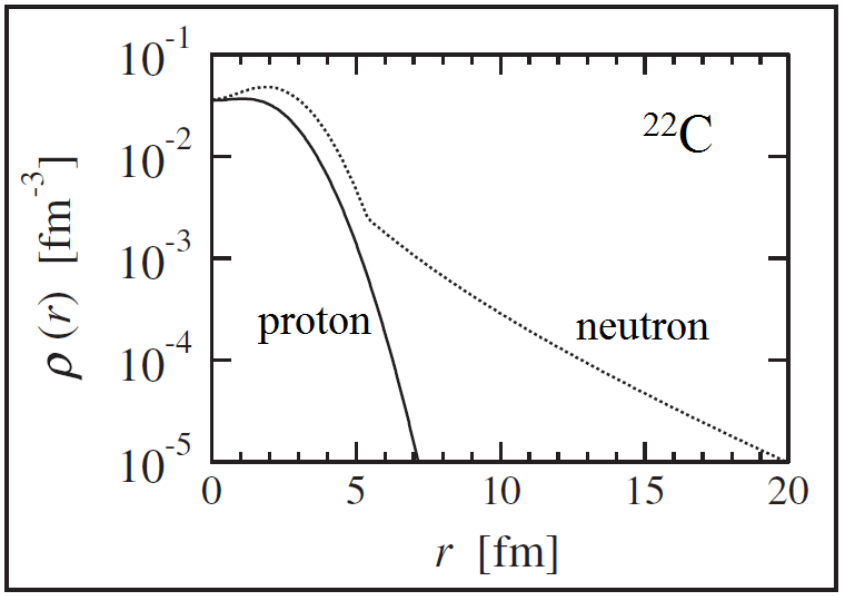

Figure 1.4: A plot of the calculated densities for the protons (solid line) and neutrons (dotted line) in ^{22}C, which is known to be a two-neutron halo. The neutron density falls of much more slowly than the proton density at large radius, which is the primary feature of halo nuclei. Figure adapted from Ref. [12].

σ_I and the nuclear size can be most simply understood in terms of the interaction radius R_I [13]:

$$\sigma_I = \pi[R_I(p) + R_I(t)]^2 \tag{1.7}$$

where $R_I(p)$ and $R_I(t)$ are the projectile and target radii, respectively. Although not directly related to the interaction radius, the root mean square R_{rms} is a more useful measure of the nuclear size. This is obtained from σ_I by fitting the cross section obtained from a Glauber model calculation [13, 22]. For stable nuclei, the radii follows a simple trend [4], with

$$R = r_0 A^{1/3} \tag{1.8}$$

using a typical radius parameter $r_0 = 1.25$ fm. For halo nuclei, however, the radius can be much larger. This is demonstrated in Figure 1.5, which shows the R_{rms} for several light

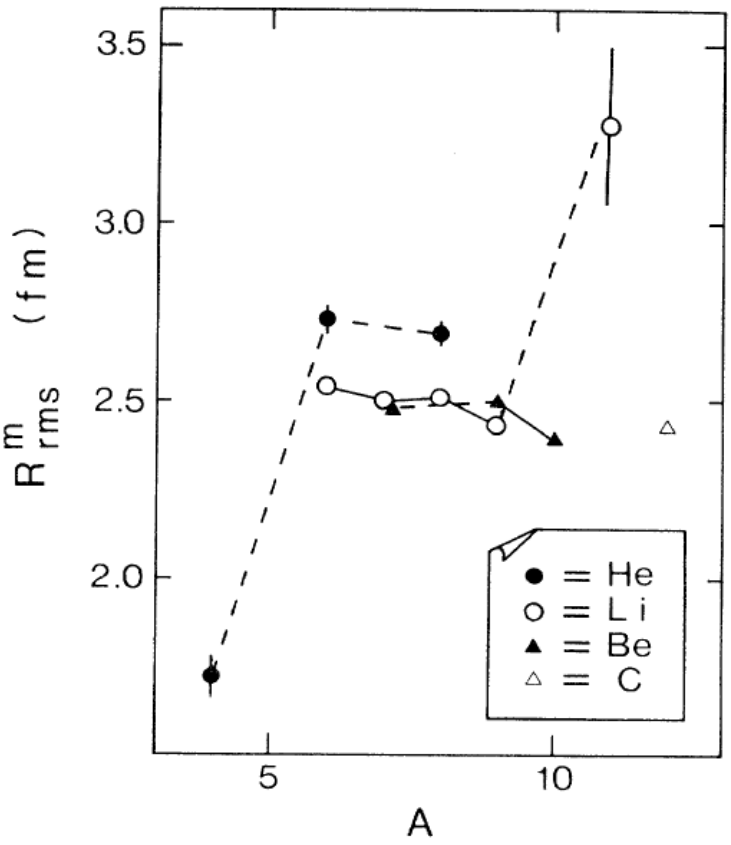

Figure 1.5: The root mean square radii of several light nuclei, deduced from the interaction cross section. There is a large enhancement in radius between ^{9}Li and ^{11}Li which deviates from the normal $A^{1/3}$ trend. This measurement was the first indication of the halo structure in ^{11}Li. Figure from Ref. [13].

nuclei determined from the interaction cross sections [13]. There is a clear enhancement in the radius for ^{11}Li which deviates from the trend shown by several other nuclei.

Another means to identify halo nuclei is measurement of the momentum distribution of fragments following removal of the halo nucleon. These measurements are made by bombarding the nucleus on a light target at high incident beam energy, and the momentum of the recoiling nuclear fragment can be measured either parallel or transverse to the direction of the beam [23]. The momentum distribution of the fragments can be related to the momentum of the removed nucleon, where a narrow distribution of the fragment indicates a low momentum of the nucleon within the halo nucleus. The relation between a large radius

and a narrow momentum distribution following nucleon removal has been interpreted within the context of the uncertainty principle, where a wave function with a larger spatial distribution has a lower momentum [15]. The combined results present a consistent picture of the structure of the halo with a weakly bound nucleon with an extended, low-momentum wave function.

The third type of measurement which is useful for studying halo nuclei is Coulomb breakup reactions. In this measurement, the halo nucleus is incident on a heavy, high-Z target at a high beam energy. The absorption of a virtual photon from the strong Coulomb field of the target causes the halo nucleon to be released into the continuum. The energy and momentum of both the nuclear fragment and the emitted nucleon are measured, and the relative energy spectrum of the breakup is reconstructed from the invariant mass of the fragment and nucleon. The energy distribution of the breakup can be related to the wave function of the halo [18] as

$$\frac{d\sigma_{CD}}{dE_{rel}} = \frac{16\pi^3}{9\hbar c} N_{E1}(E_x) \left| \langle q | \frac{Ze}{A} r Y^1_m | \Phi(\vec{r}) \rangle \right|^2 \tag{1.9}$$

where σ_{CD} is the Coulomb dissociation cross section as a function of the relative breakup energy E_{rel}, $N_{E1}(E_x)$ is the number of virtual photons for excitation, $\langle q|$ is the wave function of the nucleon in the continuum, Y^1_m is an $\ell = 1$ spherical harmonic, and $|\Phi(\vec{r})\rangle$ is the wave function of the halo nucleus before breakup. Because of the large radial wave function, the most important component of Coulomb breakup of halo nuclei is the electric dipole, or $E1$ breakup [18]. The $E1$ operator has the form rY^1, and the radial term provides a sensitive probe of the wave function for a halo. Several measurements have revealed large breakup cross sections at low excitation energies, which have been observed as a feature

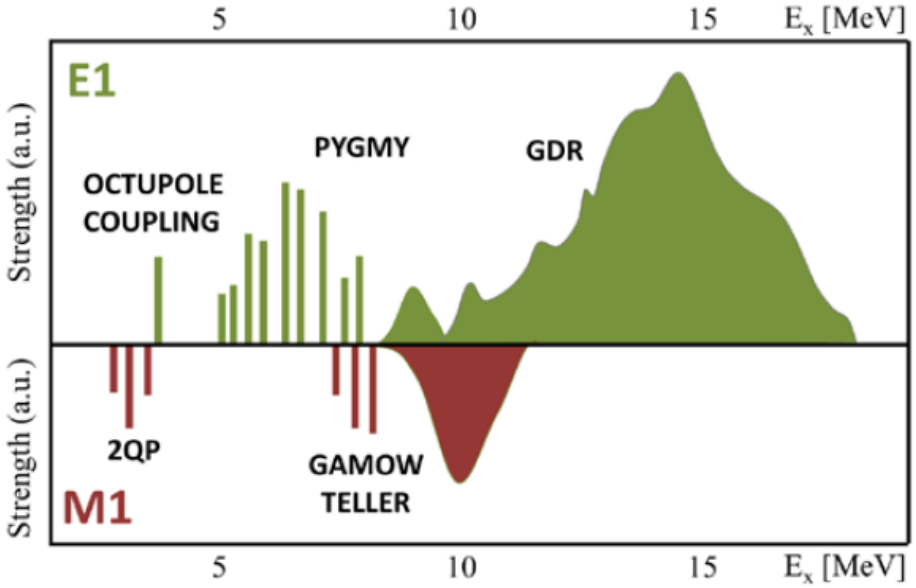

Figure 1.6: A plot showing an example of the distribution of the $E1$ and $M1$ strengths in heavy nuclei. The pygmy dipole resonance is located at lower energy than the giant dipole resonance (GDR). For lighter neutron-rich nuclei, the low-energy $E1$ response is due to a soft dipole excitation without a resonance character. Figure from Ref. [24].

unique to halo nuclei [25]. An example of the distribution of the $E1$ strength in nuclei is in Figure 1.6, which shows the typical distribution of the electric dipole ($E1$) and magnetic dipole ($M1$) responses. At high excitation energies, there is a large component from the Giant Dipole Resonance (GDR). However, at low excitation energies, there are additionally smaller resonances. For heavy nuclei, these are called pygmy resonances, but for light halo nuclei, the low-energy strength is in the form of soft-dipole modes, which was originally interpreted as a motion of the outer neutrons against the nuclear core [26]. This soft-dipole mode has been well-studied for halo nuclei. However, the magnetic response of halo nuclei is not as well studied, hampering detailed characterization of halo systems.

In addition to their interest from a structure perspective, halo nuclei have attracted interest for their use in nuclear reactions. For example, the neutron-capture reaction has been studied for ^{14}C leading to the ground-state halo in ^{15}C [27–29]. In this case, the extended

wave function of the halo neutron in ^{15}C leads to the dominance of p-wave capture, which is distinct from most astrophysical capture reactions, where the s-wave capture reaction is usually dominant [29]. In addition, several light neutron-halo nuclei have been investigated in fusion reactions to observe a possible enhancement of the fusion cross section. The use of neutron-rich nuclei is regarded as useful in the synthesis of neutron-rich heavy elements with $Z > 114$ [30]. However, the results of these studies are mixed, with some reporting enhancement of cross sections below the Coulomb barrier [31, 32], while others show no enhancement [33, 34]. The suppression of the cross section above the Coulomb barrier has been explained as a strong preference for the neutron transfer reaction, a phenomenon unique to halo nuclei [35].

1.4 Electromagnetic Transitions

One of the most useful ways to study and characterize nuclear structure is by measuring gamma-ray transitions between bound states in nuclei. Measurement of gamma rays gives direct access to the electromagnetic properties of nuclei. The probability to emit a gamma ray, which is directly related to the lifetime of a state, can be related to the wave functions of the initial (ψ_i) and final (ψ_f) states of the nucleus as

$$\lambda(\sigma L) = \frac{8\pi(L+1)}{\hbar L[(2L+1)!!]^2}\left(\frac{E_\gamma}{\hbar c}\right)^{2L+1}\frac{\left|\langle\psi_f||\mathcal{M}(\sigma L)||\psi_i\rangle\right|^2}{2J_i+1}\ . \tag{1.10}$$

Here, $\lambda(\sigma L)$ is the rate of the transition between initial and final states ψ_i and ψ_f. The decay can be either electric ($\sigma = E$) or magnetic ($\sigma = M$) in nature, with a multipolarity L. The most common multipolarities are dipole ($L = 1$) and quadrupole ($L = 2$). E_γ is the

energy of the decay. $\mathcal{M}(\sigma L)$ is the electromagnetic operator which governs the transition. The last term in Equation 1.10 is the reduced transition probability $B(\sigma L; i \rightarrow f)$:

$$B(\sigma L; i \rightarrow f) = \frac{\left|\langle \psi_f || \mathcal{M}(\sigma L) || \psi_i \rangle\right|^2}{2J_i + 1} \ . \tag{1.11}$$

This term contains all of the structure information about the initial and final states. The electric and magnetic operators have distinct forms and depend on the multipolarity of the transition:

$$\mathcal{M}(EL) = \sum_{k=p,n} e_k (r_k)^L Y_m^L(\theta_k, \phi_k) \tag{1.12}$$

$$\mathcal{M}(ML) = \sum_{k=p,n} \left[g_{s,k} \vec{s}_k + \frac{2}{L+1} g_{\ell,k} \vec{\ell}_k \right] \cdot \nabla_k \left[(r_k)^L Y_m^L(\theta_k, \phi_k) \right] \mu_N \ . \tag{1.13}$$

Both operators are summed over each of the k nucleons. The charges of the nucleons are represented by e_k, with $e_p = +e$ and $e_n = 0$. The Y_m^L are the spherical harmonics. The spin and orbital g-factors of the nucleons are represented by $g_{s,k}$ and $g_{\ell,k}$, respectively, and μ_N=0.105 $e$fm is the nuclear magneton. In order to determine the lifetime τ of a state, the total rate must be calculated from all transitions from the initial state to all possible final states:

$$\frac{1}{\tau} = \lambda = \sum_{\sigma L} \lambda(\sigma L) \ . \tag{1.14}$$

Thus, measurement of the lifetime of a gamma-ray decay can provide detailed information about the structure of a nucleus.

It is important to consider what types of gamma decay can be present for a given initial excited state. The available decays between the initial and final states are constrained by

the angular momentum J and parity π of both the initial and final states. Most importantly, the angular momenta of the initial and final states cannot differ by more than the angular momentum of the gamma ray:

$$|J_i - J_f| \leq L \leq J_i + J_f \ . \tag{1.15}$$

This is called the triangle rule because it is a constraint that arises from the conservation of angular momentum, so that the vectors $\vec{J_i}$, $\vec{J_f}$, and $\vec{L}$ must form a closed triangle. In addition, consideration must be made for the parity π of the states, which can either be positive or negative. If the parity of the final state is the same as the initial state, then the parity of the electromagnetic operator must be $\Delta\pi = +1$. If the states have opposite parity, then the parity of the operator must be $\Delta\pi = -1$. The parity of the electric and magnetic operators are given by

$$\Delta\pi(EL) = (-1)^L \tag{1.16}$$

$$\Delta\pi(ML) = (-1)^{L+1} \ . \tag{1.17}$$

These conditions limit the multipolarities σL for allowed transitions, which are summed in Equation 1.14. Because the coefficient in the front of Equation 1.10 depends strongly on L, the transition rate decreases drastically for increasing L. This means that, for a given pair of initial and final states, usually only the transition with the lowest multipolarity contributes significantly to the lifetime.

Because of the $2L+1$ dependence in Equation 1.10, the absolute transition rates depend strongly on the transition energy E_γ. In order to understand the relative strength of a tran-

sition, the Weisskopf unit is introduced, which provides an estimate of the transition rate for a given multipolarity [36]. The estimation is made by assuming that the transition is caused by a single proton moving between pure single-particle shell-model states. Additionally, the calculation assumes that the radial wave functions of the initial and final states are constant within the nucleus, with a sphere whose radius is given by Equation 1.8. Weisskopf estimates for the electric and magnetic strengths are defined as

$$B(EL) = \frac{1}{4\pi}\left[\frac{3}{L+3}\right]^2 (1.2A^{1/3})^{2L}\ e^2\mathrm{fm}^{2L} \tag{1.18}$$

$$B(ML) = \frac{10}{\pi}\left[\frac{3}{L+3}\right]^2 (1.2A^{1/3})^{2L-2}\ \mu_N^2\mathrm{fm}^{2L-2}\ . \tag{1.19}$$

These estimations normalize the transition strengths for different nuclei and provide an estimation of the number of nucleons participating in the transition. For example, if a transition has a strength on the order of 1 W.u., then that is an indication that the transition is likely a pure single-particle transition. If the strength is much greater than the Weisskopf estimate, then it is likely that more than one nucleon is involved, and the states are considered to be collective states.

1.5 Nuclear Reactions

One of the most important methods for observing halo nuclei is the measurement of the momentum distributions of nuclei following breakup reactions. Early measurements were based on fragmentation reactions, in which a stable beam is accelerated to high energy, typically above 100 MeV/nucleon, and reacts on a stationary target. Fragments, which have any number of nucleons removed from the projectile nucleus, are then detected after emerging

from the target. The momentum of the fragments is measured, either along the direction of the incoming beam (parallel momentum $p_{\parallel}$) or in a direction perpendicular to the beam (transverse momentum $p_{\perp}$). The interpretation of the momentum distributions was based on the Goldhaber description [37], in which the distribution of fragments was described by a Gaussian form with a momentum width parameter σ given by

$$\sigma^2 = \sigma_0^2 \frac{A_F(A - A_F)}{A - 1} \tag{1.20}$$

where σ is the observed width, A and A_F are the mass numbers of the beam and fragment, respectively, and σ_0 is a constant which is usually in the range 70–90 MeV/c. This can be seen in Figure 1.7(a), which shows the transverse momentum of ^{6}He fragments following fragmentation of a ^{8}He beam at 790 MeV/nucleon [15]. One of the earliest indications of a halo nucleus came from the momentum distribution of ^{9}Li following the removal of two neutrons from ^{11}Li [15]. Here, the distribution included a component which was much narrower than that expected from Equation 1.20. This can be seen in Figure 1.7(b), where the narrow distribution with $\sigma_0 = 23$ MeV/nucleon is seen on top of a distribution with the more typical $\sigma_0 = 71$ MeV/nucleon. The narrow distribution was discussed as resulting from the weak binding energy of the two valence neutrons in ^{11}Li. Along with this result came new insights into the reaction dynamics. First, it was noted that the momentum distribution of the projectile-like fragment matches the distribution of the removed nucleons [15]. Second, the momentum distribution could be qualitatively understood in terms of Heisenberg's uncertainty principle. Larger spatial distributions for the neutron wave functions in halo systems lead to narrow momentum distributions following their removal [15, 25]. Thus, the observation of the narrow momentum distribution indicated both a small momentum of the

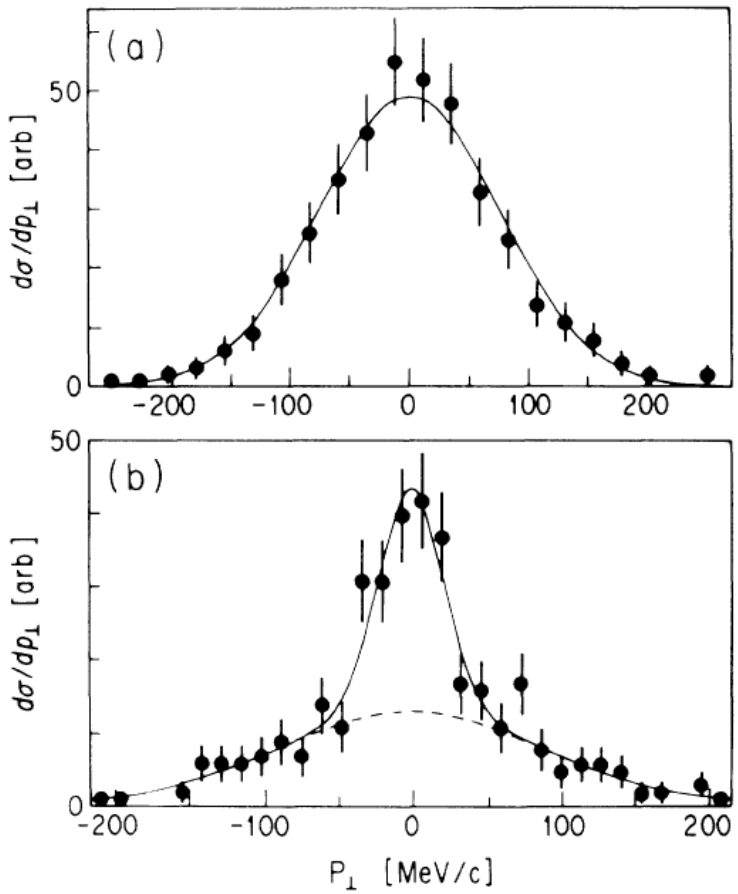

Figure 1.7: Transverse momentum distributions of (a) ^{6}He following two-neutron removal of ^{8}He and (b) ^{9}Li following two-neutron removal of ^{11}Li. The narrow component in (b) is indicative of the extended wave function of the removed neutrons. Figure from Ref. [15].

valence neutrons and a large neutron wave function, providing a consistent picture for the halo structure in ^{11}Li.

More recent developments in theory have allowed for a direct connection between momentum distributions and the single-particle structure of nucleons by using single-nucleon knockout reactions [23]. Theoretical momentum distributions can be calculated for a given wave function for a nucleon within the projectile, and the shape of these distributions are sensitive to the angular momentum of the wave function. This can be seen in Figure 1.8, which shows the parallel momentum $p_{\|}$ of ^{18}C nuclei following the one-neutron knockout reaction of ^{19}C at 57 MeV/nucleon [23]. The data are compared to theoretical curves for

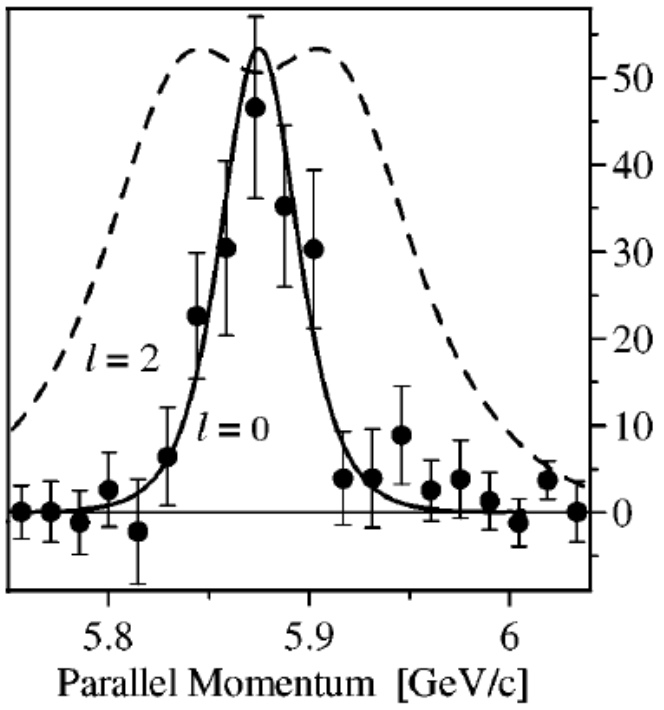

Figure 1.8: Parallel momentum distribution of ^{18}C following one-neutron knockout of ^{19}C. Data points in black are compared to theoretical calculations for $\ell = 0$ (solid line) and $\ell = 2$ (dashed line) neutron removal. Figure from Ref. [23].

$\ell = 0$ (s-wave) and $\ell = 2$ (d-wave) neutron removal. The difference in the two curves provides a clear way to extract the angular momentum of the valence neutron, and confirms the low angular momentum of the halo neutron in the ground state of ^{19}C. By tagging on gamma-rays which are coincident with outgoing fragments, this method can be used to extract exclusive cross sections leading to both ground and excited states of the reaction products. Thus, measurement of momentum distributions following single-nucleon knockout reactions has become a powerful tool for nuclear structure determination.

Chapter 2

Experimental Techniques

In the present study, the $M1$ transition rate for the $3/2^+ \rightarrow 1/2^+_{g.s.}$ transition in ^{19}C was measured using the line-shape technique and Recoil Distance Method. Both techniques are based on gamma-ray spectroscopy using a fast beam of radioactive nuclei. The ^{19}C nuclei were produced with a one-proton knockout reaction from a beam of ^{20}N, and the reaction data was analyzed to confirm the spin-parity assignments of the states in ^{19}C as well as the ground state in ^{20}N. The following sections give an overview of the use of gamma-ray spectroscopy with radioactive ion (RI) beams, introduce the methods used to extract the lifetime of nuclear excited states from the gamma-ray spectra, and discuss the theoretical basis for knockout reactions with fast RI beams.

2.1 Development of Radioactive Ion Beams

The ability to produce beams of radioactive nuclei out to the proton and neutron drip lines has been an important step in the progress of nuclear structure studies [38]. Beams of radioactive nuclei are produced from high-energy reactions of stable beams. Because of the high energy at which the radioactive secondary beams are produced, the RI beams can be used in secondary reactions to study the structure of the radioactive nuclei. The use of inverse kinematics, which uses a heavy beam and light target, in combination with the high RI beam energy, means that secondary reaction products are forward-focused. This allows

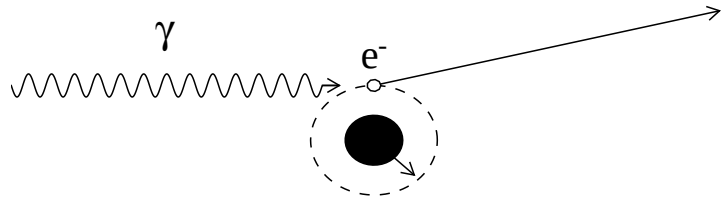

Figure 2.1: A schematic of the photoelectric effect. A photon is absorbed by an electron bound within an atom. The electron gains energy equal to the difference of the photon energy and its binding energy within the atom. The remaining positively charged ion also gains a small amount of recoil momentum.

for event-by-event tracking of the reaction products [23]. One challenge to overcome with the use of RI beams is lower intensities relative to stable beams. This problem is offset by the ability to use thick secondary reaction targets on the order of g/cm^2, since the total reaction yield is given by the product of the cross section and target thickness. For example, Coulomb excitation reactions with radioactive beams can be performed with rates of only a few particles per second [38]. Besides the low intensities, another challenge to using RI beams is the Doppler broadening of gamma rays emitted in flight. This has motivated the development of position-sensitive germanium detectors [39, 40], allowing for detailed gamma spectroscopy of radioactive nuclei. These advancements have made gamma-ray spectroscopy with fast RI beams a powerful tool to study exotic nuclei, and in-flight techniques for gamma-ray spectroscopy have been successfully applied to several types of experiments, such as knockout reactions [41], transfer reactions [42], and lifetime measurements [43].

2.2 Gamma-ray interactions in matter

Gamma-ray detectors measure the energy deposited in matter by incident gamma rays. In contrast to charged particles, which lose energy continuously when moving through matter,

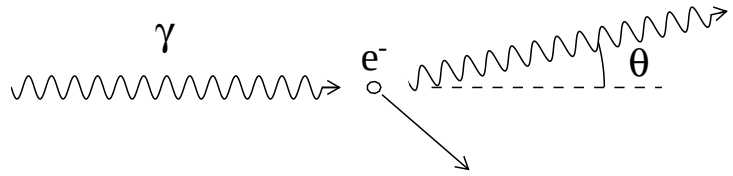

Figure 2.2: A schematic of the Compton scattering process. In this case, the electron is considered to be a free particle, and the photon is scattered elastically off of the electron. The energy of the photon changes depending on the scattering angle.

photons deposit larger amounts of energy in discrete interactions. In the energy range of the gamma spectrum, photons interact primarily in three ways: photoelectric absorption, Compton scattering, and pair production. In all three interactions, photons transfer most of their energy to electrons, which are ultimately slowed down inside of the detector as they lose kinetic energy through continuous collisions with the surrounding atoms.

The first way a photon can deposit energy into a material is through the photoelectric effect. The process is illustrated in Figure 2.1. In this process, a photon is incident upon an electron which is bound within an atom. The electron is ejected from the atom, and the photon disappears. The energy E_e of the ejected electron is given by

$$E_e = E_\gamma - E_b \tag{2.1}$$

where E_γ is the energy of the incident photon, and E_b is the binding energy of the electron within the atom. In order to conserve momentum, the rest of the atom also receives some recoil momentum. However, because the atom is much heavier than the electron, the recoil energy of the atom can be neglected. At gamma-ray energies around 1 MeV, the binding energy of the outer electrons is much smaller than the photon energy, so that almost all of the photon energy is transferred to the kinetic energy of the electron.

The second process is Compton scattering. The process is illustrated in Figure 2.2. In this process, a photon is elastically scattered off of a free electron. In reality, electrons are typically bound within an atom, but the binding energy for outer electrons where the scattering usually occurs is much smaller than the energy transferred to the electron, so this is neglected. During the scattering process, the photon is deflected at some angle relative to its initial motion and transfers energy and momentum to the electron. Due to the conservation of energy and momentum, the energy loss of the photon depends on the scattering angle. The final energy E'_γ of a photon with incident energy E_γ is given by

$$E'_\gamma = \frac{E_\gamma}{1 + (E_\gamma / m_e c^2)(1 - \cos\theta)} \tag{2.2}$$

where $m_e c^2 = 511$ keV is the rest-mass energy of the electron and θ is the scattering angle of the photon. The energy of the recoiling electron is the difference between the incident and final energies of the photon:

$$E_e = \frac{(E_\gamma)^2(1 - \cos\theta)}{m_e c^2 + E_\gamma(1 - \cos\theta)}. \tag{2.3}$$

Two extremes of the electron's energy can be noted. For a small scattering angle $\theta \approx 0$, the photon retains almost all of its energy, and $E_e \approx 0$. At the maximum scattering angle, $\theta = \pi$, the photon transfers the maximum energy, and

$$E_e = \frac{2(E_\gamma)^2}{m_e c^2 + 2E_\gamma}. \tag{2.4}$$

Scattering can happen at any angle between these two extremes, and the differential cross

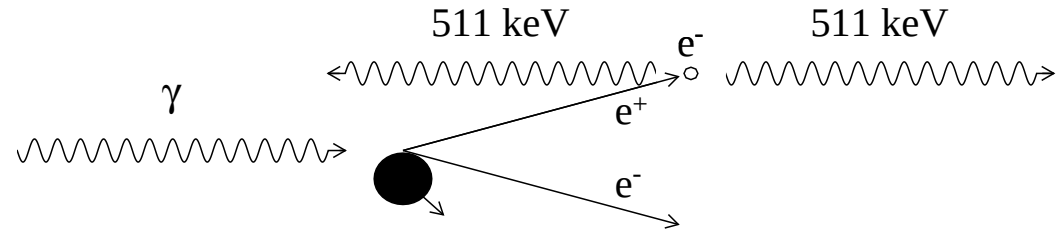

Figure 2.3: A schematic of pair production. Here, the incoming photon interacts with the strong electric field of the atomic nucleus and disappears, creating an electron and a positron. The energy of the photon is split between the mass of the electron-positron pair and the kinetic energy transferred to the electron and positron. The nucleus also gains a slight recoil momentum. After being slowed down in the surrounding material, the positron annihilates with a second electron, creating two photons with energies of 511 keV. These annihilation photons are emitted in opposite directions.

section for Compton scattering is given by the Klein-Nishina formula [44]:

$$\frac{d\sigma}{d\Omega} = Zr_e^2 \left(\frac{1}{1+\alpha(1-\cos\theta)} \right)^2 \left(\frac{1+\cos^2\theta}{2} \right) \left(1 + \frac{\alpha^2(1-\cos\theta)^2}{(1+\cos^2\theta)[1+\alpha(1-\cos\theta)]} \right) \quad (2.5)$$

where Z is the atomic number of the material, $r_e = 2.82 \times 10^{-15}$ m is the classical electron radius, and $\alpha = E_\gamma / m_e c^2$ is the ratio of the photon energy and electron rest-mass energy. After scattering, the new lower-energy photon can then go on to scatter again or be absorbed.

The final process is pair production and is illustrated in Figure 2.3. Here, a photon interacts with the strong electric field within a nucleus and disappears while creating an electron-positron pair. A positron is the anti-particle of the electron, meaning it has the same mass, size, and intrinsic spin as the electron, but is positively charged. The total kinetic energy of the electron-positron pair is equal to the difference of the photon energy and twice the electron rest-mass energy:

$$KE_{e^-} + KE_{e^+} = E_\gamma - 1.022 \text{ MeV} \ . \quad (2.6)$$

Because of the energy that goes into creating the electron-positron pair, this process cannot happen below photon energies of 1.022 MeV, and the process does not become important until several MeV. As in the case of photoelectric absorption, the nucleus gains some of the incident momentum, but its energy can be ignored. The electron and positron then lose energy as they move through the material. When the positron is at rest, it then encounters a second electron, and the two particles annihilate each other and create two photons. The two photons are both created with the energy equal to the electron rest-mass energy, 511 keV. Additionally, because both the electron and positron were essentially at rest before annihilation, they have zero total momentum, which means the two photons must also have zero total momentum. Thus, the two photons are emitted in opposite directions with equal momentum, and they each have an energy of 511 keV. These annihilation photons may go on to interact in the surrounding material via photoelectric absorption or Compton scattering, or may escape from the material. The main consequence of exiting the material is that the energy of the incident photon is only partially deposited in the surrounding material.

A comparison of the cross sections for these three processes is shown in Figure 2.4. The attenuation (in cm^2/g) in germanium is shown as a function of energy in the range 1 keV to 100 MeV. It is clear that at energies below about 100 keV, the photoelectric absorption dominates. Between about 200 keV and 1 MeV, Compton scattering is the most common process. Above several MeV, pair production becomes dominant. Most nuclear transitions have energies between about 50 keV and 5 MeV, so all three processes are relevant for gamma-ray spectroscopy measurements of atomic nuclei.

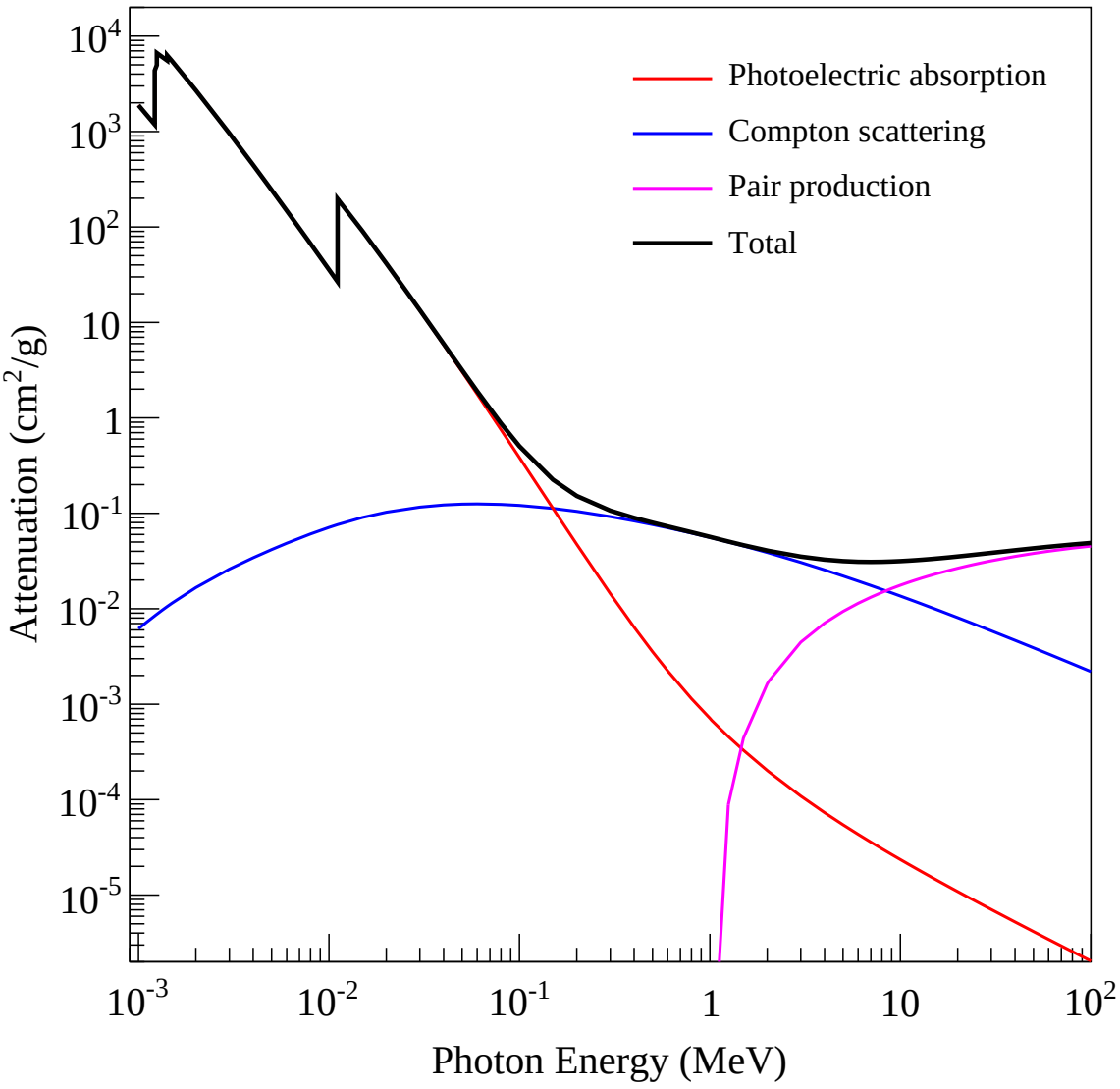

Figure 2.4: Absorption cross sections in solid germanium, plotted as attenuation, for energies between 1 keV and 100 MeV. The plot shows the cross sections for photoelectric absorption (red), Compton scattering (blue), and pair production (magenta). The sum of the three processes is shown in black. Data from the XCOM database [45].

2.3 Relativistic Doppler effect

Lifetime measurements of excited nuclear states are done by measuring gamma rays emitted from these excited states. The present experiment involves measuring gamma rays emitted from a radioactive beam moving at a significant fraction of the speed of light. For such relativistic sources, the emitted gamma rays are significantly Doppler-shifted in the frame

of the laboratory. The energy of gamma rays observed in a laboratory frame is given by the Doppler-shift equation:

$$E_{obs} = \frac{E_{cm}}{\gamma(1 - \beta\cos\theta)} \ . \tag{2.7}$$

Here, E_{obs} is the energy of the photon observed in the laboratory frame, E_{cm} is the transition energy in the center-of-mass frame of the moving source, $\beta = v/c$ is the speed of the moving source relative to the speed of light, and θ is the angle of the photon emission relative to the motion of the source, measured in the laboratory frame. The Lorentz factor γ is given by

$$\gamma = \frac{1}{\sqrt{1 - \beta^2}} \ . \tag{2.8}$$

The observed energy of a gamma ray depends on both the direction it is emitted and the speed of the moving source. For small angles of gamma emission (in the same direction as the motion of the source), the energy observed in the laboratory frame is increased relative to the center-of-mass energy. At large angles of emission (in the opposite direction of the moving source), the laboratory-frame energy is decreased relative to the center-of-mass. For larger speeds, the deviation from the center-of-mass energy increases at all angles, while for smaller speeds ($\beta \approx 0$), the observed energy approaches the center-of-mass energy.

In order to deduce the true decay energy of a gamma ray, a Doppler-shift correction is performed, which is the inverse of Equation 2.7:

$$E_{DC} = E_{obs}\gamma(1 - \beta\cos\theta) \ . \tag{2.9}$$

Here, E_{DC} is the Doppler-corrected energy. This correction is made using experimentally determined quantities. The angle of emission is determined by the interaction point within a

detector relative to the beam trajectory at the reaction target, and the speed of beam nuclei can be measured after the reaction.

When dealing with a gamma-ray detector used with fast beams, there are three sources of uncertainty to the final energy resolution of Doppler-corrected gamma-rays. These effects include the uncertainty in the velocity ($\Delta\beta$) of the beam, the uncertainty in the emission angle ($\Delta\theta$) of the gamma ray, and the intrinsic resolution (ΔE_{intr}) of the detector [39]. These three effects are added in quadrature to give the total energy resolution:

$$\left(\frac{\Delta E_\gamma}{E_\gamma}\right)^2 = \left(\frac{\beta \sin\theta}{1-\beta\cos\theta}\right)^2 (\Delta\theta)^2 + \left(\frac{\beta-\cos\theta}{(1-\beta^2)(1-\beta\cos\theta)}\right)^2 (\Delta\beta)^2 + \left(\frac{\Delta E_{intr}}{E_\gamma}\right)^2 . \tag{2.10}$$

These are plotted in Figure 2.5, where the relative contributions of each term are shown as a function of the angle of gamma-ray emission measured in the laboratory. The values used in Figure 2.5 are based on those used in Ref. [39]. Actual values for each term depend on the experimental conditions, but generally the effects of each term are clear from the figure. The contribution from the angular uncertainty (ΔE_θ) is largest at central angles of $\theta \approx 40°$–$100°$ and vanishes at large and small angles. The uncertainty due to the uncertainty in velocity (ΔE_β) has the opposite effect: it is largest at large and small angles, and smallest at central angles. The intrinsic energy resolution of a detector depends on the energy of detected gamma-rays. Because the Doppler-shifted energy depends on the angle, there is an angular dependence of the intrinsic resolution. This angular dependence is minimal, however, and the intrinsic resolution is smaller than the sum of the other two components at all angles. In general, all of the contributions to the uncertainty are larger at higher beam velocities, and for a stationary source only a constant intrinsic resolution is present. The sensitivity to the different components for fast beams can be exploited in well designed gamma-ray

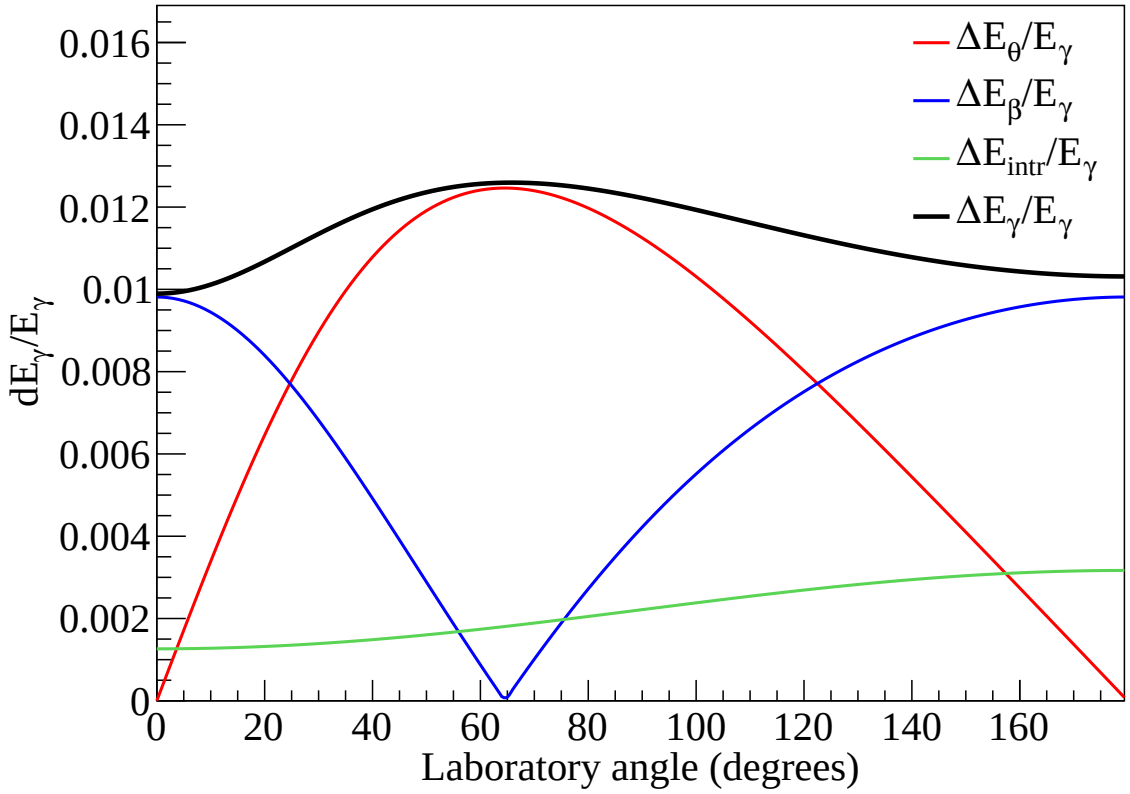

Figure 2.5: A graph showing the relative contributions the energy resolution as described in Equation 2.10. The red line shows the resolution due to the uncertainty in the angle of emission, the blue line shows the effect due to the uncertainty in velocity, and the green line shows the intrinsic energy resolution. The black line shows the total resolution when the three effects are added in quadrature. The curves are calculated with the values $\beta = 0.43$, $\Delta\beta = 0.008$, $\Delta\theta = 1.5°$, and $\Delta E_{intr} = 0.002$ MeV for a 1 MeV gamma ray in the center-of-mass frame.

measurements, and this forms the basis for the lifetime measurement techniques described in the following sections.

In many experimental cases, the Doppler-corrected energy is not necessarily equal to the center-of-mass energy of the gamma ray. Exploiting the difference between these two values is key to the lifetime measurement techniques which have been developed to study excited-state lifetimes using fast radioactive beams. The following sections discuss two techniques used in an experiment with ^{19}C which will be discussed in this thesis. The two methods, the line-shape method and the Recoil Distance method (RDM), rely on precise measurements

of Doppler-shifted gamma rays. The two methods are complementary in their sensitivity to lifetimes; the line-shape method is useful for lifetimes on the order of 100 ps–10 ns, while the RDM is better suited for shorter lifetimes on the order of 1 ps–1 ns. In addition to lifetime measurements, the theoretical framework for the one-nucleon knockout reaction is presented, which was used to produce ^{19}C in the same experiment. While the lifetime measurements were used exclusively to study the structure of the excited states in ^{19}C, the knockout reaction was used to study the ground state of ^{20}N as well as all the bound states in ^{19}C.

2.4 Line-shape Method

The first part of the experiment was based on the so-called line-shape method [46, 47]. This technique is based on the emission-point distribution of gamma rays emitted in-flight after a reaction target. For a beam with velocity βc and an excited-state lifetime τ, gamma-ray decays are distributed exponentially along the beam line, and the average decay position z along the beam line is given by

$$z = \tau\gamma\beta c \ . \tag{2.11}$$

At a velocity of $\beta \approx 0.3$, the beam moves about 1 mm in 10 ps. If the lifetime of the excited-state decay is more than 100 ps, then decays occur, on average, several centimeters downstream of the target. This shift in z results in a change in the emission angle θ of detected gamma rays. The change in the observed energy dE_γ resulting from a change $d\theta$ in the emission angle is given by

$$\frac{dE_\gamma}{d\theta} = -\frac{\beta \sin\theta}{1 - \beta\cos\theta} E_\gamma \ . \tag{2.12}$$

In the Doppler correction of experimentally observed gamma rays, the emission angle θ is calculated using the measured interaction point of the gamma ray within the detector and assuming the gamma rays are emitted from the target position. Any change in the z position cannot be taken into account in the Doppler correction, so decays that occur downstream from the target will appear in the Doppler-corrected spectrum at energies below the true decay energy. Because the decays are spread out continuously across the path of the beam, the result is a shift in the centroid of the Doppler-corrected peak as well as a tail extending to low energies. Both of these effects are increased for longer lifetimes.

The line-shape effect is demonstrated in Figure 2.6. In Figure 2.6(a), three different decay curves for lifetimes between 100 ps and 1 ns are shown for a beam exiting a target. Figure 2.6(b) shows simulated Doppler-shift corrected spectra for each lifetime. A reference spectrum for a decay with no lifetime is also plotted. The peak without any lifetime effects is narrow and symmetric, while peaks arising from the long lifetimes are shifted to lower energies and exhibit asymmetry due to long tails at low energy. As the lifetime increases, the tail becomes wider and flatter. The sensitivity of the peak shapes to the lifetime depends on the experimental conditions. For a detector which is located on the order of 10 cm from the beam line, the effect becomes noticeable when the average decay position z is at least several millimeters behind the target, which corresponds to a lifetime around 100 ps for $\beta \approx 0.3$. The upper limit of sensitivity is determined by the size of detectors, so that if the average decay position is larger than the detector size, most decays cannot be detected. In this case, the peak shape becomes flat and loses all sensitivity to the lifetime. For a detector size of several tens of centimeters, the practical upper limit of the lifetime for this method is around 10 ns.

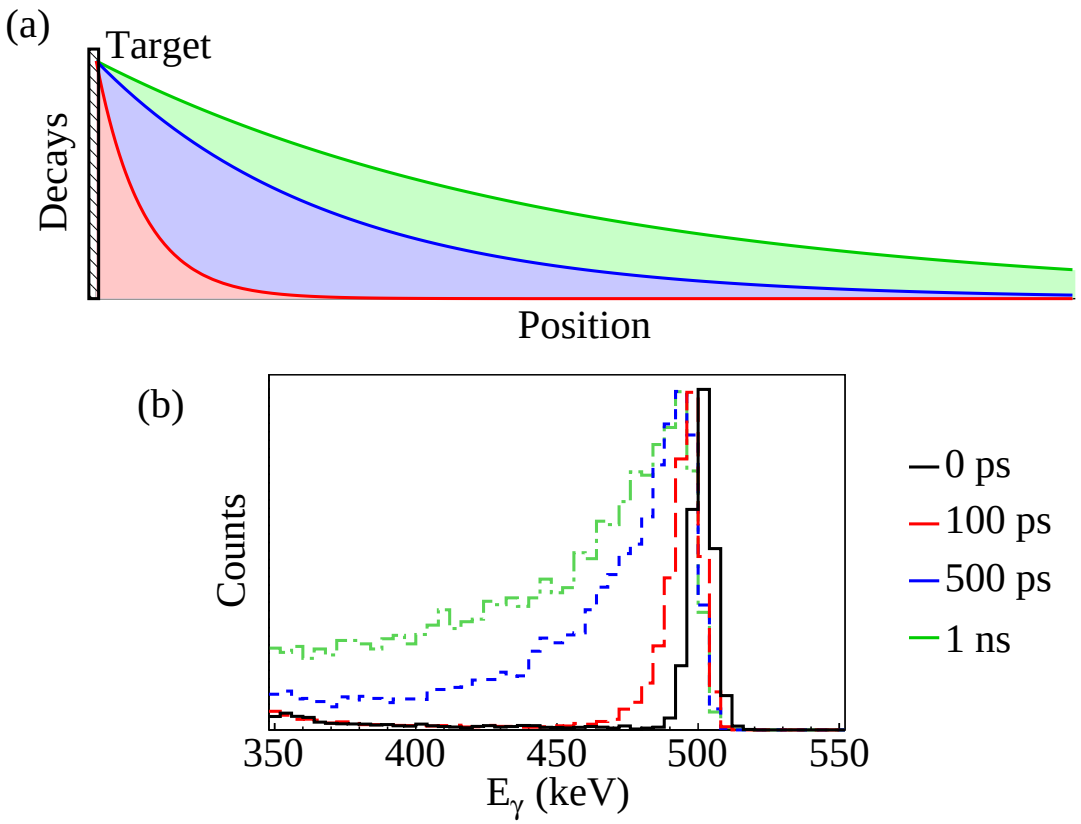

Figure 2.6: An illustration of the principles of the line-shape technique for determining lifetimes. In (a), three decay curves for lifetimes in the range of 100 ps–1 ns are shown for a beam exiting a reaction target. Simulated Doppler-shift corrected spectra corresponding to each lifetime are shown in (b), as well as a peak for a decay with no lifetime effect (0 ps). For longer lifetimes, the peak in the spectrum is shifted to lower energies, and a broad tail forms on the low-energy side of the peak.

2.5 Recoil Distance Method

The Recoil Distance Method [48] has been developed to measure the lifetime of nuclear states. The method is best suited for lifetimes between 1 ps and 1 ns (10^{-12}–10^{-9} s) [49]. Indeed, experiments using the technique have spanned this entire range [50, 51]. This section describes the principles of the Recoil Distance Method, and how it has been adapted for current experiments with radioactive beams.

The early application of the Recoil Distance Method to study nuclear lifetimes with low-energy experiments with stable beams is described in Ref. [52] and illustrated in Figure 2.7.

The method uses a device called a plunger, which holds a thin target material and a thicker stopper material, which are separated along the beam line. The distance can be adjusted by moving the stopper relative to the fixed target. A nuclear reaction occurs within the target, creating a nucleus in an excited state. The nucleus then exits the target, moving toward the stopper which is separated from the target by a well defined distance D. The reaction on the target is defined to happen at time $t = 0$, and the time of flight $t_f = D/v$ of the beam across the target-stopper separation depends on D and the velocity v of the beam after the target. If the average lifetime τ of the nuclear excited state is similar to the time of flight, then some nuclei will decay while in flight in front of the stopper, and the remaining nuclei will decay after being stopped. If a decay occurs while the beam is in flight, the gamma ray energy in the laboratory frame will be Doppler-shifted according to Equation 2.7. If the decay occurs after the beam has stopped in the target, there will be no Doppler shift in the energy. Thus two peaks appear in the Doppler-corrected gamma-ray spectrum: a shifted and an unshifted peak. The intensities of the two peaks (I_s and I_u, respectively) depend on the relative magnitudes of τ and D/v:

$$I_s = N(1 - e^{-D/v\tau}) \tag{2.13}$$

$$I_u = Ne^{-D/v\tau} \tag{2.14}$$

where N is the total number of gamma rays emitted. Measurement of the peak intensities can be made at several distances, and the ratio

$$R = \frac{I_u}{I_s + I_u} = e^{-D/v\tau} \tag{2.15}$$

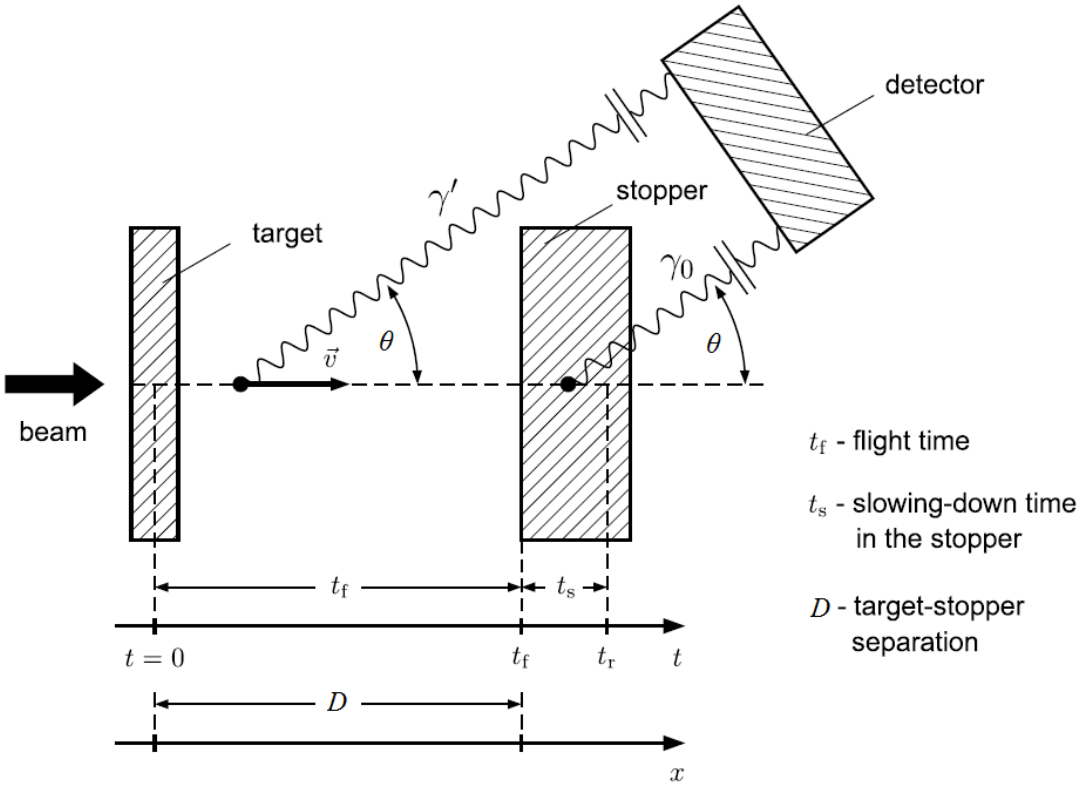

Figure 2.7: A diagram illustrating the principles of the Recoil Distance Method. After reacting inside the target, the beam travels the distance D with a time of flight t_f. Once entering the stopper, the beam slows down during time t_s, with $t_s \ll t_f$. A detector detects gamma rays emitted from an angle θ relative to the beam. Gamma rays γ' emitted during the time of flight t_f are shifted in energy, while gamma rays γ_0 emitted after the beam is stopped are unshifted, creating two peaks at different energies in the gamma-ray spectrum. The lifetime is determined from the yield of the unshifted peak relative to the total gamma-ray yield. Figure adapted from Ref. [49].

can be determined as a function of D. The slope of the exponential curve gives the value $1/v\tau$, so that τ can be determined when v is known. In a stopped-beam experiment, v is deduced from the energy of the Doppler-shifted peak [52].

With the availability of fast radioactive-beam facilities, the Recoil Distance Method has been adapted to improve its capabilities and sensitivities [49]. With beam speeds typically above $v/c \sim 0.3$, the beam can no longer be stopped within the plunger. Instead, the second foil is used as a degrader which lowers the velocity of the beam. The process is illustrated

in Figure 2.8. In this case, the principles of the method are the similar to the low-energy experiments. The degrader divides the beam into two regions: a fast region in front of the degrader, and a slow region behind it. The velocity of the beam in each region is distinct, creating two different Doppler-shifted energies. In the resulting gamma-ray spectrum, these are seen as a fast peak and a slow peak. For the original method, no Doppler correction of the observed gamma-ray spectrum is necessary, because the unshifted portion of the spectrum appears at the true decay energy. For experiments with a fast beam, however, both the fast and slow peaks in the spectrum are significantly Doppler-shifted. Thus, a Doppler-shift correction is required to recover the true decay energy. Typically, individual gamma-ray energies are corrected using Equation 2.9 by assuming the gamma rays are emitted at the fast velocity immediately after the target. With these assumptions, the fast peak is located at the true decay energy, and the slow peak becomes shifted to lower energies, because its Doppler correction is performed incorrectly.

One of the advantages of using the RDM with fast beams is the capability to detect the outgoing particles in coincidence with gamma rays. The particles can be identified on an event-by-event basis using time-of-flight and energy-loss measurements. Particle identification after the reaction allows for a reduction of background due to the elimination of beam contaminants in the final spectrum [49]. In addition, thicker targets may be used with fast beams, which allows for feasible reaction rates even for low beam intensities. There are, however, some complication in the analysis and interpretation of the data with the use of fast beams. Because of the target thickness, some decays may occur within the target or the degrader, reducing the intensity of the fast and slow peaks in the gamma-ray spectrum. At high energies, reactions of the secondary beam may also occur within the degrader, which increases the yields for the slow peak only. Thus, the lifetime cannot be extracted in

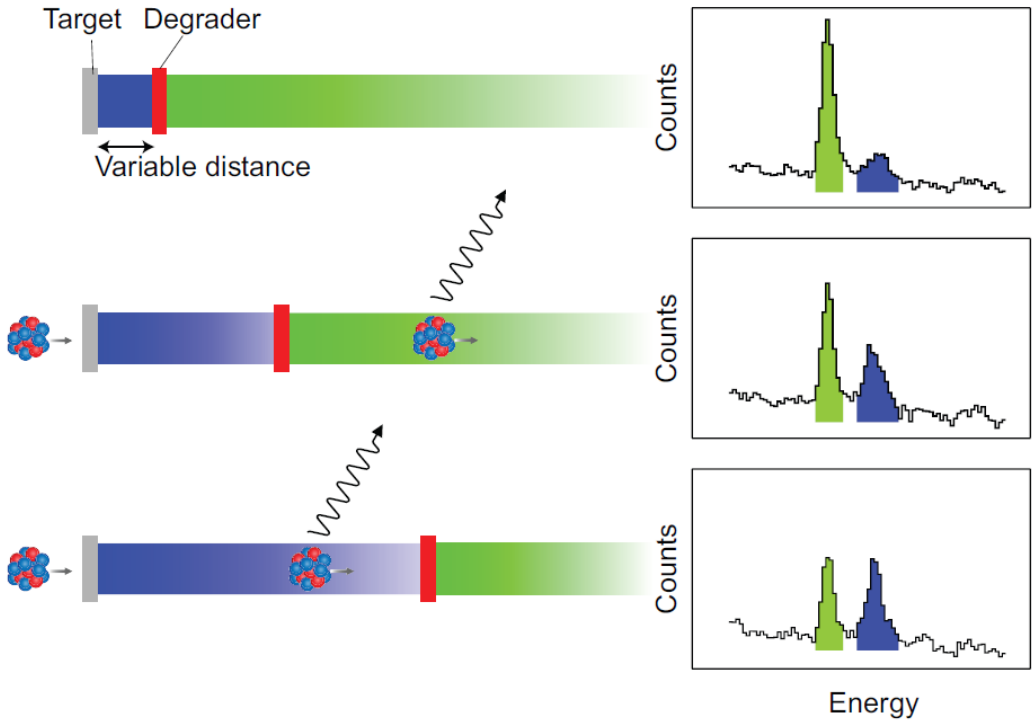

Figure 2.8: A schematic demonstrating the Recoil Distance Method used with a fast radioactive beam. The use of a degrader to slow down the beam creates fast (blue) and slow (green) regions along the beam path. As the separation of the target and degrader increases, more gamma decays occur in the fast region. The resulting gamma-ray spectra for each of the settings are shown on the right.

the manner described above. Instead, the lifetime is determined by comparing the data to simulations of the experiment.

2.6 Single-nucleon Knockout

Single-nucleon knockout reactions have become a powerful tool in the study of the single-particle structure of nuclei [23]. These are described as direct reactions, in which a proton or neutron is removed in a single step [53]. In a knockout reaction, a projectile nucleus moving at high energy, typically above ∼50 MeV per nucleon, encounters a stationary target nucleus. In the reaction, a single nucleon is removed from the projectile. In the simplest approximation of this reaction, the projectile is described as a single valence nucleon and the remaining nucleons in the projectile, where the latter components are called a core. During the reaction, the valence nucleon is removed instantaneously from the projectile while the core remains intact. Within the framework of a direct reaction, the core does not interact at all with the target, except to be elastically scattered, so that the internal configuration of the core is not changed. The knockout reaction is described theoretically in the eikonal, or Glauber model [53, 54]. Within this model, the projectile is assumed to travel in a straight line as it passes the target, and its wave function $\psi(\vec{r})$ can be separated into a plane wave and a cylindrical term:

$$\Psi(\vec{r}) = e^{ikz}\psi(b,z) \tag{2.16}$$

where the projectile moves in the z direction with momentum k, and the impact parameter b is the distance between the projectile's trajectory and the target. The Hamiltonian includes a term $V(b,z)$, which is the potential between the target and projectile. Applying the

Hamiltonian and ignoring second-order derivatives of ψ gives the eikonal equation:

$$\frac{\partial \psi}{\partial z} = -\frac{i}{\hbar v} V(b,z)\psi \ . \tag{2.17}$$

This has the solution

$$\psi(b,z) = e^{i\chi(b,z)} \tag{2.18}$$

where the eikonal phase $\chi(b,z)$ is defined as

$$\chi(b,z) = -\frac{i}{\hbar v}\int_{-\infty}^{z} V(b,z')\,dz' \ . \tag{2.19}$$

From the eikonal phase, the elastic S-matrix $\mathcal{S}$ is defined:

$$\mathcal{S} = e^{i\chi(b,+\infty)} \ . \tag{2.20}$$

The probability to scatter off of the target elastically is given by $|\mathcal{S}|^2$, and the particle can be absorbed by the target if $|\mathcal{S}|^2 < 1$, which occurs for complex potentials. To calculate knockout cross sections, the S-matrices $\mathcal{S}_c$ and $\mathcal{S}_v$ are calculated separately for the core (c) and valence (v) nucleon, respectively. For calculation of the S-matrices, the potential $V(b,z)$ is obtained by folding the target the target density, core nuclear or valence nucleon density, and an appropriate nucleon-nucleon potential. The target and core densities are usually taken to be a Woods-Saxon form, and the valence nucleon is assumed to be a point particle. The relative wave function of the valence nucleon within the core nucleus is calculated in a Woods-Saxon potential which is adjusted to match the experimental separation energy of the nucleon within the projectile.

There are mechanisms through which the projectile can react with the target: stripping and diffractive dissociation. The stripping reaction occurs when the valence nucleon is absorbed by the target nucleus, while the core is scattered with the remaining nucleons in the same state as before the reaction. This is an inelastic reaction in which the target does not remain in its ground state. The cross section for stripping is given by

$$\sigma_{str} = \frac{1}{2j+1} \int \sum_{m} \langle \psi_{jm} | (1 - |\mathcal{S}_v|^2) |\mathcal{S}_c|^2 | \psi_{jm} \rangle \, db \ . \tag{2.21}$$

Within the integral, the terms $(1 - |\mathcal{S}_v|^2)$ and $|\mathcal{S}_c|^2$ are the respective probabilities for the valence nucleon to be absorbed and the core nucleus to scatter elastically. The ψ_{jm} is the wave function of the nucleon relative to the core nucleus, and the integral is taken over the impact parameter b of the center of mass of the nucleon-core system relative to the target.

Diffractive dissociation occurs when both the valence nucleon and the remaining core are scattered elastically. Because the entire reaction is elastic, the target nucleus is left intact in its ground state. The diffractive dissociation cross section is given by

$$\sigma_{diff} = \frac{1}{2j+1} \int \sum_{m,m'} \left[\langle \psi_{jm} | | 1 - \mathcal{S}_c \mathcal{S}_v |^2 | \psi_{jm} \rangle \delta_{m,m'} - | \langle \psi_{jm'} | (1 - \mathcal{S}_c \mathcal{S}_v) | \psi_{jm} \rangle |^2 \right] db \tag{2.22}$$

This equation arises from the completeness of the bound and unbound wave functions of the scattered particles after the reaction, and avoids integration of the states in the continuum.

The total single-particle cross section σ_{sp} is the sum of the stripping and diffractive dissociation cross sections, additionally including a Coulomb breakup term σ_C:

$$\sigma_{sp} = \sigma_{str} + \sigma_{diff} + \sigma_C \ . \tag{2.23}$$

The Coulomb breakup term is due to a strong Coulomb force from high-Z targets and is not important for light targets, as is the case for the current work.

The single-particle cross section is applicable only for pure single-particle states. Actual cross sections must be corrected to account for the mixture of different configurations in the wave function. These different configurations in both the initial and final wave functions mean that different nucleons may be removed to give the final state. The relative contributions for removal of the various nucleons is given by a spectroscopic factor. The spectroscopic factor is calculated from the overlap of the wave functions of the initial projectile with A nucleons Ψ_i^A and the core wave function with $A-1$ nucleons Ψ_f^{A-1}:

$$\langle \Psi_f^{A-1} | \Psi_i^A \rangle = \sum_{n\ell j} c^{fi}(n\ell j)\psi_{n\ell j} \tag{2.24}$$

where $\psi_{n\ell j}$ is the normalized wave function for the valence nucleon with quantum numbers $n\ell j$, and each of the $c^{fi}(n\ell j)$ is a coefficient of fractional parentage which describes the relative contribution of each single-particle wave function to connect the initial and final nuclear states. The spectroscopic factor $S^{fi}(n\ell j)$ is then given by

$$S^{fi}(n\ell j) = \left| c^{fi}(n\ell j) \right|^2 \ . \tag{2.25}$$

The spectroscopic factor can be described as the probability that the projectile in an initial state Ψ_i^A will form a core in a final state Ψ_f^{A-1} by removing a nucleon with quantum numbers $n\ell j$. For removal of a nucleon occupying a pure single-particle state, $S^{fi}(n\ell j) = 1$, and for removal of a nucleon from a fully filled orbital, $S^{fi}(n\ell j) = 2j+1$, which reflects the total number of available nucleons in the orbital. If the spectroscopic factor is calculated in the

isospin formalism, it must be replaced by $C^2S(n\ell j, T)$, usually simply written as $C^2S(n\ell j)$, where C is an isospin Clebsch-Gordan coefficient. Finally, if the spectroscopic factor is calculated in a harmonic oscillator basis, there is an additional center-of-mass correction $[A/(A-1)]^N$ which must be applied [55], where $N = 2n + \ell$ is the major oscillator shell of the removed nucleon.

In an actual knockout experiment, the initial state of the projectile is fixed, and it is sufficient to denote the spectroscopic factor to the final state of the core with $S(J^\pi, n\ell j)$. The total cross section σ_{th} to a given final state is given by

$$\sigma_{th} = \sum_{n\ell j} \left[\frac{A}{A-1}\right]^N C^2S(J^\pi, n\ell j)\sigma_{sp}(n\ell j, S_n^{eff}) \ . \tag{2.26}$$

This cross section is an incoherent sum of all single-particle cross sections for the nucleon wave functions which can connect the initial projectile and final core states, normalized by each of the spectroscopic factors. In general, both the stripping and diffractive dissociation cross sections are calculated based on removing a nucleon with an effective separation energy S_n^{eff}:

$$S_n^{eff} = S_n + E_x(J^\pi) \ . \tag{2.27}$$

The effective separation energy is based on the separation energy S_n of the removed nucleon from the ground state of the projectile nucleus, and leads a state J^π in the final nucleus with excitation energy $E_x(J^\pi)$.

Chapter 3

Experimental Devices

The present experimental work was performed at the National Superconducting Cyclotron Laboratory (NSCL) at Michigan State University. In experiments at the NSCL, a primary beam of stable nuclei is accelerated by the Coupled Cyclotron Facility (CCF) [56] in order to produce a radioactive secondary beam. The secondary beam is analyzed and purified by the A1900 fragment separator [57] and delivered to the experimental area. Secondary reactions with the radioactive beam occur on a target in the experimental area, and final reaction products are separated and identified by the S800 spectrograph [58]. The details of each of the experimental steps are described in the following sections.

3.1 Beam Production

At the NSCL, radioactive ion beams are produced as reaction products of stable beams on a stable target. The acceleration of the stable beam begins with the ionization of stable isotopes. The NSCL has two machines which perform this function, the Superconducting Source for Ions (SuSI) [59, 60] and the Advanced Room Temperature Ion Source (ARTEMIS-B) [61]. In both cases, the beam is extracted from a stable source and injected into a plasma for ionization. Gaseous species are extracted directly from a gas source, while solid sources are heated in an oven so that the atoms evaporate into the air. Within the plasma, the stable atoms are ionized through multiple collisions with energetic electrons which are

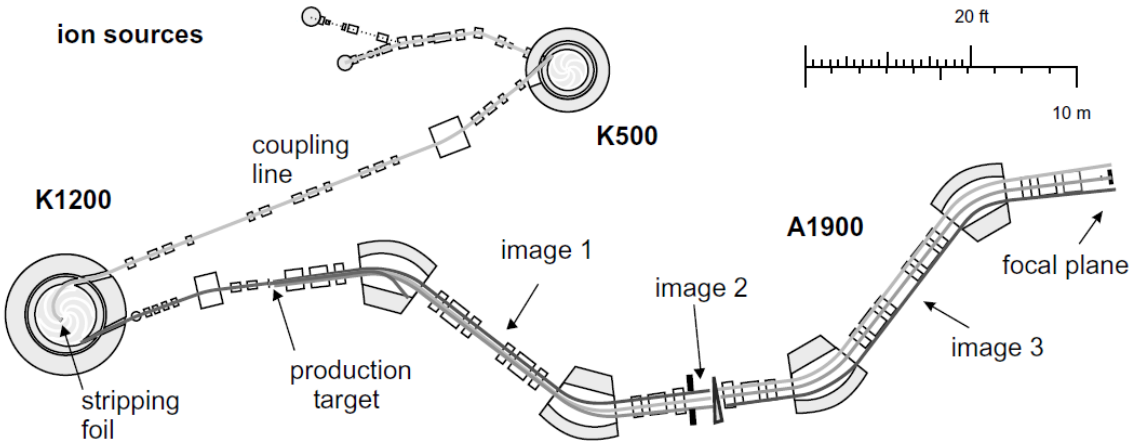

Figure 3.1: The Coupled Cyclotron Facility at the NSCL. A stable beam is created at an ion source and accelerated in the K500 and K1200 cyclotrons. The beam then reacts at the production target to create a radioactive secondary beam. The secondary beam continues through the A1900 and is then sent to the experimental area. Figure adapted from Ref. [57].

accelerated using electron cyclotron resonance. In this method, the electrons in the plasma are accelerated by applying microwave radiation, and the electrons are confined to a circular orbit by a constant magnetic field. The process can be understood by equating the Lorentz force on a moving electron in a magnetic field and the centripetal force of the resulting circular motion:

$$qvB = \frac{\gamma m_e v^2}{\rho} \ . \tag{3.1}$$

Here, q is the charge of the electron, v is the velocity of the electron perpendicular to the magnetic field, B is the magnetic field strength, m is the electron's mass, and ρ is the radius of rotation. Rearranging this equation yields the cyclotron frequency ω_c:

$$\omega_c = \frac{qB}{\gamma m_e} \tag{3.2}$$

which, in the classical limit, is independent of the energy of the electron and the radius of motion, allowing the plasma electrons to be excited many times at the same electromagnetic

frequency. After being ionized, the stable atoms are sent to the Coupled Cyclotron Facility for acceleration.

The Coupled Cyclotron Facility [56] comprises two cyclotrons: the K500 and K1200. These can be seen on the left side of Figure 3.1. The partially ionized atoms are first injected into the K500, where they are accelerated based on the cyclotron motion of the ions. The ions are confined within the cyclotron by a magnetic field, and accelerated between three sets of electrodes with radio-frequency alternating electric fields. As the ions gain energy, they remain in circular motion due to the magnetic field, but the radius ρ of their orbit increases with increasing energy:

$$\rho = \frac{\gamma m v}{qB} \ . \tag{3.3}$$

Once the beam reaches the maximum energy of about 10–15 MeV/nucleon, or the velocity $v/c \approx 0.15$, it exits the K500 through a port on the outer edge of the cyclotron. The beam is transported through a coupling beamline to the entrance of the K1200 cyclotron, where a thin carbon foil removes all or most of the remaining electrons. After entering the K1200, the acceleration process begins again, and the beam is accelerated up to a final energy of 100–200 MeV/nucleon, or $v/c \approx 0.5$.

After the ion beam is fully accelerated by the cyclotrons, it is ejected from the K1200 and impinged on a production target to produce several radioactive species. Radioactive ions are produced in the target primarily through projectile fragmentation of the stable beam nuclei. During the projectile fragmentation process, a prefragment is first produced in an excited state. After the reaction, nucleons are statistically emitted from the prefragment, resulting in a final fragment with any number of protons or neutrons fewer than the incident nucleus. After emerging from the target, the beam is composed of many different nuclear species,

including stable and radioactive species. This is shown in Figure 3.2(a), which shows an example of all the nuclei produced by fragmentation of a stable beam of ^{86}Kr, drawn on the chart of nuclides. To produce the secondary beam that is suitable for experiments, the desired isotope must be filtered from all the remaining fragmentation products. This is done through isotopic separation of the beam [62]. The beam is directed into the A1900 fragment separator [57], which consists of four superconducting dipole magnets as well as an aluminum wedge which together achieve isotopic separation. In the first step of separation, the secondary beam passes through the first two magnets, which achieve separation based on the magnetic rigidity $B\rho$ of the beam. Based on Equation 3.3, the magnetic rigidity of the beam is

$$B\rho = \frac{\gamma m v}{q} \tag{3.4}$$

which depends on the momentum γmv and charge q of the nucleus. Because the velocity of the particles remains nearly constant during fragmentation reactions, the magnetic rigidity selection is essentially a selection in the mass-to-charge ratio A/Z of the beam [62]. The result of this can be seen in Figure 3.2(b), which shows the nuclei along a line of constant A/Z which pass through the first two dipole magnets of the A1900. The next stage in separation occurs through the use of an aluminum degrader located between the second and third magnets of the A1900. The degrader is in the shape of a wedge to provide a variable thickness which is adjusted for each experiment. This is used to selectively decrease the velocity of the products. The energy loss of a heavy charged particle through a material is given by the Bethe-Bloch formula [44]:

$$\frac{dE}{dx} = -\frac{4\pi e^4 q^2}{mv^2} NZ \left[\ln \frac{2mv^2}{I} - \ln\left(1 - \frac{v^2}{c^2}\right) - \frac{v^2}{c^2} \right] . \tag{3.5}$$

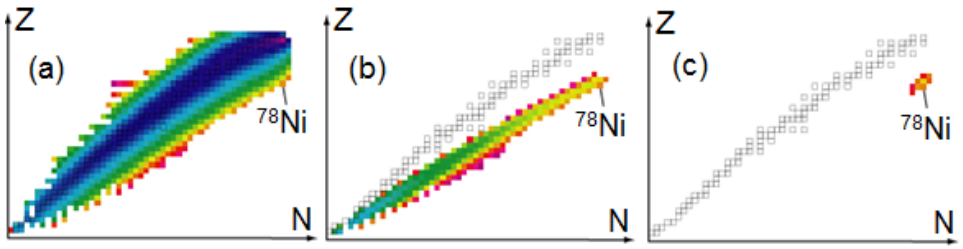

Figure 3.2: The production rates of nuclei following the fragmentation of an energetic ^{86}Kr beam at various points in the A1900. Part (a) shows the production rate immediately after the production target. Part (b) shows the rates after the first selection based on the magnetic rigidity of the beam. The straight line of accepted nuclei represents the constant A/Z ratio which is isolated after traveling through the first two dipole magnets of the A1900. Part (c) shows the transmitted beam at the end of the A1900, where there is a clear selection of the mass and charge of interest.

Here, q, m, and v are the charge, mass, and velocity of the heavy particle. Z is the atomic number of the surrounding material, and I is an empirically determined parameter which represents the average ionization potential of the material. After passing through the final two magnets, the beam is again separated by magnetic rigidity. In this case, the particles do not have the same velocity, and the beam is selected based on a constant ratio of $A^{2.5}/Z^{1.5}$ [62]. This is seen in Figure 3.2(c), where the final acceptance is limited to a small range of nuclei. For a given experiment, the magnetic fields and degrader thickness are adjusted to produce a secondary beam with the optimal balance of energy, intensity, and purity.

3.2 TRIPLEX device

At the main experimental area, the TRIple PLunger for EXotic beams (TRIPLEX) [63] was used to provide a target and degrader. This device was recently developed for lifetime measurements at the NSCL. The TRIPLEX is a modified version of the so-called single plunger and can hold up to three metal foils. The addition of a second degrader allows for new types of lifetime measurements and extends the sensitivity to lifetimes [63, 64]. A photo

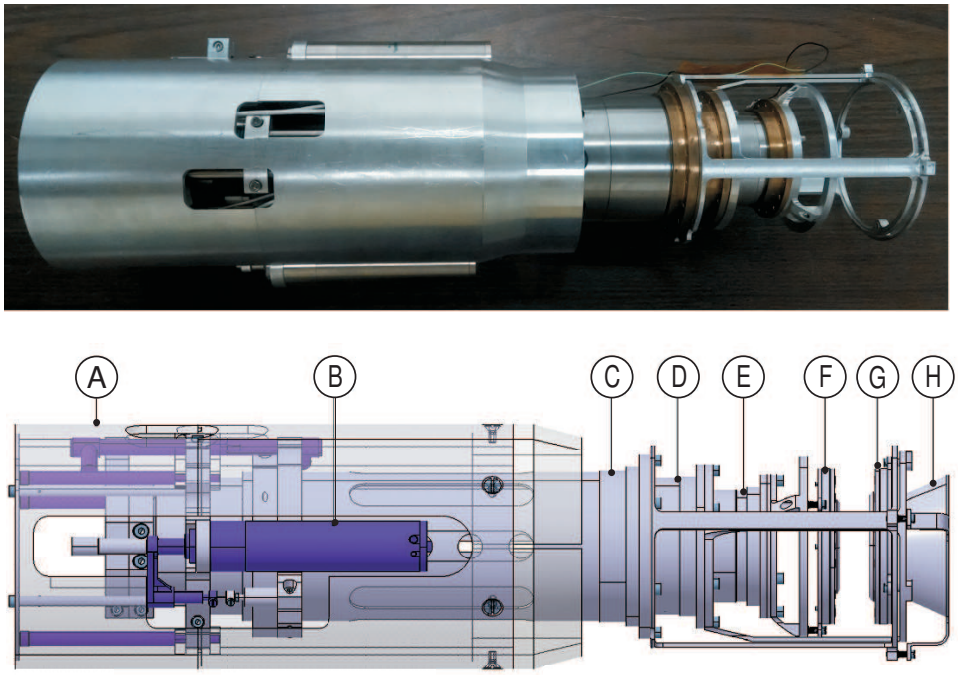

Figure 3.3: A picture of the TRIPLEX plunger at the NSCL, with a diagram on the bottom. The diagram shows the various components: (A) the outer support frame, (B) one of the motors, (C) the outer tube which connects to the second degrader, (D) the central tube which connects to the first degrader, (E) the inner tube which connects to the target, (F) the target cone, (G) the first degrader cone, and (H) the second degrader cone. The radioactive beams enters the plunger from the left and encounters the foils on the far right. The picture shows the plunger with the foil frames removed. Figure from Ref. [63].

of the TRIPLEX device and a corresponding labeled diagram are shown in Figure 3.3. The TRIPLEX consists of three main parts: a support structure, bearing unit, and foil unit. This section describes each part of the plunger as well as its experimental operation.

The support structure consists of an outer frame which is attached to an inner support ring as well as a dedicated vacuum pipe which houses the TRIPLEX plunger during experiments. The support ring is the foundation for all of the immobile components in the plunger. These include the central plunger tube which holds the first degrader foil and the motors which move the inner and outer tubes. During experiments, the plunger is placed within the vacuum pipe as shown in Figure 3.4. Six screws hold the outer frame in place and can be adjusted to align the plunger foils to the beam path. The beam chamber also contains

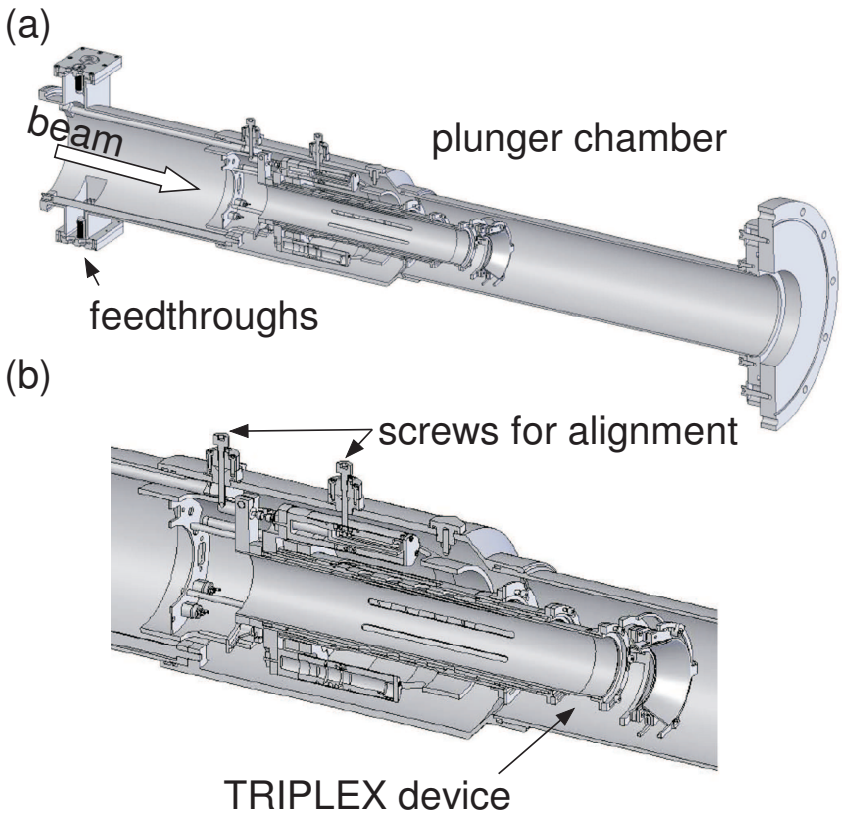

Figure 3.4: The TRIPLEX plunger located inside the dedicated vacuum chamber. Electrical feedthroughs for control and monitoring of the device are visible in (a). The close-up view in (b) shows the screws which are used to align the plunger to the beam path. Figure from Ref. [63].

two sets of electrical feedthroughs, which allows the cabling for control and monitoring of the plunger to be connected through the beam pipe.

The bearing unit of the plunger comprises three concentric tubes which attach to the three plunger foils. The tubes can be seen in Figure 3.5. The middle tube is attached to the inner support ring and is fixed in place. The inner and outer tubes are held in place by four sliding bearings which are attached to the middle tube. The inner and outer tubes can be moved along the central axis to adjust the foil distances, and are attached to two independent motors. Each motor is connected to the tube via a small wire attached to a ring clamped around each movable tube. This allows the tubes to be moved without

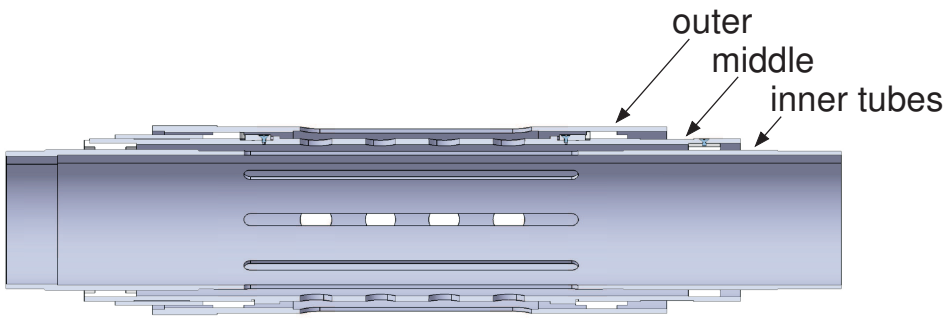

Figure 3.5: The three tubes which comprise the bearing unit of the TRIPLEX plunger. The stationary middle tube is attached to the inner support ring and connects to the first degrader foil. The inner and outer tubes move along the beam direction and connect to the target foil and second degrader foil, respectively. Figure from Ref. [63].

introducing any radial force which could deform the tubes. The movable range of each motor is approximately 2.5 cm.

The foil unit is located at the downstream end of the TRIPLEX and can be seen on the right side of Figure 3.3. At the end of each tube is a brass ring which holds a frame to mount the target and degrader foils. Each foil is mounted on a specially shaped cone. The cones are attached by small screws and are held in place by springs. The compression of each spring is adjusted to ensure alignment of the foil faces. As seen in Figure 3.3, the second-degrader cone has a longer, narrow shape which fits inside the first-degrader cone so that the second-degrader foil can come into contact with the first-degrader foil. This requires that the second-degrader foil be cut into a circle to fit. However, there is no such fitting requirement for the target and first-degrader foils, so these are usually square-shaped. The inner diameter of the second degrader is about 4.6 cm, which is large enough for all of the radioactive beam to pass through.

Accurate positioning of the plunger foils is vital for recoil distance experiments, especially for short-lifetime measurements. The positions of the target and second degrader foils are determined from three independent measurements. First, the motors which control the

motion of the inner and outer tubes provide the displacement information of the tubes with sub-μm resolution. The maximum range of each motor is approximately 3 cm; however, depending on the configuration of the foils, the achievable foil separation is usually reduced to 2.5 cm. Additionally, two micrometer probes have been installed in the plunger support which measure the displacement of the inner and outer tube rings over a small distance. These probes have a range of only about 2 mm, much smaller than the total range of the motors, but have a similar measurement precision. However, these can be used to verify the motor displacement readings at small distances, where the accurate measurement is most important. It has been found that the probes show small deviations in the displacement on the order of 5 μm at the edge of their ranges. Therefore, these are only used in a limited context for distance verification. The final method to determine foil separation is based on capacitance measurements. Individual foils are electrically isolated from each other and from the rest of the plunger. Therefore, two foils placed at small distances from each other act as a parallel plate capacitor. The position of the foils where electrical contact occurs defines the setting for zero distance of the foils. Any offset from the true zero distance is determined through by measuring the capacitance at several distances near the zero-distance setting. A voltage pulse is sent into the first degrader, and the induced voltage in the target or second degrader is read out. For a parallel plate capacitor, the capacitance, and therefore the induced voltage, is inversely proportional to the foil separation. A fit to the calibration determines the point at which the induced voltage diverges, and the difference between this point and the zero-distance setting obtained from the electrical contact determines the offset for the true zero distance. This calibration must be done for each experiment and each set of target and degrader foils. The offset for a typical experiment is on the order of 10 μm. The capacitance measurement also serves as a way to align the foils. By adjusting the

compression of the springs, the capacitance between two adjacent foils can be maximized, and the maximum capacitance corresponds to the best parallel alignment.

3.3 Gamma-ray detection

Gamma rays emitted from the recoiling nuclei were detected by the Gamma-Ray Energy Tracking In-beam Nuclear Array (GRETINA) [40]. GRETINA consists of 7 detector modules, each with 4 high-purity germanium crystals. Each crystal has a deformed hexagonal face, and the faces are designed to fit around a sphere with a radius of 18 cm. The detector crystals are each about 7 cm wide and 9 cm deep, and adjacent crystals within each module have less than a 2.7 mm gap between them. The arrangement of the four crystals within each module can be seen in Figure 3.6(a), which shows the two types of hexagons used. The 28 crystals covered a solid angle of 1π, or about 25% of the sphere. A picture of the GRETINA crystals surrounding the beam pipe is found in Fig. 3.7. The picture shows how the hexagonal crystals fit together around the sphere.

GRETINA represents a large advance from previous detectors because of its excellent position and energy resolution. Because of the strong dependence of the observed energy on the emission angle (Equation 2.7), determination of the gammay-ray interaction position within the crystal is vital in determining the rest-frame energy of the gamma ray. For GRETINA, the typical position resolution achieved is about 2 mm, corresponding to an angular resolution of about 10 mrad. This resolution is achieved through the use of electrical segmentation of the detector crystals. Each detector has 36 individual electrical contacts around the outside of the crystal. These are arranged in six rows along the length of each crystal, and six sections around the edges. The segmentation pattern is shown in Figure 3.6(b). When

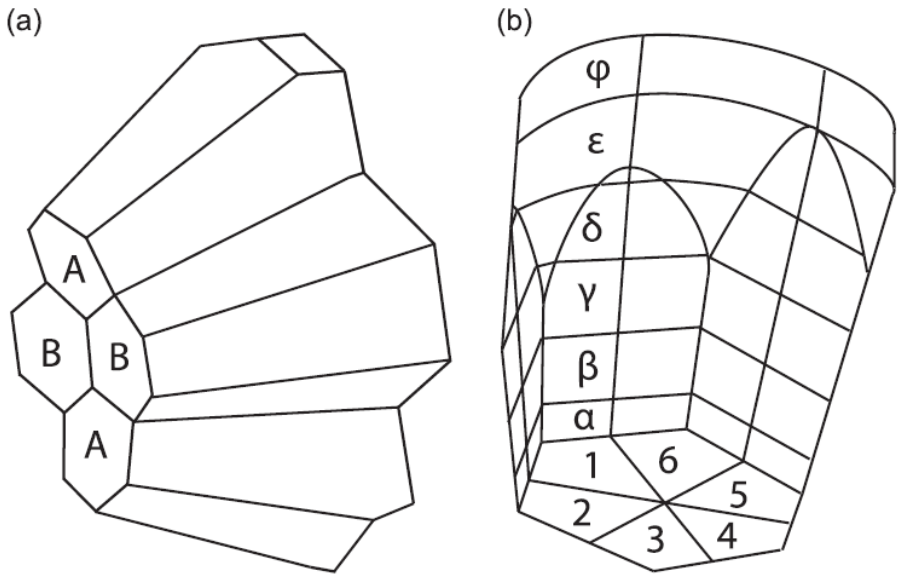

Figure 3.6: The design of the detector crystals in GRETINA. Part (a) shows the two shapes used to fit the detector faces around a circle. Part (b) shows how each crystal is electrically segmented into six radial sections and six layers deep, creating 36 individual segments used for position resolution. Figure adapted from Ref. [40].

an interaction occurs in one section, the released electrons are all collected at a single anode. The total charge collected is then read off from that anode. Additionally, anodes in adjacent segments will record image charges if the electrons are collected near that segment. The relative size of the image charges on adjacent segments depends on the location of the gamma-ray interaction. Algorithms used by the GRETINA software can reconstruct the original interaction position within the segment based on the image charges of adjacent segments. A cylindrical bore through the center of each crystal contains the central contact in the middle of each crystal which records the total energy deposited.

GRETINA was designed specially for gamma-ray tracking, which is the reconstruction of the path of the gamma ray after multiple Compton scattering events. The tracking process is done in several steps. First, individual interaction points are grouped according to the likelihood that they came from the same photon originating from the target. Within the

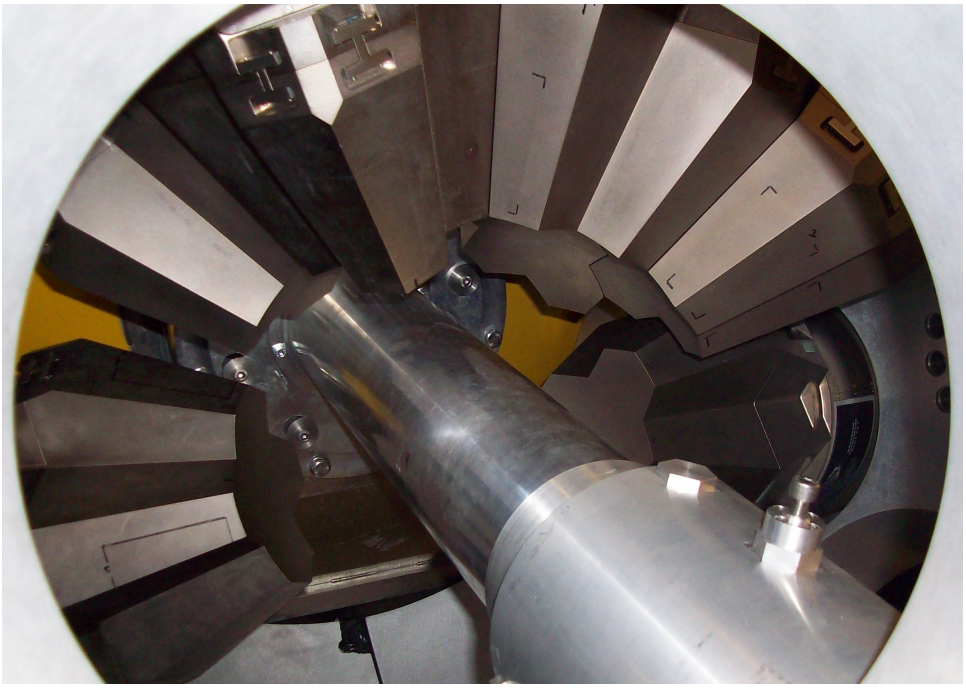

Figure 3.7: The beam pipe used in the experiment showing the GRETINA clusters around the downstream portion. The detectors on top show how adjacent modules fit together. The radioactive beam comes in from the bottom right.

group, the ordering of the interactions is determined by comparing every possible sequence of interactions using the Compton equation (Equation 2.2). In the case of ^{19}C, there is only a single gamma ray near 200 keV. At the current beam energy with the positioning of GRETINA and the TRIPLEX, the resulting in lab-frame energies were between 100 and 300 keV. At these energies, most gamma rays deposit all of their energy in a single photoelectric event, and very few gamma rays are Compton scattered. Therefore, tracking was not implemented in the analysis of ^{19}C data, since tracking is designed to reconstruct Compton-scattered gamma rays. Instead, the data were cut on a gamma-ray hit multiplicity of one, meaning only those events with a single hit in GRETINA were used. This had the effect of reducing the gamma-ray background without significantly reducing counts in the peak.

3.3.1 Calibrations

Calibration of GRETINA serves two purposes. First, the energy calibration ensures that the signals read out from the detectors correspond to the true energy deposited by gamma rays in the detector. This is done by using standard sources: small samples of radioactive isotopes which emit gamma rays at well known energies. After a source has been measured with the detectors, the signal responses can be fitted with a polynomial to map each detected peak to the correct energy. This is done for each crystal of GRETINA, since the central contact of each crystal reads out the total energy for that crystal. For the current experiment, no corrections needed to be made to the read-out energies, because the experiment was run in the middle of a long campaign with GRETINA, so the detectors were maintained in a calibrated state.

The second purpose of the calibrations is to perform a measurement of the efficiency of the detectors which provides an essential calculation of the probability of detecting gamma rays as a function of their energy. The efficiency calibration is vital to the knockout reaction measurement, because calculation of exclusive cross sections to excited states depends on precise knowledge of the detection efficiency. For proper efficiency calibration, two pieces of information are necessary: the total activity of the standard source and the relative intensity of each of the gamma rays of the isotope. In this experiment, two standard sources, ^{133}Ba and ^{152}Eu, were used for the efficiency calibration, which exhibit several gamma-ray peaks in the region below 500 keV. The measured efficiency for two different TRIPLEX configurations are shown by the red and blue points in Figure 3.8. Additionally, simulated efficiencies are shown by the black points. The process for simulating the efficiencies is described in Section 3.5. Figure 3.8(a) shows the efficiency measured in the line-shape configuration with

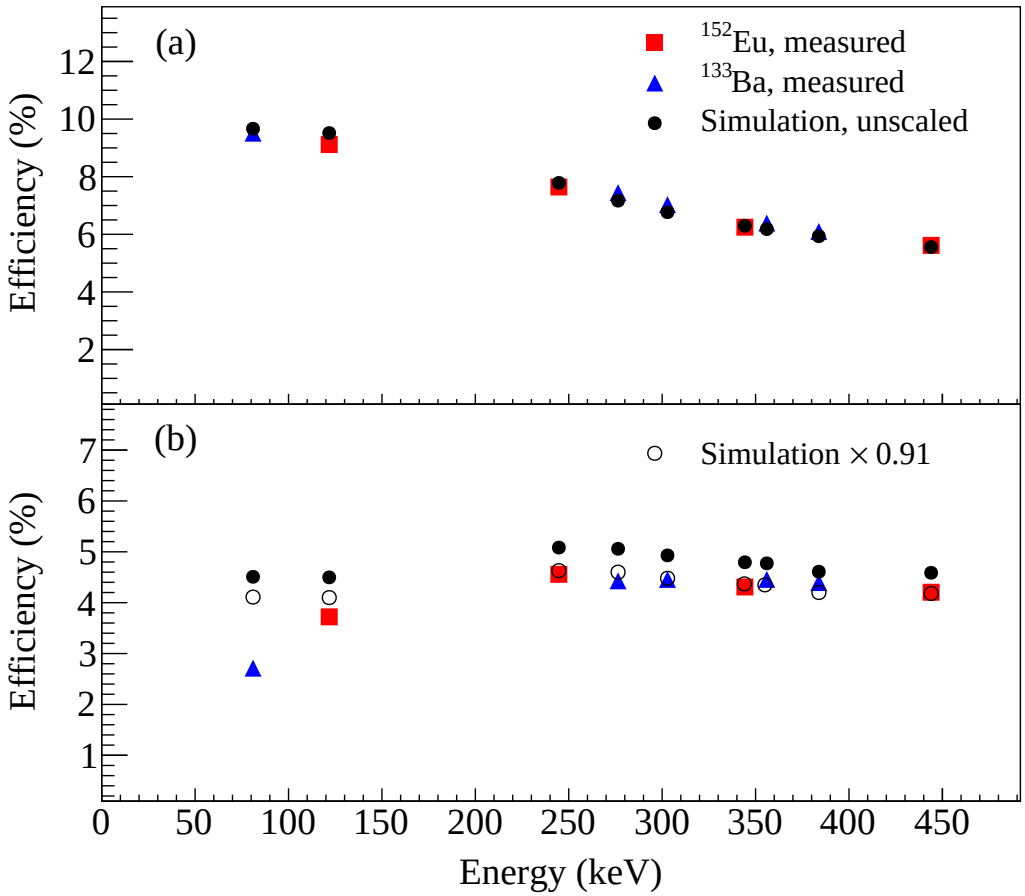

Figure 3.8: Results of the efficiency calculations using (a) the line-shape configuration with a single beryllium target, and (b) the Recoil Distance Method setup, with a beryllium target and two tantalum degraders. The standard sources include ^{152}Eu (red squares) and ^{133}Ba (blue triangles) for gamma rays below 500 keV. Simulated efficiencies are compared to the data in black. Unscaled simulated efficiencies are shown by solid circles, and in (b), the open circles show the simulation scaled by 0.91. Only the efficiency for the line-shape setup is used in the calculation of partial cross sections in the knockout reaction study.

only a beryllium foil placed in the target position of the TRIPLEX. Figure 3.8(b) shows the efficiency measured with a beryllium target, tantalum first degrader, and tantalum second degrader attached to the TRIPLEX. This second configuration was not used to take data in the current experiment, but matched the settings used for a similar experiment with ^{17}C [51]. In both cases, the calibration is taken with the source attached to the downstream edge of the target. In Figure 3.8(b), there is a sharp drop in efficiency at energies below 120 keV due to the strong attenuation of gamma rays through the thick degraders which are not present

in the previous setting.

3.4 Charged-particle Detection

After the secondary beam reacts in the TRIPLEX target, recoiling products are detected in the S800 spectrograph [58]. The primary function of the S800 is to identify particles through position, momentum, and timing measurements. The S800 achieves this through its suite of particle detectors. In the present work, the momentum of the recoiling ^{19}C particles was also used to quantify the knockout reaction from the ^{20}N secondary beam. This section describes the details of the particle detectors in the S800 and the calibrations used to make measurements.

3.4.1 S800 Spectrograph

The layout of the S800 can be seen in Figure 3.9. The S800 consists of two parts: an analysis line and the spectrograph itself. The radioactive secondary beam enters the analysis line from the A1900 and is sent to the experimental area. Final products are collected in the focal plane at the end of the spectrograph. The S800 can operate in two distinct modes. In the focused mode, the beam is focused at the target position, while at the focal plane the beam is dispersed based on the energy spread of the reaction products. In this mode, there is a large acceptance ($\pm$2.5%) of the incoming momentum, but the total energy resolution is limited by the momentum width. In dispersion matched mode, the beam is dispersed at the target position. This lowers the momentum acceptance of the S800 to $\pm$0.25%, but significantly increases the energy resolution.

The S800 achieves particle identification measurements through a large array of particle

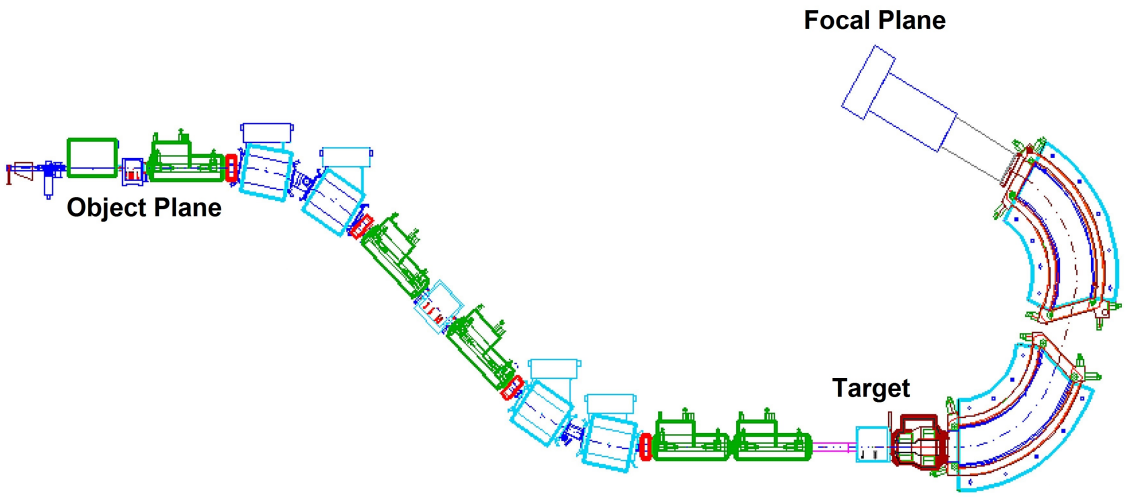

Figure 3.9: The S800 spectrograph. The secondary beam arrives from the A1900 at the object plane, and is sent to the target area, where the experimental target and detectors are located. After the target, final products are sent through spectrograph and analyzed in the focal plane. Figure from Ref. [65].

detectors [66]. At the object plane of the S800 (see Figure 3.9) is a plastic timing scintillator which records the timing of each incoming secondary beam particle. After the target, there are two dipole magnets which separate the final reaction products from unreacted secondary beam nuclei by their magnetic rigidity. The focal plane of the S800 is located after the magnets, and several detectors are located there which provide identification of final products after reaction of the secondary beam. A diagram of the focal plane detectors can be seen in Figure 3.10. A Cathode Readout Drift Chamber (CRDC) is located at the focal plane position and measures the position of particles at the focal plane. A second CRDC located one meter downstream of the focal plane is used in conjunction with the first CRDC to provide the full trajectory of beam particles after the target. After the CRDCs is an ionization chamber which records the energy loss of the beam. Immediately after the ionization chamber is an E1 scintillator, which provides a time-of-flight measurement from the object

plane scintillator and is used as a trigger for the S800 readout. Behind the E1 scintillator, a hodoscope composed of of 32 CsI(Na) crystals can be used for charge-state identification of the stopped beam. All of these detectors provide event-by-event particle identification, meaning that each particle that reaches the focal plane of the S800 is individually recorded.

3.4.1.1 Timing Scintillators

Within the S800, beam particles encounter two plastic scintillator detectors. When a charged particle moves through a scintillator, molecules within the plastic are excited as electrons are knocked out by the energetic particles. The molecules then decay back into the ground state, emitting photons. This light is collected at the ends of the detector by a photomultiplier tube, which records the total light output. While these detectors have poor energy resolution, they have very good timing resolution. These are therefore used to measure the time of flight of the beam across the S800. The time of flight of the reaction products measured between the object scintillator and the E1 scintillator can be understood from the magnetic rigidity of the S800 spectrograph:

$$B\rho = \frac{\gamma m v}{q} \approx \frac{Av}{Z} = \frac{A}{Z}\frac{d}{T} \ . \tag{3.6}$$

Because each nucleus travels the same distance d between the scintillators, for a given magnetic rigidity, the time T taken by each particle is proportional to A/Z. Therefore, the time-of-flight measurement is used with Z-identification to determine the final reaction products. The A1900 has similar timing scintillators which are used to identify the incoming secondary beam.

3.4.1.2 Cathode Readout Drift Chambers

At the focal plane are two CRDCs, which each measure the x (dispersive) and y (non-dispersive) positions of the reaction products. These detectors are shown in Figure 3.10. Each detector has an active area of 30×59 cm^2 and a depth along the central beam axis of 1.5 cm, and the two detectors are separated by a distance of 1 m along the beam line. The CRDCs are filled with a gas mixture of 80% CF_4 and 20% C_4H_{10}. As a beam particle passes through the gas, it knocks out electrons, ionizing the gas molecules. The electrons then drift across an applied electric field and are collected by an anode wire oriented along the x direction. The anode wire is arranged along a series of 224 cathode pads, and the x position is determined by reading the induced charge on the cathodes caused by the accumulating electrons. A charge is induced on several adjacent pads, and there are different ways to determine the position where the beam particle passed through. In this work, the position is calculated by calculating the weighted average of the induced charge location. In the analysis, the pad with the highest induced charge is found, and the average position of the induced charge is calculated using the five pads on either side of the central pad, with each pad weighted by their induced charge. The distribution of charges can also be fit using a Gaussian distribution, with the centroid of the fit used as the x position. The y position is determined from the drift time of the electrons moving toward the anode. This is measured relative to the timing signal from the E1 scintillator. Once the x and y positions of the beam particles are known at both CRDC locations, the angle of the beam path along each direction can be calculated. The position and angular information from the CRDCs is used to calculate the beam path at the target location. This is described in Section 3.4.1.4.

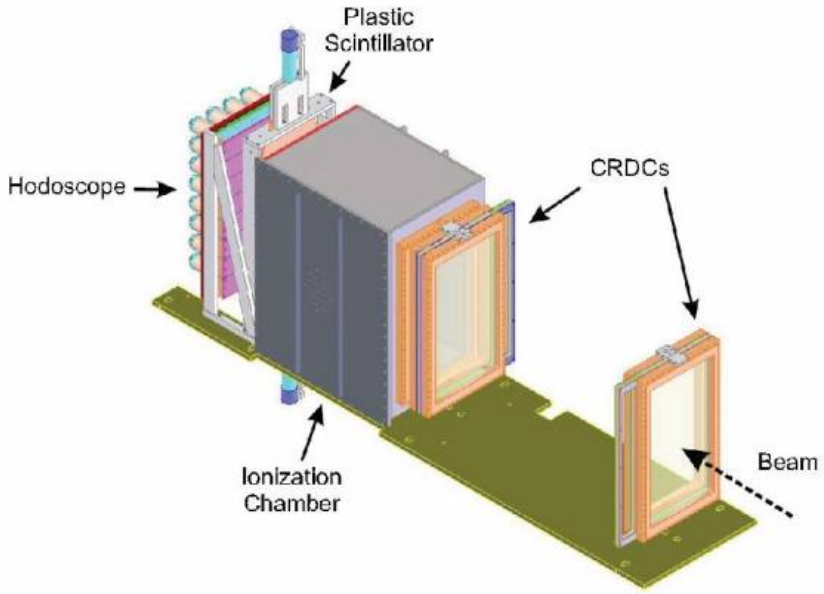

Figure 3.10: The focal plane detectors of the S800. The CRDCs measure the x and y positions of the beam relative to the central axis. The ionization chamber measures energy loss, and the plastic E1 scintillator measures the time of flight of the beam and is used as a trigger. The hodoscope behind the scintillator can be used to tag long-lived decays, but was not used in the present work. Figure from Ref. [67].

3.4.1.3 Ionization Chamber

An ionization chamber to measure the energy loss of beam particles is located behind the second CRDC. The chamber is a gas-filled detector about ten times as thick along the beam path as the CRDCs. It is filled with P10 gas, which consists of 90% Ar and 10% CH_4. Just like in the CRDCs, beam particles lose energy across the detector through collisions with gas molecules, creating ions by knocking out electrons. The gas is surrounded by 16 anode-cathode pairs which collect the electrons and gas ions, and the total amount of charge collected is proportional to the energy loss of the beam. For a fully ionized particle, the energy loss of beam particles is proportional to the square of the atomic number of the

particle (Equation 3.5), and the energy loss serves as a Z-identification of final products. This is used in combination with the time of flight measured by the scintillators to uniquely identify the mass and charge of all particles in the S800.

3.4.1.4 Trajectory Reconstruction

Determination of the beam position and angle at the location of the reaction target is necessary for proper Doppler correction of the gamma-ray spectrum. The lab-frame energy of emitted gamma rays depends on the angle of emission relative to the motion of the moving source nucleus as well as the speed of the source. Therefore, Doppler correction of observed gamma rays depends on both the location of the gamma ray interaction within the detector and the direction of the moving nucleus. Determination of the beam trajectory at the target location is done using the code COSY Infinity [68] and is based on the position measurements from the CRDCs in the focal plane of the S800. The quantities which are used in this calculation are the dispersive position (x_{fp}), dispersive angle (a_{fp}), non-dispersive position (y_{fp}), and non-dispersive angle (b_{fp}), measured at the focal plane. The x_{fp} and y_{fp} are simply the positions measured in the first CRDC. The angles at the dispersive plane are calculated from the x and y positions of both CRDCs and the fixed gap (1 m) between them:

$$a_{fp} = \tan^{-1}\left(\frac{x_2 - x_1}{1\text{ m}}\right) \tag{3.7}$$

$$b_{fp} = \tan^{-1}\left(\frac{y_2 - y_1}{1\text{ m}}\right) . \tag{3.8}$$

Here, x_1 and y_1 are the position measured in the first CRDC, and x_2 and y_2 are the position measured in the second CRDC. From these quantities, the particle trajectory at the target

area is calculated through an inverse mapping S^{-1}:

$$\begin{pmatrix} a_{ta} \\ y_{ta} \\ b_{ta} \\ d_{ta} \end{pmatrix} = S^{-1} \begin{pmatrix} x_{fp} \\ a_{fp} \\ y_{fp} \\ b_{fp} \end{pmatrix} \tag{3.9}$$

where a_{ta}, y_{ta}, b_{ta}, and d_{ta} are the dispersive angle, non-dispersive position, non-dispersive angle, and deviation from the central energy at the target position, respectively. The inverse map S^{-1} transforms the focal-plane parameters to the target parameters. This map is non-linear and extends to fifth order in the focal-plane parameters. In focused mode, the dispersive position at the focal plane is much smaller than the dispersion due to the momentum spread of the incoming secondary beam; therefore the dispersive position at the target (x_{ta}) cannot be calculated and is instead assumed to be zero.

3.4.1.5 Calibrations

In order to properly use the data from the S800 detectors, these values must be calibrated before the analysis of experimental data. This section details the steps taken to calibrate the S800 detectors.

Although the CRDCs are designed to measure the x and y positions of the beam at the focal plane, the raw signals are a position signal (x) and a time signal (y). Calibration of these signals are necessary to convert the raw signals into the true x and y positions. The calibrations are done by inserting a metal plate in front of each CRDC. The plate has a specific pattern of holes drilled into it whose positions are precisely known. Thus, the each CRDC only detects particles which pass through the holes and into the detector. The pattern

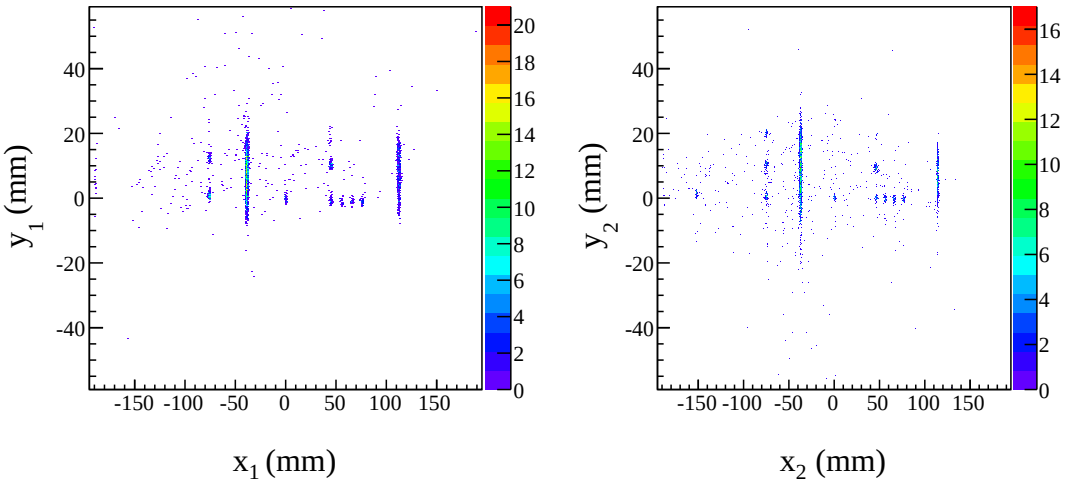

Figure 3.11: An example of the calibrated mask runs for CRDC1 (left) and CRDC2 (right). The holes and lines correspond to holes in a specially made plate in order to map the raw CRDC signals to the known coordinates of the plate holes.

left in the raw CRDC spectrum can be matched to the known pattern, and the measured values at the holes are adjusted through a linear scaling to the true position values. The calibrated positions are designed so that the origin (0,0) corresponds to the central axis of the beam line at the focal plane. The calibration is performed separately for each CRDCs. This process is done several times during an experiment, because the timing signal due to ions drifting in the gas depends on several factors, including the pressure and temperature of the gas. An example of the calibrations is shown in Figure 3.11, which shows the matching hole pattern in both CRDCs.

The timing signals from the A1900 and S800 scintillators are vital in the identification of secondary beam fragments and final particles. The time of flight of a given isotope is not unique, however. If a particle's motion deviates from the central axis of the beam line, then the length of its trajectory through the S800, and therefore time of flight, will be changed. This deviation can be corrected for using the trajectory of the particle measured in the S800 focal plane. This correction is made for the signals of the timing detectors at the A1900

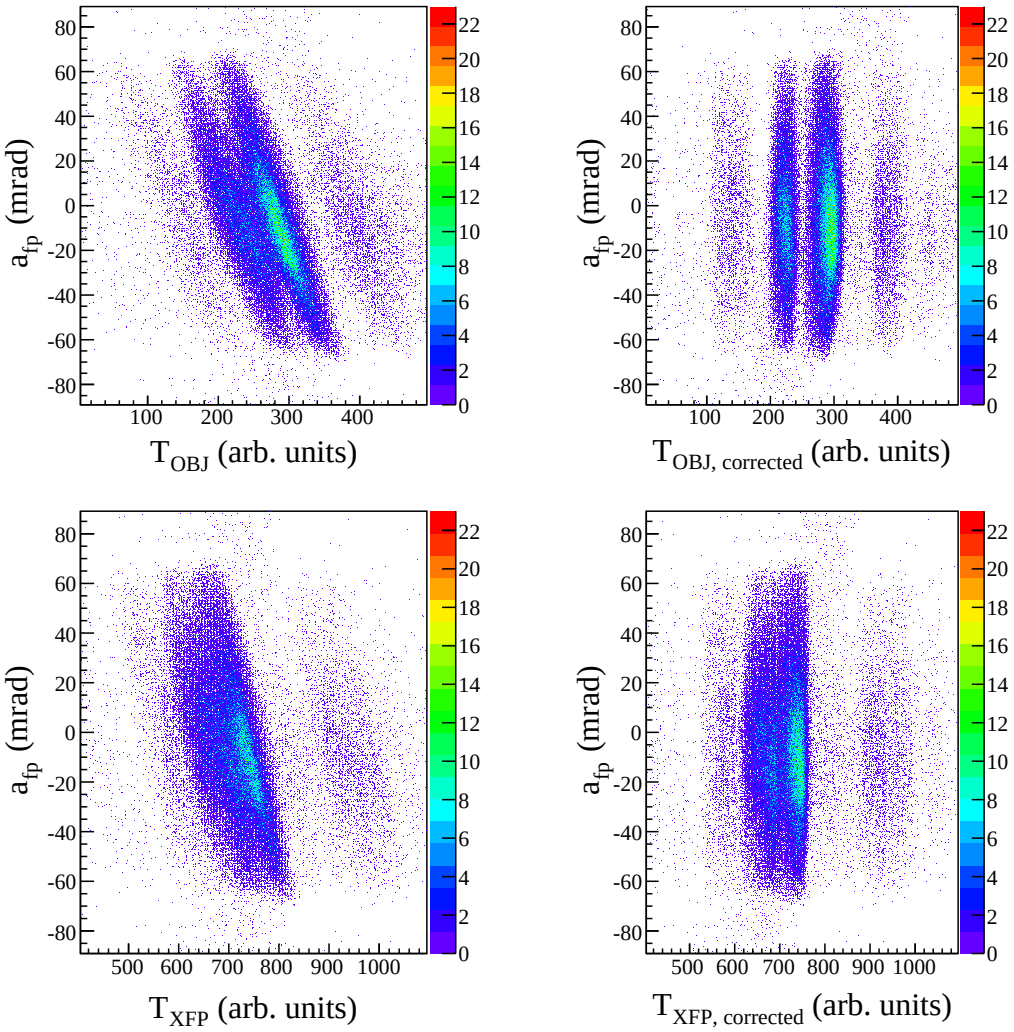

Figure 3.12: Plots showing the effects of corrections to the timing signals from the A1900 extended focal plane (XFP) and S800 object plane (OBJ) scintillators. The left plots show the timing spectra without any corrections, and the right plots show the same spectra with corrections based on the dispersive angle (a_{fp}) measured at the S800 focal plane. The corrections make particle identification possible.

extended focal plane (XFP) and S800 object plane (OBJ). For the object scintillator, for example, the correction is made according to the equation

$$T_{OBJ,\ corrected} = T_{OBJ} + c_a a_{fp} + c_x x_{fp} \tag{3.10}$$

where $T_{OBJ,\ corrected}$ and T_{OBJ} are the corrected and uncorrected timing signals from the S800 object scintillator, a_{fp} and x_{fp} are the dispersive angle and position at the focal plane, and c_a and c_x are correction factors. A similar equation is used to correct T_{XFP}, the time from the A1900 extended focal plane scintillator. The effect of the corrections is shown in Figure 3.12.

3.5 Simulation Software

Most of the analysis of the lifetime is done by comparing gamma-ray data to output from a simulation package. The simulations are based on GEANT4 [69]. GEANT4 incorporates particle tracking through physical materials, and deals with particle and photon interactions. The current package [70] was developed specifically for lifetime measurements at the NSCL. The code has previously been updated to include three foils of the TRIPLEX plunger and includes new geometries for the GRETINA detectors. This section describes details of the simulation package and how it is used in lifetime analysis.

The primary inputs to the simulation are the positions of the plunger foils and the detectors, and the properties of the incoming secondary beam. The simulation can include one, two, or three foils, corresponding to single target, two-foil plunger, or three-foil plunger configurations, respectively. Each foil is assigned a thickness based on the weight of the foil measured before being installed in the plunger. The density of the foils can be scaled to match the energy loss of the secondary beam through each foil measured during the experiment. The foils are positioned based on foil separations used in the experiment, and the entire plunger can be translated relative to other materials to match the experimental conditions. Each GRETINA module, which consists of four segmented germanium crystals,

can be turned on or off in the simulation based on the experimental configuration of the detectors. Each detector is based on a set of four crystal shapes which are rotated and translated to the appropriate position within the simulated volume. The simulation does not include segment information when considering gamma-ray interaction positions. Instead, the position resolution is replicated by shifting the photon interaction position according to a Gaussian distribution. The width of this distribution is fixed as an input to match the observed position resolution.

The simulation also gives a complete description of the radioactive beam. Proton and neutron numbers as well as the charge-state distribution of the secondary beam nucleus are specified. The beam is also given a spatial, angular, and momentum spread to match experimental conditions. The reaction to create the final nucleus in simulated in a single step by instantaneously changing the number of protons and neutrons appropriately. Reaction kinematics are included by parameters which describe the average momentum loss during the reaction and the spread of momentum around this average. The level scheme of the final nucleus is constructed, with the relative population and branching ratios of each state specified.

During every event in the simulation, and single nucleus is created which is sent toward the plunger target. Within the target and degrader foils, the beam is slowed down continuously. The reaction position is randomly chosen somewhere inside the target and degrader foils. The relative number of reactions on each of the foils is fixed by two parameters. As the final nucleus is propagated in the simulation, it emits photons according to the level scheme. The location of gamma-ray emission is determined by sampling an exponential decay function based on the input lifetime. Within the simulation, photons are emitted isotropically in the rest frame of the nucleus, and the distribution is Lorentz-boosted into the laboratory

frame. The Doppler-shifted photons then move through the volume of the simulation and can be absorbed or scattered by any of the surrounding materials. Photon interactions within the detectors are recorded, including the energy loss and position for each scattering or absorption event.

In order to compare with experimental data, the simulation is run many times, with Monte Carlo trials to simulate random processes. Position and energy information for the nuclei along their track is saved at several points, including the reaction location and photon emission points. Photon hit information within the detector, including multiplicity, is also saved. The data is stored as trees within the ROOT framework [71]. Data are output to a ROOT file, and are either saved as raw ROOT trees or histograms. These histograms can be compared to experimental data during analysis.

The analysis of experimental data consists of comparing experimental and simulated gamma-ray spectra. Once all physical and geometrical parameters are fixed in the simulation, several simulations are performed by varying the lifetime of the states of interest. For each lifetime, the simulated histograms are fit using Pearson's χ^2 test [72]. For a histogram with N bins, data points n_i, where i is the index of a bin, and simulated points ν_i, the χ^2 value is calculated as:

$$\chi^2 = \sum_{i=1}^{N} \frac{(n_i - \nu_i)^2}{\sigma_i^2} \tag{3.11}$$

where σ_i is the uncertainty in the counts in bin i of the data. Because the counts in each bin are Poisson-distributed, $\sigma_i^2 = n_i$. This test provides a "goodness-of-fit" for each simulation. If the data are well described by the simulated spectrum, then the χ^2 value will be smaller, because the difference $n_i - \nu i$ is decreased. On the other hand, if the data and simulation are very different, then the χ^2 will increase. Once a the χ^2 value is calculated for several different

lifetimes, a distribution can be found. The lifetime with the minimum of the distribution is then the "best-fit" lifetime. For small changes around the best-fit, the distribution is quadratic, and the lifetime values which are one standard deviation away are given by

$$\chi^2 = \chi^2_{min} + 1 \ . \tag{3.12}$$

In order to validate the simulation and evaluate systematic errors, the simulation software is also used to simulate source efficiency measurements. In this case, no particles are created, but gamma rays are emitted isotropically from a single point, which is defined to match the position of a source used in the experimental calibration. The energies and branching ratios of all gamma rays used in the calibration are set to match known values in the literature. After simulating a large number of gamma rays, the detector response is recorded, and the efficiency of each peak is calculated in the same manner as the experimental data, taking into account the total number of events in the simulation. Examples of the simulated efficiency are shown in Figure 3.8, which compares the simulation to ^{152}Eu and ^{133}Ba source measurements in the energy range below 500 keV. In Figure 3.8 the efficiency is shown for the configuration with only a beryllium target, and the simulation is well matched to the data without any scaling. In Figure 3.8(b), the efficiency is compared for the configuration with a beryllium target and two tantalum degraders. In this case, the simulation overestimates the efficiency, which is due to incorrect description of gamma-ray absorption within the degrader materials. To match the measured efficiency, the simulation must be scaled by an empirical correction factor. In Figure 3.8(b), the simulation is scaled by 0.91, which reproduces the efficiency between 200 keV and 500 keV within 2%, while the efficiency below 150 keV cannot be matched by scaling. However, this configuration was not used in the present experiment,

and the discrepancy is expected to be smaller because only a single degrader was used for the recoil-distance setting. In fact, to calculate knockout cross sections to the excited state in ^{19}C, only the efficiency using the line-shape setting is necessary, where the shape of the simulated efficiency curve is consistent with the data.

Chapter 4

Gamma-ray Lifetime Measurement of ^{19}C

4.1 Motivation

The primary motivation of this experiment was to measure the magnetic dipole ($M1$) response of a halo nucleus to provide new insight into its structure. As discussed in Section 1.3, a well known characteristic of halo nuclei is the large enhancement of the electric dipole ($E1$) response at low energies, also called the soft $E1$ excitation [73]. This soft $E1$ excitation has been well characterized experimentally for several halo nuclei [18, 20, 74, 75]. However, there are no similar measurements of the $M1$ properties of halo nuclei. Some static magnetic properties have been measured for halo nuclei, such as the magnetic moment [76] and magnetization radius [77] of the one-neutron halo ^{11}Be. However, these are static properties only measured for a single state. An $M1$ transition has been observed between the $1/2^+$ and $3/2^+$ states in ^{17}C [51, 78]. This transition, with a lifetime of over 500 ps, is a strongly hindered transition, and this hindrance has been ascribed to the possible presence of a halo structure in the excited $1/2^+$ state [78]. However, the halo nature of this state has not been confirmed experimentally. Thus, there is interest in studying the $M1$ transition rate in a confirmed halo nucleus.

The search for an $M1$ transition between bound states is expected to be difficult. The

greatest obstacle is the small number of transitions available. Because of the low particle separation energy required for halo formation, there are typically very few bound excited states which can decay via gamma emission. In addition, there is a structure effect which tends to block the occurrence of $M1$ transitions. In a simplistic model of the halo, an $s_{1/2}$ neutron is coupled to an inert 0^+ core. One consequence of the selection rules for the $M1$ transition is that it can only occur between the two magnetic substates of a single ℓ orbital, resulting in a spin-flip [79]. For a pure $\ell = 0$ state, the $M1$ response vanishes due to the absence of a spin-flip partner for the $s_{1/2}$ orbital. However, the realistic picture can be more complex; for example, non-negligible core-excitation components have been suggested by an inclusive one-neutron removal study from the halo nucleus ^{19}C [80]. Therefore, a measurement of the magnetic response can probe the purity of the s-wave and core configuration in ^{19}C. The present work aims to quantify the magnetic transition strength in ^{19}C in order to identify possible hindrance, and investigate the role of shell model configurations responsible for such a transition.

The nucleus ^{19}C presents an ideal case to investigate magnetic responses of halo nuclei. The first suggestion of a halo structure in the ground state of ^{19}C came from a measurement of the longitudinal momentum following one-neutron removal [81]. The ground state has been further studied through interaction cross sections [82], momentum distributions [83–85], Coulomb dissociation [18], and knockout reaction cross sections [41, 80, 86]. These results have firmly established the ground-state one-neutron halo structure with spin and parity J^π of $1/2^+$ and one-neutron separation energy S_n of 580(90) keV [87]. The ground-state halo appears because the final neutron in ^{19}C occupies the $1s_{1/2}$ orbital, as shown in Figure 1.3. In addition to ground-state studies, an excited state at $\approx$200 keV has been established by in-beam γ-ray studies [88, 89] which propose a tentative J^π of $3/2^+$. A second possible γ-ray

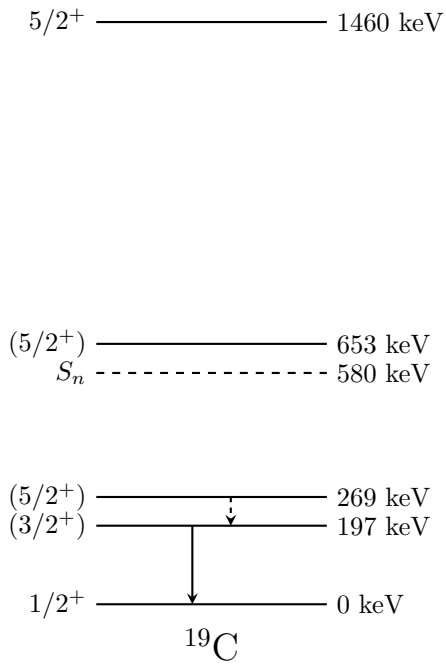

Figure 4.1: The level scheme for ^{19}C at the time of the present experiment. Two gamma-ray transitions have been observed among the bound states [88, 89], and two resonances above the neutron separation energy have been observed [90, 91].

transition at ≈70 keV was also observed in one experiment [89], suggesting a $J^\pi = 5/2^+$ state at ≈270 keV. However, the existence of this state has been called into question because a $5/2^+$ state was observed just above the neutron separation energy [90], and one-neutron knockout cross sections exclude a bound $5/2^+$ state [80, 86]. Based on the proposed level scheme, the multipolarities of both the $3/2^+ \rightarrow 1/2^+_{g.s.}$ and possible $5/2^+ \rightarrow 3/2^+$ transitions are expected to be $M1$. A previous search for isomeric states in ^{19}C did not find any state with a lifetime on the order of 50 ns or longer, indicating a relatively prompt transition [92]. A precise measurement of the lifetime of the bound excited states in ^{19}C can help to deduce the structure of these states.

4.2 Overview of Experiment

The experiment was performed at the National Superconducting Cyclotron Laboratory at Michigan State University to investigate the lifetime of bound excited states in ^{19}C [93]. Stable ^{22}Ne ions were produced by the SuSI ion source and delivered to the Coupled Cyclotron Facility (CCF). In the K500 cyclotron, the $^{22}Ne^{4+}$ ions were accelerated to an energy of 10.9 MeV/nucleon. Once the ions exited the K500, they were sent through a stripper which removed all remaining electrons, and the $^{22}Ne^{10+}$ ions were accelerated by the K1200 cyclotron up to 120 MeV/nucleon. The primary beam was produced at a rate of 150 particle nanoamperes, or about 9×10^{11} particles per second.

The ^{22}Ne beam was impinged on a 5.8 mm beryllium target. A cocktail of reaction products was sent through the A1900 fragment separator, which was tuned to allow ^{20}N fragments to pass through. Although the CCF usually produces nuclei through fragmentation reactions, ^{20}N ions were produced in a different reaction. Fragmentation only involves loss of nucleons, but the current reaction required loss of three protons as well as the pickup of one neutron by the ^{22}Ne nuclei. This reaction setting was chosen because it provided a ^{20}N beam at a suitable energy and rate as well as a high beam purity. A 2.8 mm aluminum wedge degrader was placed in the middle of the A1900 to separate products based on their energy loss. The ^{20}N ions exited the A1900 and arrived at the experimental area at an average energy of 74 MeV/nucleon. The secondary beam arrived at the experimental station at a rate of 1×10^4 ions per second, and a total momentum width of 2% around the average momentum. The purity of the secondary beam at the experimental station was 91%. Identification of the secondary beam was made based on timing measurements at the A1900 extended focal plane and the S800 object plane. The particle identification spectrum for the secondary beam is

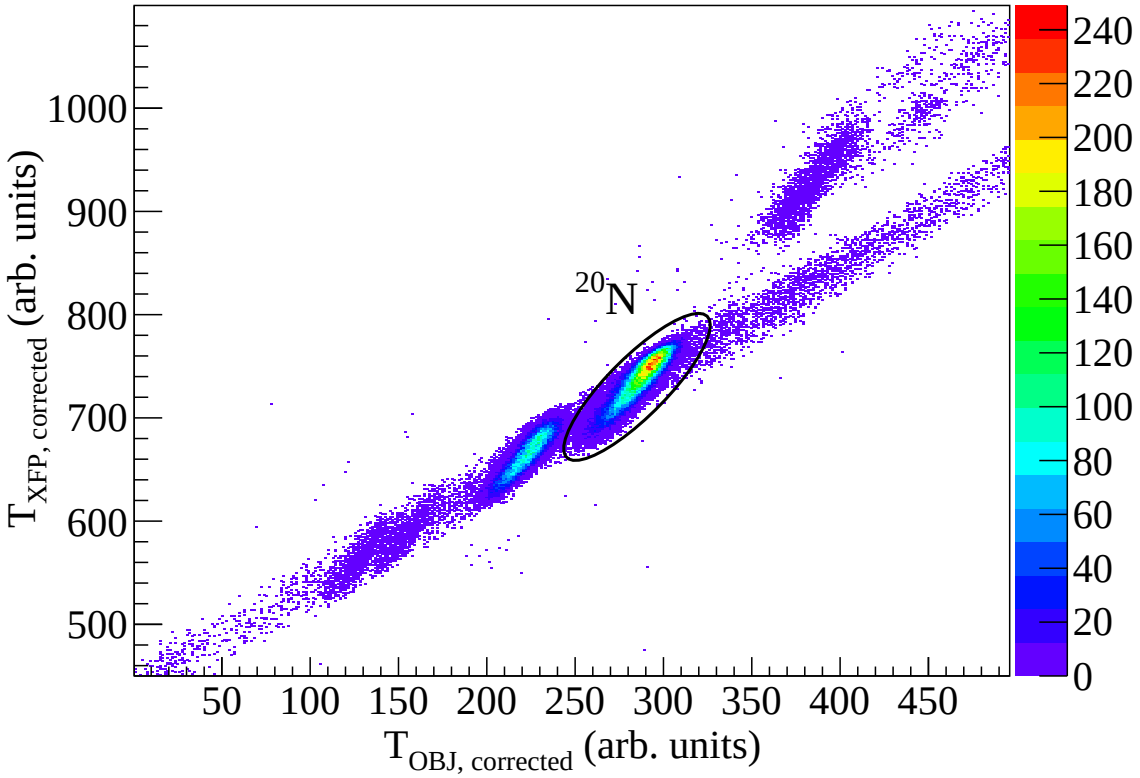

Figure 4.2: The particle identification spectrum for the secondary beam. On the x-axis is the time taken from the S800 object plane scintillator (OBJ), and the y-axis shows the time from the A1900 extended focal plane scintillator (XFP).

shown in Figure 4.2 with ^{20}N identified as the primary component.

The TRIPLEX plunger was located at the target location of the S800. Seven GRETINA modules were placed around the beam line. Four modules were located in a forward ring in centered downstream of the plunger, and the three remaining modules were located in a central ring centered immediately in front of the plunger. The plunger was shifted so that the target was located about 13 cm upstream from the center of the GRETINA sphere. This was done in order to allow for sufficient gamma-ray detection efficiency while maintaining sensitivity to the varying degrees of Doppler shifts due to the different recoil velocities in the Recoil Distance Method (RDM) measurement. With this configuration, the forward detectors covered angles of 25°–55°, and the central detectors covered angles of 50°–80°.

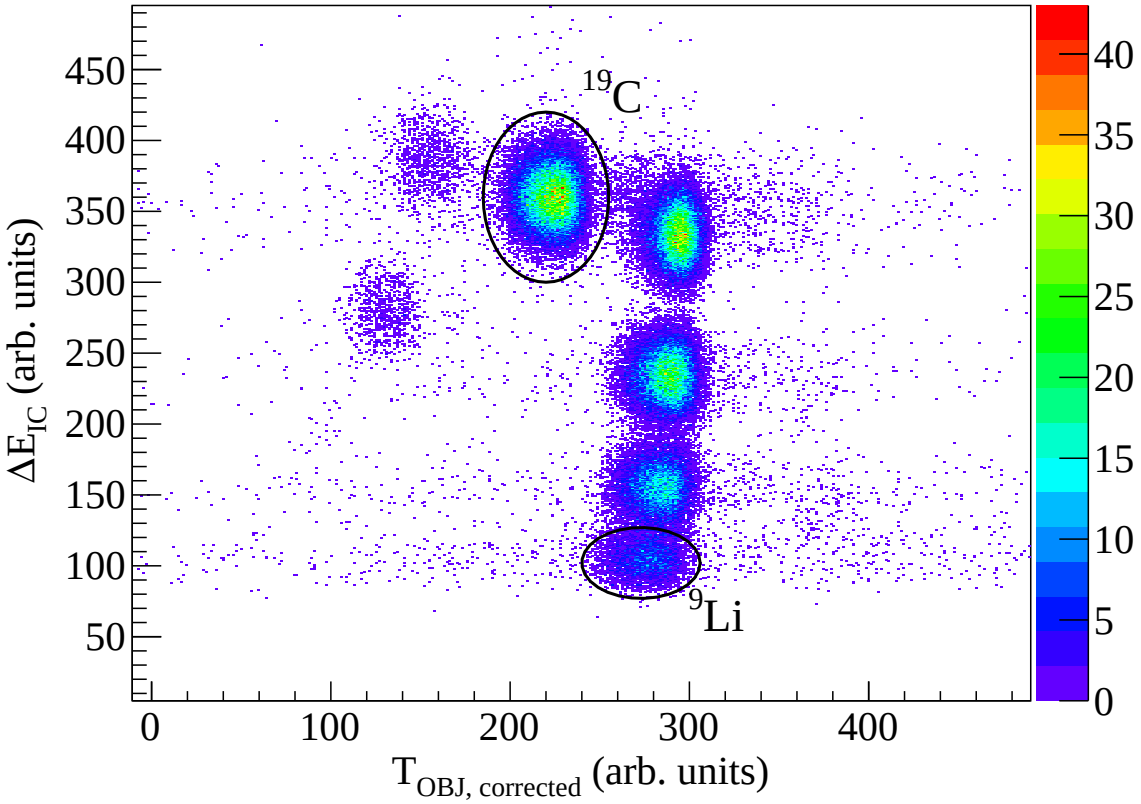

Figure 4.3: The particle identification spectrum for the final products in the S800 spectrograph. The x-axis shows the corrected time of flight from the S800 object plane (OBJ), and the y-axis shows the energy loss through the ion chamber.

Line-shape data were first taken with a single 2.0 mm beryllium target. For the Recoil Distance Method, a 0.92 mm tantalum degrader was added to the plunger, with a target-degrader separation of 5.0 cm. Because of the low rates of the experiment, RDM data were only taken at a single distance setting.

After reacting in the TRIPLEX foils, recoiling ^{19}C nuclei were detected and identified in the S800 spectrograph. The particle identification spectrum obtained during the line-shape portion of the experiment is shown in Figure 4.3. This spectrum was produced by gating on the ^{20}N secondary beam in the A1900 particle identification (Figure 4.2). All events originating from a ^{20}N particle in the A1900 are plotted. Clean separation of final nuclear products is achieved based on the ion chamber energy loss and the S800 focal plane timing.

These two measurements allow unique identification of reaction products. According to Equation 3.5, the ions lose energy based on Z^2, or the square of the charge of the ion. Thus, the vertical axis of serves as an identification of the atomic number of each isotope. The horizontal axis shows the corrected time of flight T_{OBJ} from the S800 object plane. For a given magnetic rigidity of the spectrograph, the time of flight is related to the mass-to-charge ratio of each isotope according to Equation 3.6. Thus, the spectrum in Figure 4.3 is used to identify each product formed from the secondary beam reactions within the TRIPLEX. In Figure 4.3, the location of ^{19}C nuclei is indicated, as well as ^{9}Li. By making software gates on the particle identification spectrum, each nucleus can be studied individually.

4.3 Line-shape Analysis

Data were first taken with the line-shape method. In this case, the TRIPLEX was used with only a 2.0 mm beryllium foil placed at the target position. The target was located 13 cm upstream of the center of GRETINA. The spectrum was created using a detector multiplicity of one, meaning that only those events in which a single GRETINA crystal records a hit are shown. For the current transition energy of 209 keV, the lab frame energies of the gamma rays measured in the detectors are below 300 keV. At these energies, photon interactions in germanium are dominated by photoabsorption (see Figure 2.4); therefore, this cut on multiplicity resulted in little reduction of counts in the gamma-ray peak, while reducing contributions from the background. The energy of every detected gamma ray was corrected according to Equation 2.7. The velocity $\beta = 0.362$ was based on the magnetic rigidity of the S800. The emission angle was calculated from the interaction position within GRETINA, assuming the gamma rays originated from the center of the target. Corrections

to the emission angle and velocity were made based on the parameters calculated from the S800 inverse map (Equation 3.9).

The Doppler-corrected gamma-ray spectrum is shown by the black histogram in Figure 4.4. In the spectrum, a single gamma-ray peak is seen in the spectrum at 209(2) keV. The asymmetric peak has a wide tail extending to low energies. The moderate slope in the spectrum indicates the γ decays occur while ^{19}C recoils are moving along the beam path surrounded by GRETINA. This means the decay lifetime is on the same order as the flight time for the beam to pass through GRETINA. The detector coverage extends about 30 cm downstream of the target position, which corresponds to a flight time of about 3 ns at the average ^{19}C recoil velocity. A transition from a second excited state near 270 keV is not significantly observed in the present data. A gamma-gamma coincidence analysis gated on the 209-keV peak region above 100 keV places an upper limit of 10% on possible feeding.

In order to extract the lifetime of the 209-keV excited state, the data were compared to simulated spectra based on the lifetime of the state. Within the simulation, the spatial and angular distributions of the beam was first matched to the measured distributions of the incoming ^{20}N beam and outgoing ^{19}C beam. Gamma rays in the simulation which interacted with the detectors were analyzed in the same manner as the experimental data, and a Doppler-corrected spectrum was produced. The simulated spectrum does not include a background, so to compare to the experimental spectrum, the simulation must be added to an appropriate background shape. Typically, an exponential shape is used for the background in simulations, which is fit in the regions around gamma-ray peaks [64, 94]. However, in the current spectrum, it is difficult to separate the low-energy tail of the peak from ^{19}C with the background at low energy. Therefore, the background was taken from gamma rays in coincidence with ^{9}Li recoils, which also appear in the particle identification spectrum in

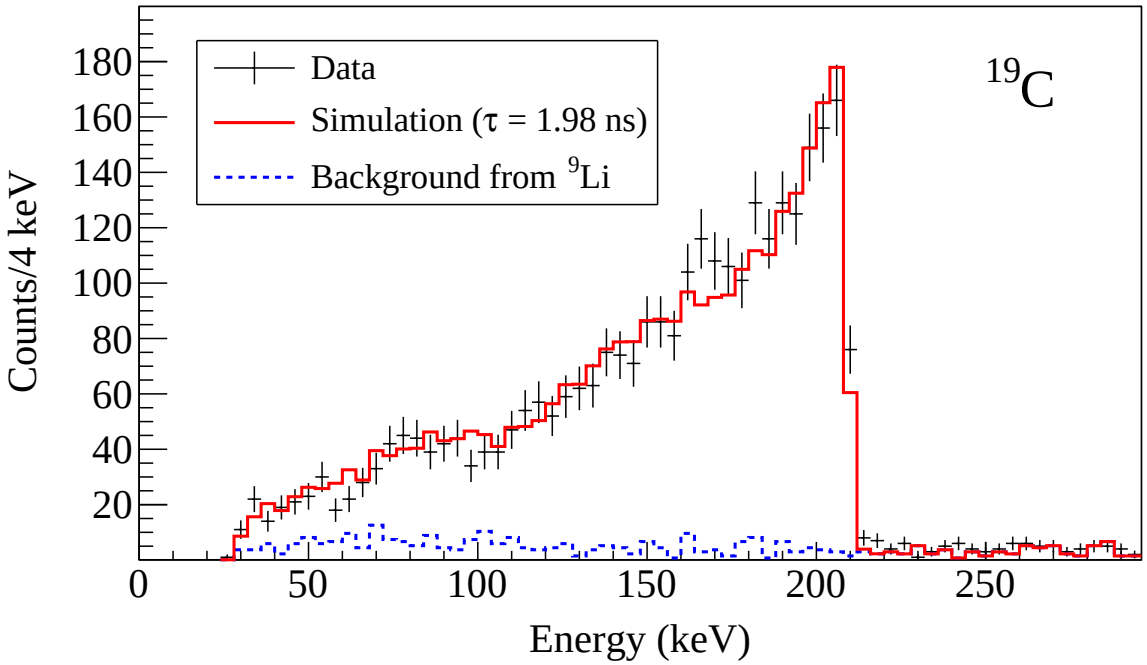

Figure 4.4: The Doppler-corrected spectrum using the line-shape method. A single peak at 209 keV with a wide tail at lower energies is clearly visible. The plot shows the data in black, and the best-fit simulation is shown in red, which includes a background taken from ^{9}Li shown in blue.

the same setting as ^{19}C (see Figure 4.2). The nucleus ^{9}Li was chosen because it has a single gamma-ray transition at 2.7 MeV, so the low-energy region is expected to be dominated by background. The background was scaled to match the region above the peak, and the simulated spectrum was added and scaled to fit the peak region above 100 keV. The simulation was fit for several assumptions of the background shape, it was found that the best fit lifetime did not significantly depend on the choice of background parametrization.

Several spectra were produced in the above manner by adjusting the lifetime of the 209 keV transition, and the best fit lifetime was determined using the χ^2-minimization procedure described in Section 3.5. The χ^2 distribution as a function of the simulated lifetime is shown in Figure 4.6(a). A quadratic fit to distribution around the minimum gives a best-fit lifetime of 1.98 ns. The simulation using this lifetime is shown by the red histogram in

Fig. 4.4. Based on the χ^2 fitting, the statistical uncertainty for this measurement is 0.10 ns.

4.4 Recoil Distance Analysis

After data was taken with only a target, a 0.92-mm tantalum degrader was added in order to make use of the Recoil Distance Method. The target and degrader were separated by 5.0 cm, with the target located 15 cm upstream from the center of GRETINA. The gamma-ray spectrum was created again by gating on the detector crystal multiplicity of one. As was the case for the line-shape analysis, the spectrum was obtained by Doppler correction of the observed gamma rays assuming the decays originated from the center of the target and were emitted with a speed of $\beta = 0.362$. Corrections were also made to the velocity and angle based on S800 measurements. In this case, gamma rays emitted between the target and degrader are emitted at the same velocity as the Doppler correction, and appear in the spectrum at the true decay energy. Nuclei that decay after the degrader have a lower velocity ($\beta = 0.322$) than those which decay before the degrader. This difference in velocity means that the Doppler-corrected energy is below the true decay energy, and these gamma rays appear as a peak at lower energy.

The Doppler-corrected spectrum is shown by the black points in Fig. 4.5. A double-peaked structure is seen with a similar low-energy tail as seen in the line-shape spectrum. The fast and slow peaks are labeled in the figure. The fast peak is centered at 209 keV, while the slow component has a peak at 190 keV. The large height of the slow peak relative to the fast peak indicates that most decays occur beyond the degrader. Thus the lifetime must be longer than the flight time of 500 ps across the 5 cm distance between the target and degrader. Similar to the line-shape measurement, the slow peak has a broad tail extending

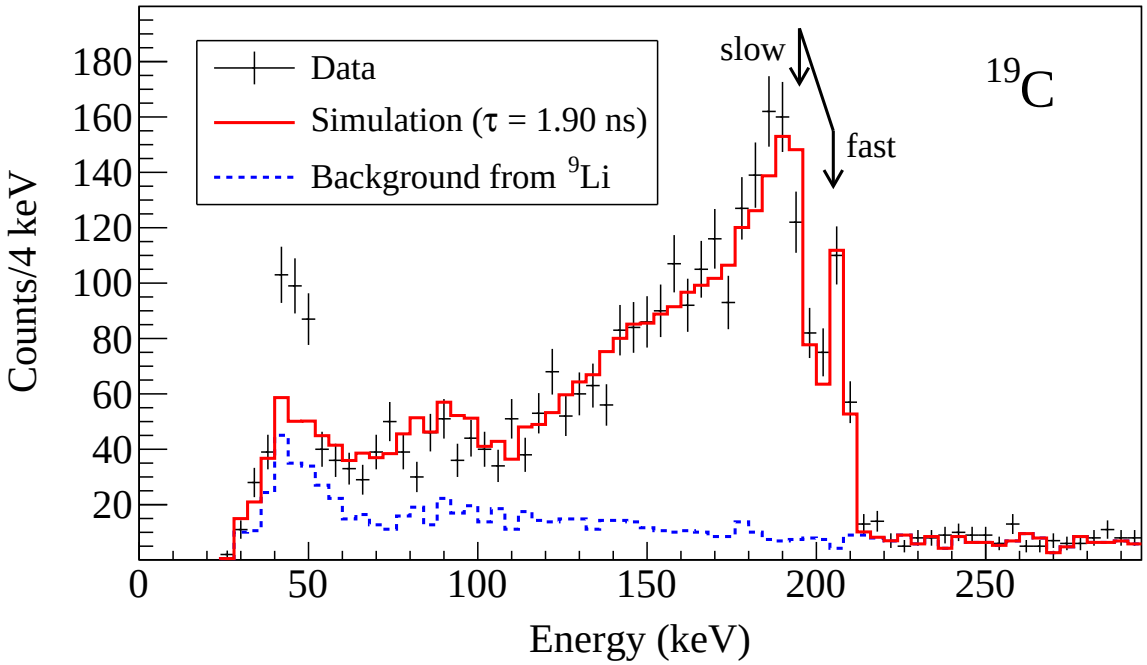

Figure 4.5: The Doppler-corrected spectrum using the Recoil-Distance Doppler-Shift Method. A double peak at 209 keV is again visible, with the same low-energy tail. The fast peak centered at 209 keV is much smaller than the slow peak at 190 keV. The data are shown in black, and the best-fit simulation is shown in red, with the assumed background arising from ^{9}Li shown in blue. In this plot there are additional x-rays around 50 keV because of the energy loss of the beam inside the tantalum degrader.

to low energies. This again is an indication of the nanosecond-order lifetime. In addition to the recoil-distance peak, there is a peak around 50 keV. This is due to X-rays originating from tantalum atoms which are excited as the beam passes through the degrader. These are emitted in the laboratory frame around 70 keV, but appear at lower energies after Doppler correction.

Simulations were performed in the same manner described in Section 4.3, with a background spectrum from ^{9}Li recoils was again used to match the background in the ^{19}C spectrum. The χ^2 distribution generated as a function of lifetime is shown in Figure 4.6(b). The same energy range was used for the fit procedure in both the line-shape and recoil distance measurements, and this region excludes the tantalum X-ray peak below 100 keV. In this

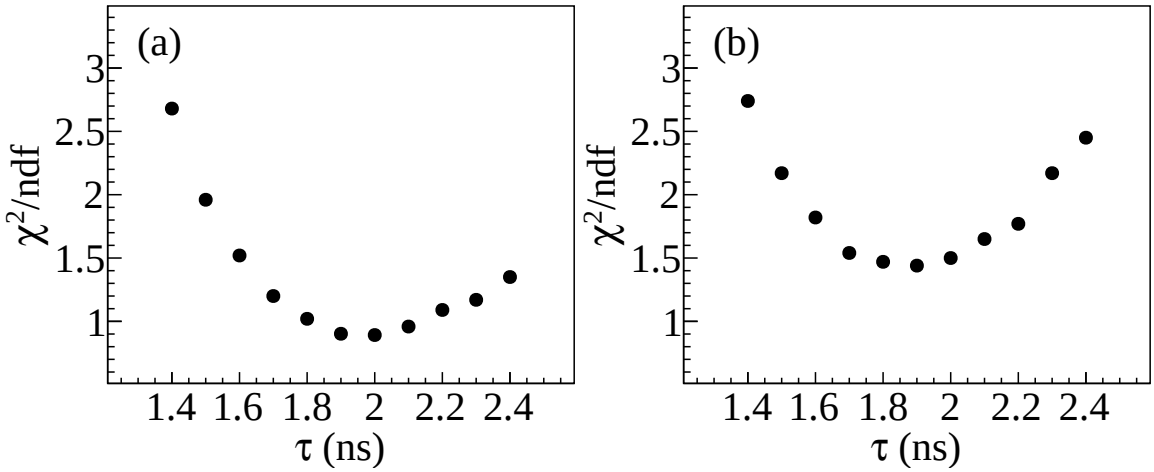

Figure 4.6: The χ^2 distributions obtained by fitting the simulated gamma-ray spectra to the experimental spectrum for various lifetimes of the 209-keV transition in ^{19}C. Part (a) shows the distribution for the line-shape spectrum, and (b) shows the distribution for the recoil-distance spectrum. Quadratic fits to the curves give minima at 1.98 ns and 1.90 ns, respectively.

case, the best-fit lifetime is 1.90 ns, with a statistical error of 0.12 ns. The simulation using a lifetime of 1.90 ns is compared to the data by the red histogram in Fig. 4.5. The lifetime obtained for the recoil-distance measurement is slightly longer than the value obtained with the line-shape technique, although they are both consistent within their uncertainty.

4.5 Results

The adopted value of the lifetime in this work was determined by taking into account systematic errors for each analysis. The errors are summarized in Table 4.1. For both measurements, the largest uncertainty in the lifetime is the statistical uncertainty from the fitting procedure. Sources of systematic uncertainty common to both measurements include the shape of the beam profile used in the simulation, the geometry of the TRIPLEX, and the shape of the gamma-ray background. The largest systematic uncertainty of 0.05 ns (3%) came from the kinematic profile of the beam. The uncertainty in the shape of the background added 0.02 ns

Table 4.1: Summary of systematic errors observed for the lifetime measurement. Error due to the beam properties, plunger geometry, and gamma-ray background shape were similar for both the line-shape and recoil-distance methods. The error from degrader reactions only appears for the recoil-distance measurement.

Component	Error (%)
Difference of measurements	4
Beam properties	3
Plunger geometry	<1
Background determination	1
Degrader reactions	2

(3%), and uncertainty from the positioning of the TRIPLEX plunger contributed less than 0.02 ns (<1%). For the recoil-distance data, an additional ambiguity arises in the spectrum from reactions producing ^{19}C in the degrader, which introduce background contributions in the lifetime measurement. Such reactions only populate the slow peak and increase the apparent lifetime of the transition. To account for secondary reactions in the degrader, a ratio R is introduced in the simulation which defines the ratio of the yield of target/degrader reactions. This allows the simulated spectra to be properly fit to the slow peak. Typically, R is determined simultaneously with the lifetime τ in a two-dimensional χ^2 fitting. For the current setup, however, it was found that there is almost no sensitivity to changes in the reaction ratio. The ratio R assumed in the present simulation is 4.6(14), which is estimated from ratios deduced in previous experiments utilizing analogous one-proton knockout reactions from nitrogen projectiles [95, 96]. The large R in this measurement results in a small additional error of 2%. By adding the statistical and systematic errors in quadrature, the results are deduced to be 1.98(12) ns and 1.90(13) ns for the two measurements.

Because the two results are consistent, the adopted value is determined to be 1.94(15) ns by taking the average. In addition to the errors discussed above, the final value also includes the error due to the difference (4%) between the two results. Based on Equation 1.10, the

$B(M1)$ transition strength is calculated as

$$B(M1) = \frac{56.8}{E_\gamma^3 \tau}\ \mu_N^2 \mathrm{MeV}^3 \mathrm{fs}\ . \tag{4.1}$$

Assuming that the 209-keV transition in ^{19}C is a pure $M1$ transition, the $B(M1; 3/2^+ \rightarrow 1/2^+)$ strength is determined to be $3.21(25)\times10^{-3}\mu_N^2$. Comparing to the Weisskopf estimate for an $M1$ transition (Equation 1.19), this corresponds to a strength of $1.79(14)\times10^{-3}$ Weisskopf units (W.u.). If there is any admixture from the $E2$ multipolarity in this decay, the $B(M1)$ strength is reduced accordingly. However, the effect is expected to be negligible in this case due to the $1/E^{2L+1}$ dependence of the partial lifetimes. In the mass region $A < 44$, the largest $E2$ transition strengths connecting to ground states are about 20 W.u. [97]. With this strength assumed, the $B(M1)$ is reduced by only 6%. In fact, the $E2$ strengths for the $2^+ \rightarrow 0^+$ transitions in neighboring even carbon isotopes are only 1–3 W.u. [95, 96, 98], so the $E2$ contribution in ^{19}C may be safely ignored. A possible spin and parity assignment of $5/2^+$ for the 209-keV state would require a pure $E2$ transition for the decay to the $1/2^+$ ground state. This would result in a $B(E2)$ of 350 W.u., far beyond the recommended upper limit of 100 W.u. [97]. Thus the presently measured lifetime supports the $3/2^+$ assignment previously proposed for the first excited state in ^{19}C.

4.6 Discussion

To investigate the degree of the $M1$ hindrance in ^{19}C, the present result is compared to existing data for $M1$ decay strengths in the mass region $A<40$ in Figure 4.7 [99]. In Figure 4.7(a), the strengths of all transitions which involve a $1/2^+$ state are plotted. As is clear

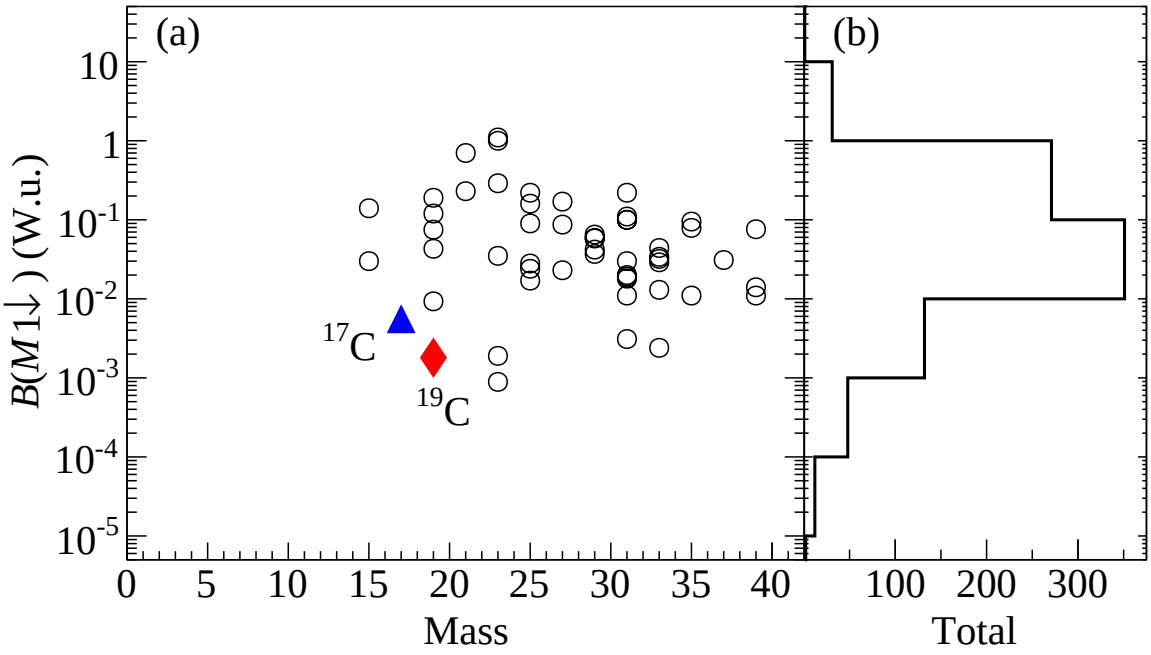

Figure 4.7: A plot showing the distributions of all $B(M1)$ transition strengths among nuclei of mass $A < 40$. (a) plots the values for only those transitions which involve a $1/2^+$ state, with the presently measured $B(M1; 3/2^+ \rightarrow 1/2^+_{g.s.})$ for ^{19}C highlighted in red, and the analogous $B(M1; 1/2^+ \rightarrow 3/2^+_{g.s.})$ in blue. (b) shows the distribution for all $M1$ transitions. In both cases, it is clear that the $B(M1)$ strength for ^{19}C lies among the weakest transitions. Data from Ref. [99]

from the figure, the $M1$ transition in ^{19}C, highlighted in red, is among the smallest strengths observed in this mass region. The strength is even below that measured for the analogous transition in ^{17}C (5.7×10^{-3} W.u.) [51], shown by the blue point. In Figure 4.7(a), two additional points at $A = 23$ are visible, denoting the $1/2^+ \rightarrow 3/2^+_{g.s.}$ transitions in the mirror nuclei ^{23}Na and ^{23}Mg. These are considered to be interband transitions between Nilsson orbits [2 1 1 1/2] and [2 1 1 3/2] of well deformed nuclei [100]. In a shell model picture, the hindrance is due to a large cancellation between the orbital and spin contributions to the $M1$ strength [101]. When compared to all transitions in this mass region as shown in Figure 4.7(b), the $M1$ hindrance in ^{19}C remains evident, indicative of the unusual structure of ^{19}C.

4.6.1 Shell Model Calculations

Shell model calculations were performed to investigate the origin of the $M1$ hindrance as well as the remaining strength. Three interactions, WBP [102], SFO-tls [103], and Yuan [104], were used within the *psd* model space, allowing 2–3 $\hbar\omega$, where $\hbar\omega$ represents the excitation of a single nucleon to the next-highest oscillator shell. The WBP interaction was constructed based on fits to energy levels for nuclei of mass 10–22 [102]. The modified SFO interaction, denoted SFO-tls, is based on the SFO interaction [105], which is a modification of the PSDMK2 interaction [106]. Further modifications to the SFO interaction have been made based on Ref. [103], including adjustments to the tensor (t) and spin-orbit (ls) components of the interaction. These adjustments were made in order to reproduce the observed magnetic properties in ^{17}C [103]. The interaction of Yuan incorporates a monopole-based universal interaction which includes the bare $\pi + \rho$ tensor force [107]. This is designed to reproduce matrix elements involving nucleons within the p and sd shells ($\langle psd|V|psd\rangle$) and cross-shell matrix elements between the p and sd shells ($\langle pp|V|sdsd\rangle$) which have not been well studied in other interactions [104]. Both the SFO-tls and Yuan interactions have further corrections which include so-called loosely bound effects. These corrections take into account the large size of the loosely bound $1s_{1/2}$ orbital by reducing the strength of matrix elements which involve this orbital [103]. The interactions incorporating the loosely bound effects are denoted SFO-tls+lbe and Yuan+lbe. For all five interactions (WBP, SFO-tls, SFO-tls+lbe, Yuan, and Yuan+lbe), the level scheme and $B(M1; 3/2^+ \rightarrow 1/2^+)$ transition probability in ^{19}C are calculated and compared to present data.

The calculated energies for the low-lying states in ^{19}C can be seen in Figure 4.8. The figure also displays the experimental level scheme, including the locations of both the pro-

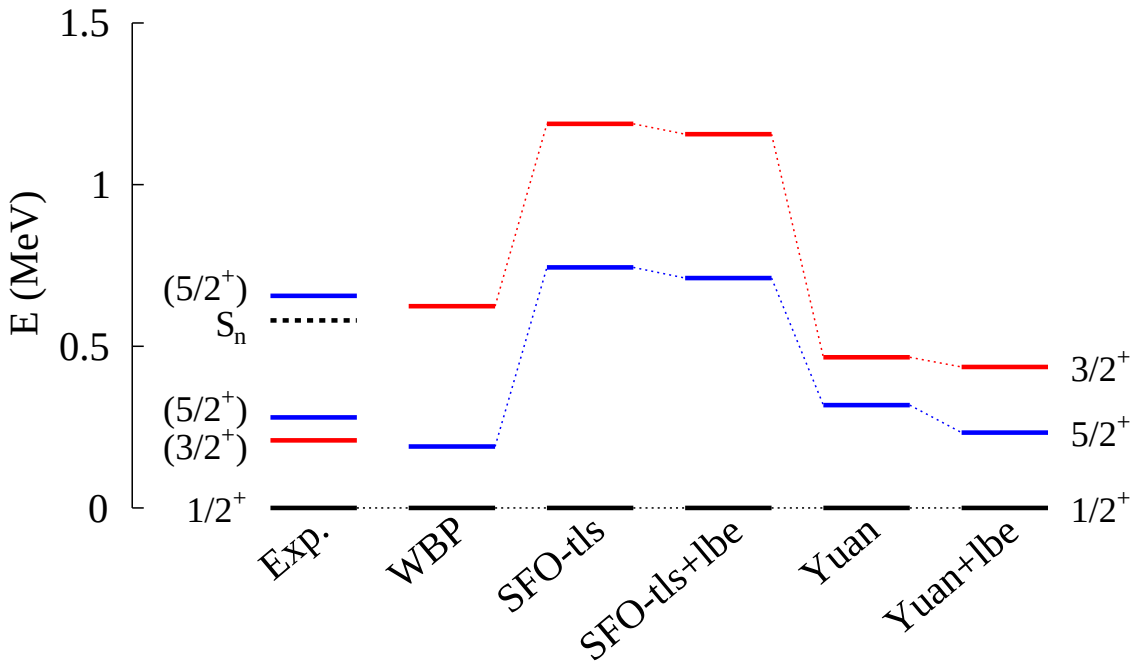

Figure 4.8: The experimental and shell model predictions for the low-lying states in ^{19}C. The 1/2+ ground state is shown in black, the $3/2^+$ is red, and the $5/2^+$ state is blue. The experimentally observed levels shown on the left includes the two suggested locations of the first excited $5/2^+$ state [89, 90]. For all theoretical models, the $1/2^+$ ground state is correctly reproduced, while the order of the $3/2^+$ and $5/2^+$ states are reversed.

posed bound [89] and unbound [90] first $5/2^+$ state. All calculations correctly predict the $1/2^+$ ground state. However, in all cases the $5/2^+$ state is located below the $3/2^+$, in contrast to the proposed level scheme. A test calculation was able to reproduce the level ordering if the single-particle energy of the $1s_{1/2}$ orbital was reduced by 0.5 MeV within the Yuan+lbe interaction. Although the level ordering was consistent with experiment, there was no fundamental change in the components of the wave functions or in the calculated $B(M1)$ transition strength. The purpose of the present work is to determine the microscopic cause of the hindered $B(M1)$ strength. Because this understanding is not affected by the specific ordering of levels, the discrepancy in the level scheme is not important for the current results.

Calculations for the $B(M1; 3/2^+ \rightarrow 1/2^+)$ transition strength for ^{19}C can be seen in

Figure 4.9. Generally, the $M1$ transition strength is calculated between an initial state ψ_i and a final state ψ_f according to

$$B(M1) = \frac{\left|\langle\psi_f||\mathcal{M}(M1)||\psi_i\rangle\right|^2}{2J_i+1} \tag{4.2}$$

where $\mathcal{M}(M1)$ is the $M1$ operator which allows transitions between states for single nucleons, and J_i is the spin of the initial state. The full $M1$ operator is give by [79, 101]

$$\mathcal{M}(M1) = \sqrt{\frac{3}{4\pi}}\sum_{i,\tau_z}\left\{g_{s\tau_z}\vec{s}_{i,\tau_z} + g_{\ell\tau_z}\vec{\ell}_{i,\tau_z} + g_{t\tau_z}\sqrt{8\pi}\left[Y^2(\hat{r}_{i,\tau_z})\otimes\vec{s}_{i,\tau_z}\right]^{(1)}\right\}\mu_N \ . \tag{4.3}$$

The three terms in the summation represent the spin, orbital, and tensor components of the operator. The index i represents the sum over all nucleons, with $\tau_z = \mathrm{p}$ representing protons and $\tau_z = \mathrm{n}$ representing neutrons. The g-factors g_s, g_ℓ, and g_t represent the relative strength the spin, orbital, and tensor terms, respectively. The first two terms represent the standard $M1$ operator described in Equation 1.13, and impose the $M1$ selection rule $\Delta\ell = 0, 1$. The tensor term is a modification which allows a forbidden transition with $\Delta\ell = 2$ through the inclusion of the Y^2 spherical harmonic. The calculations were first performed using the effective g-factors $g_{sp} = 5.307$, $g_{sn} = -3.635$, $g_{\ell p} = 1.15$, $g_{\ell n} = -0.15$, and $g_{tp}, g_{tn} = 0$. These values were previously used to explain magnetic properties in ^{17}C [103]. The results are shown by the solid light grey bars in Figure 4.9.

In all cases, the calculations under-predict the observed value, by up to two orders of magnitude. Several corrections are required to match the experimental value. The addition of loosely bound effects to the SFO-tls and Yuan interactions is shown by the solid dark grey bars. In both cases, this addition improves the predicted values, but is still insufficient to

account for the observed value. A further correction is needed to match to the experiment, and this occurs through the modification of the effective g-factors in the $M1$ operator. The modified values are $g_{sp} = 5$, $g_{sn} = -3.5$, $g_{\ell p} = 1.175$, $g_{\ell n} = -0.106$, $g_{tp} = 0.26$, and $g_{tn} = -0.17$. These are based on a fit to $M1$ data using six parameters with the USDA interaction [101]. The non-zero g_t terms activate the tensor term in the $M1$ operator, which is a coupling of the position and spin vectors of the nucleons. The presence of the $Y^2(\vec{r})$ term allows the $\Delta\ell = 2$ transition, which is otherwise forbidden by selection rules. In the case of ^{19}C, this allows a transition between the $s_{1/2}$ and $d_{3/2}$ orbitals for the valence neutron. The inclusion of the modified $M1$ operator is shown by the hatched bars in Figure 4.9. In all cases, this provides further improvement to the predicted values.

Based on the shell-model calculations, the observed $M1$ hindrance is ascribed to the lowering of the $1s_{1/2}$ orbital and resulting proximity to the $0d_{5/2}$ orbital characteristic of weakly bound nuclei. The degeneracy of these two orbitals is supported by all the calculations, as demonstrated by the compressed level schemes shown in Figure 4.8. The primary configurations of the valence neutrons in the ground and first excited states in ^{19}C are similar for all calculations, and are given as follows:

$$|^{19}\mathrm{C}(1/2^+)\rangle = \alpha|(d_{5/2})^4_{J=0^+}\otimes(s_{1/2})\rangle + \dots \tag{4.4}$$

$$\begin{aligned}|^{19}\mathrm{C}(3/2^+)\rangle &= \beta|(d_{5/2})^4_{J=2^+}\otimes(s_{1/2})\rangle \\ &\quad + \gamma|(d_{5/2})^3_{J=3/2^+}\otimes(s_{1/2})^2\rangle + \dots \ .\end{aligned} \tag{4.5}$$

The configurations listed here are built on top of a ^{14}C core, with a 0^+ configuration shown by Figure 1.3(b). These configurations are shown schematically in Figure 4.10. For the WBP

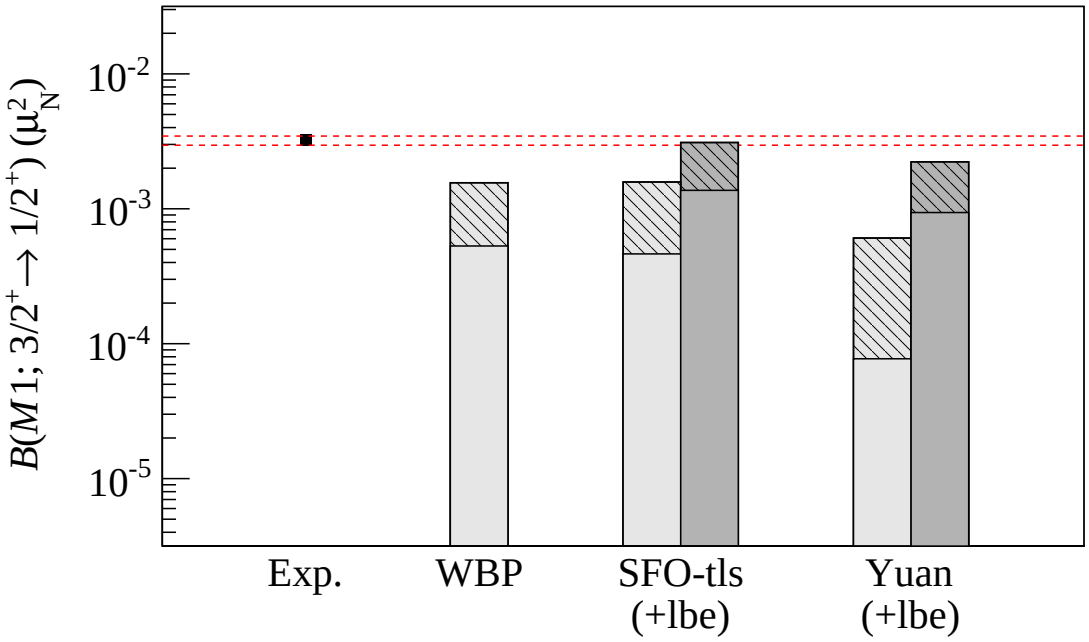

Figure 4.9: The experimental and shell model predictions for the $B(M1; 3/2^+ \rightarrow 1/2^+)$ transition strength in ^{19}C. The current experimental value is shown on the left, and the results for each shell model calculation are shown on the right. The light grey bars indicate the values calculated without any corrections. The dark grey bars for the SFO-tls and Yuan interactions indicate calculations with the loosely-bound effects [103]. The striped bars additionally include the modification of the $M1$ operator as described in the text. In all cases, both the loosely bound effects and modified $M1$ operator improve the predictions relative to the observed value.

and Yuan(+lbe) interactions, the relative strengths of the configurations are nearly identical, with $\alpha^2 \approx 0.48$, $\beta^2 \approx 0.29$, and $\gamma^2 \approx 0.26$, while the SFO-tls(+lbe) gives $\alpha^2 \approx 0.40$, $\beta^2 \approx 0.26$, and $\gamma^2 \approx 0.23$. The agreement between these calculations clearly shows the prevalence of the $1s_{1/2}$ and $0d_{5/2}$ components in both the ground and excited states.

For five valence neutrons within the $(s_{1/2}d_{5/2})^5$ space above a ^{14}C(0^+) core, the only possible configurations for the $1/2^+$ and $3/2^+$ states are those listed in Equations 4.4 and 4.5. The $M1$ transition strength between these configurations is exactly zero. More generally, all possible configurations for the $(s_{1/2}d_{5/2})^5$ space are (a) $(d_{5/2})^5$ $J = 5/2^+$; (b) $(d_{5/2})^4_{J=0^+} \otimes (s_{1/2})$ $J = 1/2^+$; (c) $(d_{5/2})^4_{J=2^+} \otimes (s_{1/2})$ $J = 3/2^+, 5/2^+$; (d) $(d_{5/2})^4_{J=4^+} \otimes (s_{1/2})$ $J = 7/2^+$,

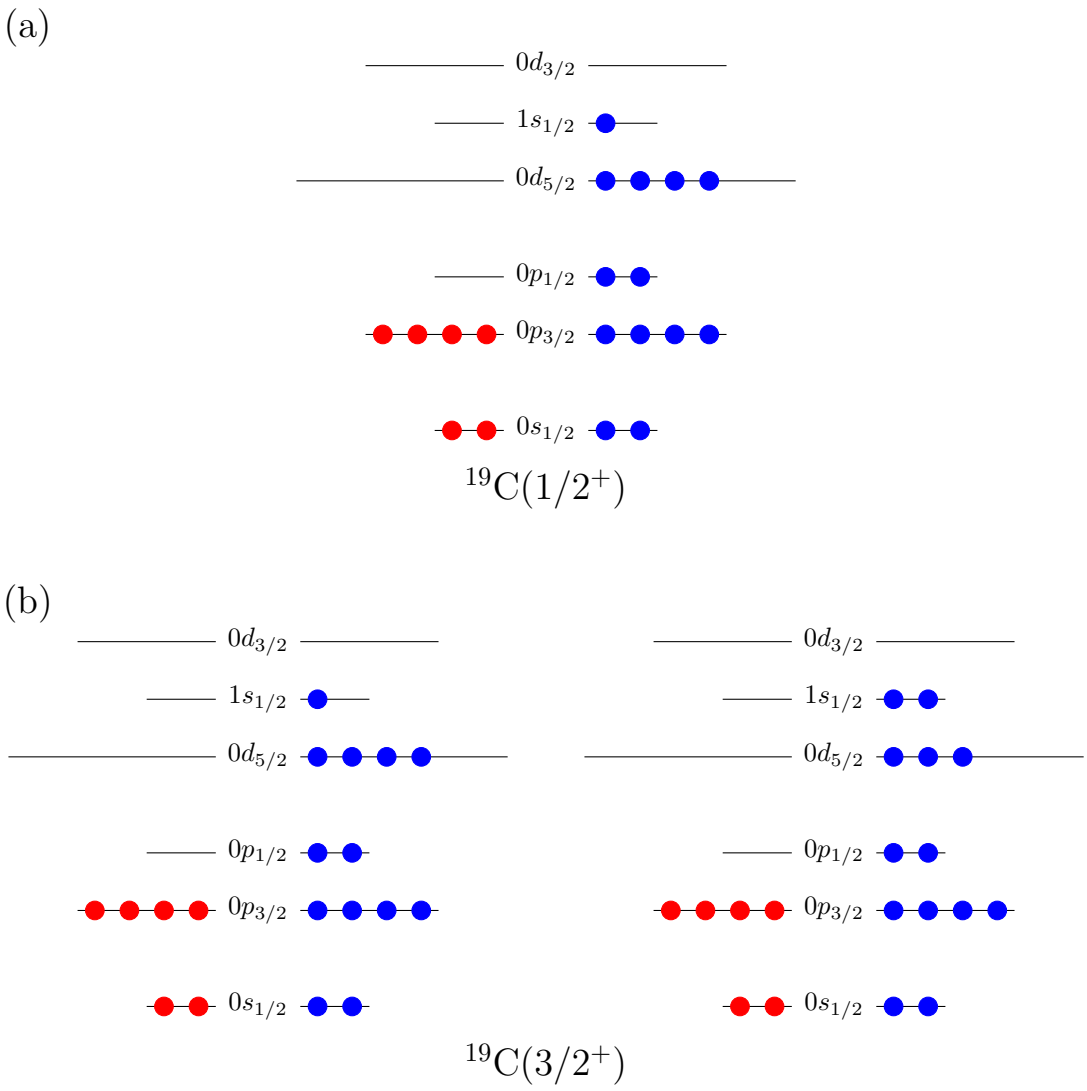

Figure 4.10: The primary configurations for the ground state (a) and excited state (b) in ^{19}C. The $1/2^+$ ground state is primarily formed by the $1s_{1/2}$ neutron coupled to a 0^+ core. The $3/2^+$ excited state is divided between two main configurations. On the left, the $1s_{1/2}$ neutron is coupled to a 2^+ core, and on the right, two neutrons in the $1s_{1/2}$ orbital couple to 0^+, and the three neutrons in the $0d_{5/2}$ orbital couple to $3/2^+$. The calculated amplitudes of each configuration are given in the text.

$9/2^+$; and (e) $(d_{5/2})^3 \otimes (s_{1/2})^2$ $J = 3/2^+, 5/2^+, 9/2^+$. The $B(M1)$ strength is zero between all pairs of these configurations except for the spin-flip transitions between the $3/2^+$ and $5/2^+$ states in (c), and the $7/2^+$ and $9/2^+$ states in (d). It is also important to note that the $M1$ strength between the $3/2^+$ and $5/2^+$ states in (e) is also zero because these are within

the identical $(d_{5/2})^3$ space, and this transition is not a spin-flip. Other transitions require a $\Delta\ell = 2$, $\Delta j = 2$ transition between the $1s_{1/2}$ and $0d_{5/2}$ orbitals. This is the primary mechanism responsible for the suppressed $B(M1)$ value in ^{19}C. Additional components to the wave functions beyond those listed in Equations 4.4 and 4.5 could allow finite transition strengths, but the total $B(M1)$ remains diminished due to the smaller amplitudes of those configurations.

A decomposition of the $M1$ strength into the individual matrix elements for the proton and neutron orbital, spin, and tensor components using the WBP interaction is shown in Figure 4.11. The figure also shows similar calculations for the $1/2^+ \rightarrow 3/2^+$ transitions in ^{23}Na and ^{23}Mg, which also have small $B(M1)$ values on the same order as ^{19}C. For ^{23}Na and ^{23}Mg, there is a large cancellation between individual components which results in the small values for the transition strengths. For ^{19}C however, there is not as strong of a cancellation effect, but instead the individual matrix elements themselves are much smaller. What is unique for ^{19}C is that the orbital and spin components are as small as the tensor components. Thus, the prominence of the $s_{1/2}$ and $d_{5/2}$ orbitals in both the ground and excited states reduces the $M1$ strength down to the level of 10^{-3} μ_N^2, where contributions from the ℓ-forbidden transition between the $s_{1/2}$ and $d_{3/2}$ orbitals become important.

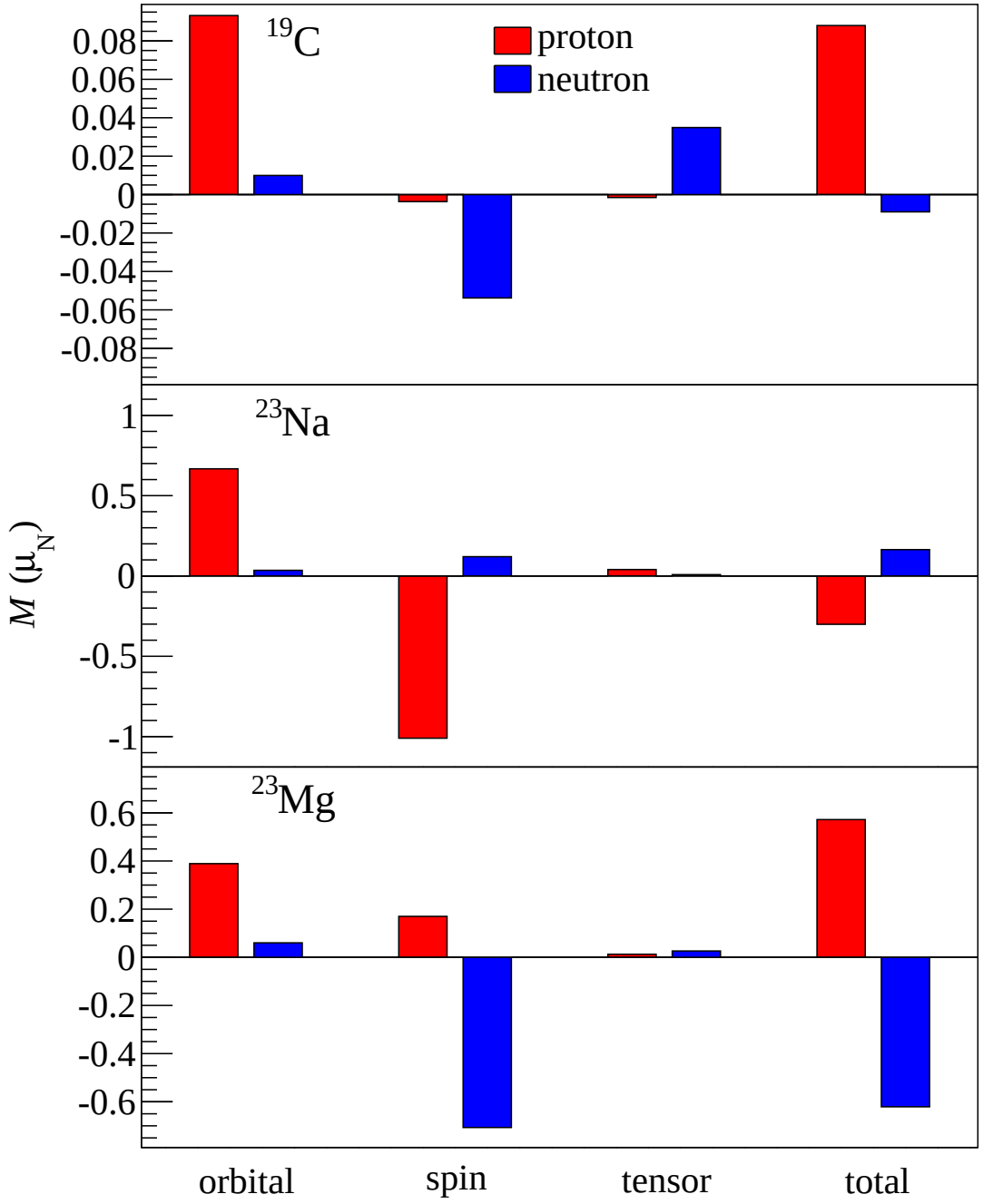

Figure 4.11: Decomposition of the calculated $B(M1)$ strengths in ^{19}C, ^{23}Na, and ^{23}Mg into the spin, orbital, and tensor components for both protons and neutrons. All calculations are made using the WBP interaction [102]. It is clear that the individual matrix elements are smaller for ^{19}C, while the small $B(M1)$ values in ^{23}Na and ^{23}Mg are due to cancellation between the components.

Chapter 5

One-proton Knockout Measurement of ^{20}N

5.1 Motivation and Overview

Results from the present experiment were also analyzed to study the one-proton knockout reaction from ^{20}N. This study can be considered as an extension of the lifetime measurement because it is used to examine the spins of the excited state in ^{19}C. The reaction is also sensitive to the ground wave function in ^{20}N. Measurement of the exclusive cross sections to states in ^{19}C gives the overlap of those states with the ^{20}N ground state and can be used to constrain the ground state spin in ^{20}N. Additionally, measurement of the momentum distribution of the ^{19}C fragments after the reaction can be used to confirm the configuration of the valence proton in ^{20}N.

In a standard shell model picture for ^{20}N, the seventh proton occupies a $p_{1/2}$ orbital, and the thirteenth neutron occupies a $0d_{5/2}$ orbital. Coupling of these two orbitals is expected to produce a 2^- or 3^- for the ground state. However, as shown in Figure 1.3, the standard picture does not explain the ground state in the neighboring nucleus ^{19}C. If the situation is the same for ^{20}N, then another ground state may be possible. Calculations with the WBP interaction [102] predict a 2^- ground state. However, there is very little experimental data on the levels in ^{20}N. A beta-decay study of ^{20}N has found decay rates consistent with a 2^-

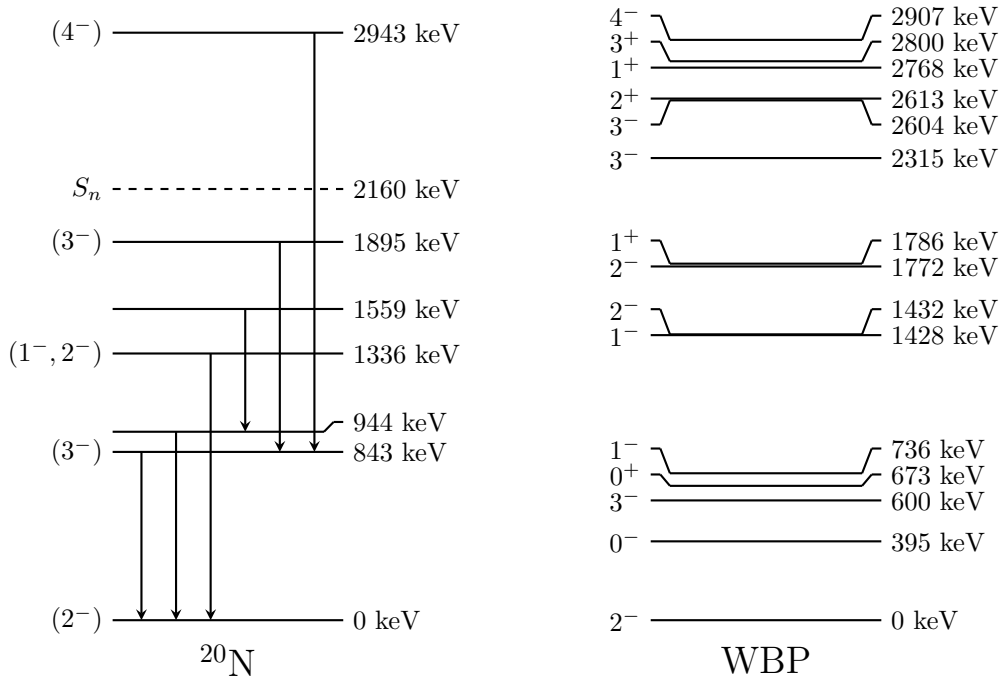

Figure 5.1: Comparison of the low-lying levels observed in ^{20}N with shell-model calculations using the WBP interaction. The spin and parities of the experimental levels are based on similar shell model calculations [110], and no firm assignments have been made for any states.

ground state [109]. A more recent gamma-ray study observed several transitions in ^{20}N and made tentative level assignments based on shell model calculations, but did not make any firm spin assignments [110]. The level scheme for ^{20}N resulting from that experiment is shown in Figure 5.1, which also compares the levels obtained with the WBP interaction. Because very few states are assigned from the experiment, it is clear more evidence is necessary to characterize the spin in the ground state of ^{20}N.

There is great interest in identifying the levels in ^{20}N, because such identification can help to locate the single-particle energies of the neutron $1s_{1/2}$ and $0d_{5/2}$ orbitals. It is known that these two orbitals move rapidly among neutron-rich nuclei. In ^{22}O, the lowering of the $0d_{5/2}$ orbital below the $1s_{1/2}$ orbital causes the appearance of the $N = 14$ magic number [111], while the gap is expected to disappear in the nearby nucleus ^{21}C [112]. The relative energies

of the $1s_{1/2}$ and $0d_{5/2}$ orbitals for several isotonic chains are shown in Figure 5.2 [113–115]. For the $N = 7$ and $N = 9$ chains, the orbitals are nearly degenerate in ^{14}N and ^{16}N, and in ^{13}C and ^{15}C, the levels are inverted, with the $1s_{1/2}$ orbital at a lower energy than $0d_{5/2}$. In the case of $N = 11$, the levels are inverted for ^{17}C, but return to normal ordering in ^{18}N, with the $1s_{1/2}$ above the $0d_{5/2}$. In the present case of $N = 13$, the two orbitals are degenerate in ^{19}C [93], as shown by the simultaneous filling of these orbitals in Figure 1.3(d). If the normal ordering returns in ^{20}N, then the five valence neutrons should occupy the $0d_{5/2}$ orbital. Coupling of these $0d_{5/2}$ neutrons to the $0p_{1/2}$ valence proton creates a 2^- or 3^- ground state in ^{20}N, and determination of the ground state would help to confirm the expected trend for $N = 13$. Although the current experiment can provide evidence for the ground state in ^{20}N, proper assignment of all low-lying states is necessary to fully determine the locations of the $1s_{1/2}$ and $0d_{5/2}$ single-particle states, which is beyond the scope of the current measurement.

The knockout reaction is also interesting in view of the possible similarity of the neutron distributions in ^{20}N and ^{19}C. Previous measurements of the interaction and charge-changing cross sections in ^{20}N have suggested the presence of a neutron skin [116, 117]. A neutron skin is described as an excess of neutrons around the nuclear surface, although without the extended tail that is present for halos. The current measurement is the first study of a one-proton knockout reaction leading to a halo nucleus, and could be useful to investigate the connection between skins and halos.

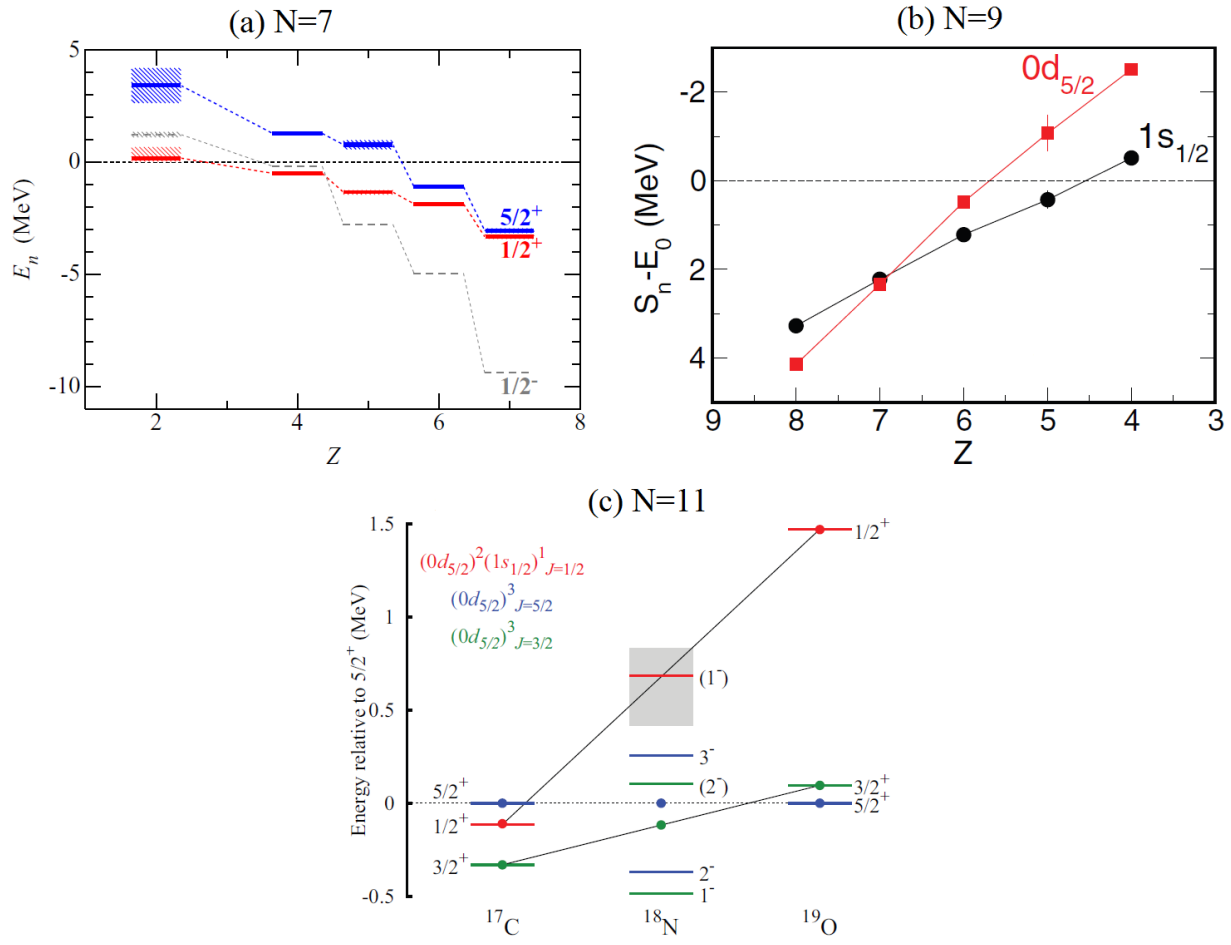

Figure 5.2: Three plots which show the evolution of the neutron $s_{1/2}$ and $d_{5/2}$ orbitals in light neutron-rich isotopes. In (a), the energies of the orbitals are plotted relative to the neutron separation energy for $N = 7$ isotones. For ^{13}C ($Z = 6$), the $1s_{1/2}$ orbital (red) is clearly located below the $0d_{5/2}$ orbital (blue), and for ^{14}N, the orbitals are nearly degenerate. Plot (b) shows the same trend for the $N = 9$ isotones. Here, for ^{15}C, the $1s_{1/2}$ orbital (red) is below the $0d_{5/2}$ orbital (black), while they overlap in ^{16}N. Plot (c) shows the energy of the $1s_{1/2}$ orbital (red) relative to the $0d_{5/2}$ orbital (blue) for the $N = 11$ isotones. In this case, the orbitals are nearly degenerate in ^{17}C, while in ^{18}N, the $1s_{1/2}$ orbital is located well above the $0d_{5/2}$ orbital. Figures from Refs. [113–115].

5.2 Cross Sections

The experiment was performed as described in Section 4.2. The cross section was calculated from the line-shape setup which employs only a 2 mm beryllium target with no degrader. The inclusive cross section σ_{-1p} for the one-proton knockout from ^{20}N to ^{19}C is calculated as

$$\sigma_{-1p} = \frac{N_{^{19}\mathrm{C}} A_t}{\epsilon N_{^{20}\mathrm{N}} \rho_t d_t N_A} \tag{5.1}$$

where $N_{^{19}\mathrm{C}}$ is the total number of ^{19}C nuclei detected, $N_{^{20}\mathrm{N}}$ is the number of ^{20}N nuclei incident on the reaction target, A_t, ρ_t and dt are the target molar mass, mass density, and thickness, respectively, $N_A = 6.02 \times 10^{23}$ mol^{-1} is Avogadro's number, and ϵ is the efficiency to detect the ^{19}C nuclei. The number of ^{19}C nuclei was obtained by integrating the particle ID spectrum (see Figure 4.3). The incoming beam rate was given by the rate of the S800 object scintillator. Transmission of the secondary beam from the object scintillator to the experimental area was determined by measuring the secondary beam rate through S800 without a target installed. Because the 2% total momentum spread of the secondary beam is smaller than the 5% momentum acceptance of the S800 spectrograph, all of the beam incident at the target location is detected at the focal plane, so that the transmission measured at the focal plane is identical to the transmission at the target. The total one-proton knockout cross section σ_{-1p} measured for the current experiment is 0.76(10) mb.

Cross sections to excited states are obtained independently from the inclusive cross section by considering gamma-ray yields in GRETINA. In the present experiment, only a single gamma-ray transition was observed at 209 keV. The measured lifetime supports the $3/2^+$ assignment for this state. No evidence for a bound $5/2^+$ state was found. The total yields were counted from the gamma-ray spectrum in Figure 4.4. All counts in the peak, even down

Table 5.1: Theoretical cross sections compared to the experimental values, assuming a 2^- ground state in ^{20}N. Theoretical cross sections are calculated as described in the text. The total cross section is first calculated assuming the observed $3/2^+$ state is the only bound excited state in ^{19}C. The second calculation also includes the cross section assuming the low-lying $5/2^+$ state is bound, calculated with the excitation energy from the previous gamma-ray study [89].

E_x (keV)	J^π	ℓ, j	$\sigma_{\rm sp}$ (mb)	C^2S	$\sigma_{\rm th}$ (mb)	$\sigma_{\rm exp}$ (mb)
0	$1/2^+$	1, 3/2	13.1	0.038	0.52	
209	$3/2^+$	1, 1/2	12.0	0.014		
		1, 3/2	13.0	0.086	1.36	
269	$5/2^+$	1, 1/2	11.9	0.81		
		1, 3/2	12.9	0.068	11.1	
Inclusive $(1/2^+, 3/2^+)$					1.88	0.76(10)
Inclusive $(1/2^+, 3/2^+, 5/2^+)$					13.0	

to the low-energy region below 100 keV, were assumed to come from either the $3/2^+ \rightarrow 1/2^+$ transition or from the background. The gamma-ray yields were then scaled based on the efficiency of gamma-ray detection. Using this method, the calculated cross section to the 209-keV state $\sigma_{-1p}(209\ \text{keV})$ is 0.62(9) mb. In general, the cross section to the ground state $\sigma_{-1p}(g.s.)$ is simply calculated as the difference between the inclusive cross section and the cross section to all excited states:

$$\sigma_{-1p}(g.s.) = \sigma_{-1p} - \sum_{E_x} \sigma_{-1p}(E_x) \ . \tag{5.2}$$

With only one observed excited state, the cross section to the ground state in ^{19}C is found to be $\sigma_{-1p}(g.s.) = 0.14(13)$ mb.

5.2.1 Theoretical Calculations

Calculation of theoretical cross sections comprises two parts: spectroscopic factors $C^2S(J^\pi, n\ell j)$ for removal of a proton with quantum numbers $n\ell j$ leading to a final state with spin J^π, and single particle cross sections $\sigma_{sp}(n\ell j, S_p^{eff})$ based on an effective proton separation energy S_p^{eff}. Spectroscopic factors were obtained from shell-model calculations with the WBP interaction [102]. States in ^{19}C and ^{20}N were calculated within the *psd* model space allowing 2–3 $\hbar\omega$ for ^{19}C and 1–2 $\hbar\omega$ for ^{20}N. Spectroscopic factors were calculated for each proton orbital which connects the ground state in ^{20}N with the low-lying states in ^{19}C. The calculated spin and parity of the ground state in ^{20}N is 2^- (see Figure 5.1). However, because the ground state is not experimentally well determined, the 0^- state at 395 keV was also considered as a ground-state candidate. Therefore, two sets of calculations were made for both possible ground states.

Single-particle cross sections were calculated from elastic S-matrices for the target-core and target-proton systems. The S-matrices were calculated by folding the target and core/proton densities with the effective nucleon-nucleon interactions. Densities for the ^{9}Be target and ^{19}C core were calculated in the Woods Saxon form:

$$\rho(r) = \frac{\rho_0}{1 + \exp[(r-c)/a]} \ . \tag{5.3}$$

The parameters were obtained from Ref. [118]:

$$a = 0.54 \tag{5.4}$$

$$c = (0.978 + 0.0206A^{1/3})A^{1/3} \tag{5.5}$$

$$\rho_0 = \frac{3A}{4\pi c^3(1 + \pi^2 a^2/c^2)} \ . \tag{5.6}$$

The proton was treated as a point particle. The effective nucleon-nucleon was taken to be a zero-range delta function whose strength was based on nucleon-nucleus scattering at high energy [119]. The proton potential within the ^{19}C core was a Woods-Saxon form, with typical parameters $r_0 = 1.25$ fm and $a = 0.7$ fm. The potential depth was adjusted to match the proton separation energy of 17.9 MeV. For the cross section to the excited state in ^{19}C, the effective separation energy S_p^{eff} is calculated as the sum of the ground-state separation energy and the excitation energy of 209 keV.

The results of the cross section calculations are shown for a 2^- ground state in Table 5.1, and for a 0^- ground state in Table 5.2. The tables list the spectroscopic factors and single-particle cross sections for the $1/2^+$ ground state and $3/2^+$ excited state in ^{19}C. The theoretical cross section for each state is the product of these factors scaled by a correction factor of $[A/(A-1)]^N = [20/19]^1$ which is necessary to correct for the center-of-mass motion for spectroscopic factors calculated in the harmonic oscillator basis [55]. For the 2^- case, it is possible to remove an $\ell = 1$ proton and produce $1/2^+$, $3/2^+$, and $5/2^+$ states in ^{19}C. Therefore, the inclusive cross section was calculated first for ground state and observed $3/2^+$ excited state, and additionally including a $5/2^+$ state. The effective separation energy of this state was based on the excitation energy (269 keV) from the gamma-ray study which first suggested a bound $5/2^+$ state [89]. Because the excitation energies are much smaller

Table 5.2: Theoretical cross sections compared to the experimental values, assuming a 0^- ground state in ^{20}N. In this case, the $5/2^+$ state is not accessible through removal of an $\ell = 1$ proton.

E_x (keV)	J^π	ℓ, j	σ_{sp} (mb)	C^2S	σ_{th} (mb)	σ_{exp} (mb)
0	$1/2^+$	1, 1/2	12.1	0.85	10.8	
209	$3/2^+$	1, 3/2	13.0	0.059	0.81	
Inclusive					11.6	0.76(10)

than the proton separation energy, the single-particle cross sections did not depend largely on the choice of energy of this state. For a 0^- ground state in ^{20}N, it is impossible to access a $5/2^+$ state from $\ell = 1$ removal, so this calculation only compares with the presently observed states. In all cases of ground state spins in ^{20}N, the calculations exceed the experimental value. With a 2^- ground state, the calculated cross section to the $1/2^+$ and $3/2^+$ states in ^{19}C is 1.88 mb, which is on the same order as the experiment. When including the $5/2^+$ state, the cross section increases by an order of magnitude to 13 mb. For the case of a 0^- ground state, the cross section is also much larger than the experiment, at 11.6 mb.

The large difference in cross sections between the calculations is due to the different spectroscopic factors obtained for the two possible ground states in ^{20}N. The dominant configurations for the 2^- and 0^- states are illustrated in Figure 5.3. In the WBP interaction, the 2^- state in ^{20}N is primarily formed from the $\pi p_{1/2} \otimes (\nu d_{5/2})^5$ coupling of the valence proton and valence neutrons, with a strength of 61%. With this configuration, removal of any p-wave proton leaves the neutrons in the $d_{5/2}$ orbital. As discussed in Section 4.6.1, these configurations forms only a small part of the $1/2^+$ and $3/2^+$ states in ^{19}C, both of which are dominated by the $(\nu d_{5/2})^4 \otimes (\nu s_{1/2})^1$ and $(\nu d_{5/2})^3 \otimes (\nu s_{1/2})^2$ configurations.

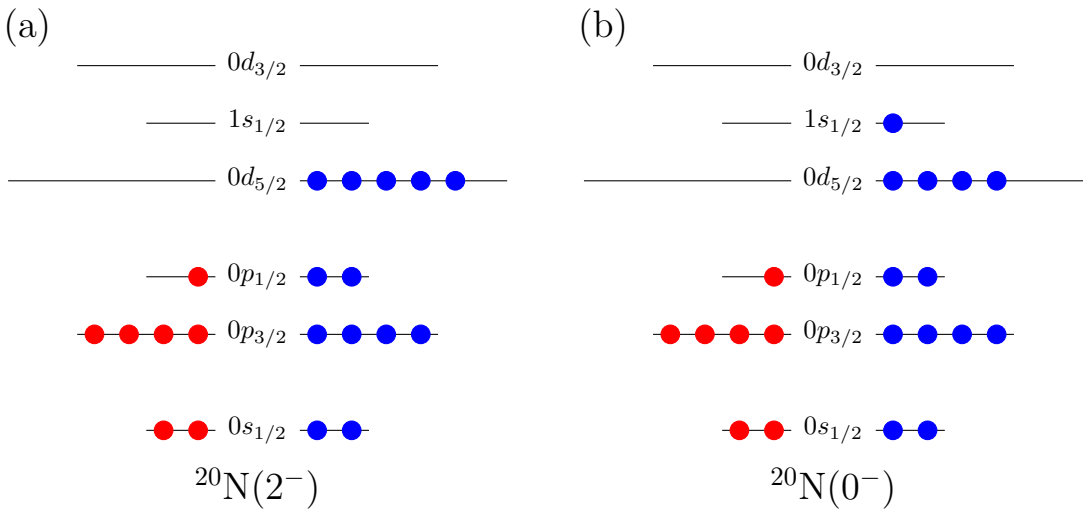

Figure 5.3: The primary configurations for the lowest 2^- (left) and 0^- states in ^{20}N, calculated with the WBP interaction. Protons are shown in red, and neutrons in blue. The 2^- configuration is formed by the coupling of the valence $0p_{1/2}$ proton to the $(0d_{5/2})^5_{J=5/2}$ neutrons. The shown configuration accounts for 61% of the total strength of the 2^- state. The 0^- configuration is formed by the coupling of the same proton to the $(0d_{5/2})^4_{J=0}1s_{1/2}$ neutrons. This accounts for 74% of the total strength in the 0^- state.

5.3 Momentum Distributions

The parallel momentum $p_{\|}$ of the recoiling ^{19}C fragments was measured at the S800 focal plane. The inclusive momentum distribution was separated into components for the ground and excited state by gating on gamma rays detected by GRETINA. A momentum spectrum was first obtained by selecting events with a gamma ray below 300 keV, since this is the highest observable energy for forward-angle detectors. This spectrum was composed of a mix of both true decays from the 209-keV state and low-energy background. A separate spectrum was produced by selecting gamma rays above 300 keV, where only background events occur. The background momentum spectrum was scaled to the expected background rate in the mixed spectrum and subtracted from the mixed spectrum to produce the distribution for the 209-keV state. This ensured that the shape of the distribution best corresponded to true

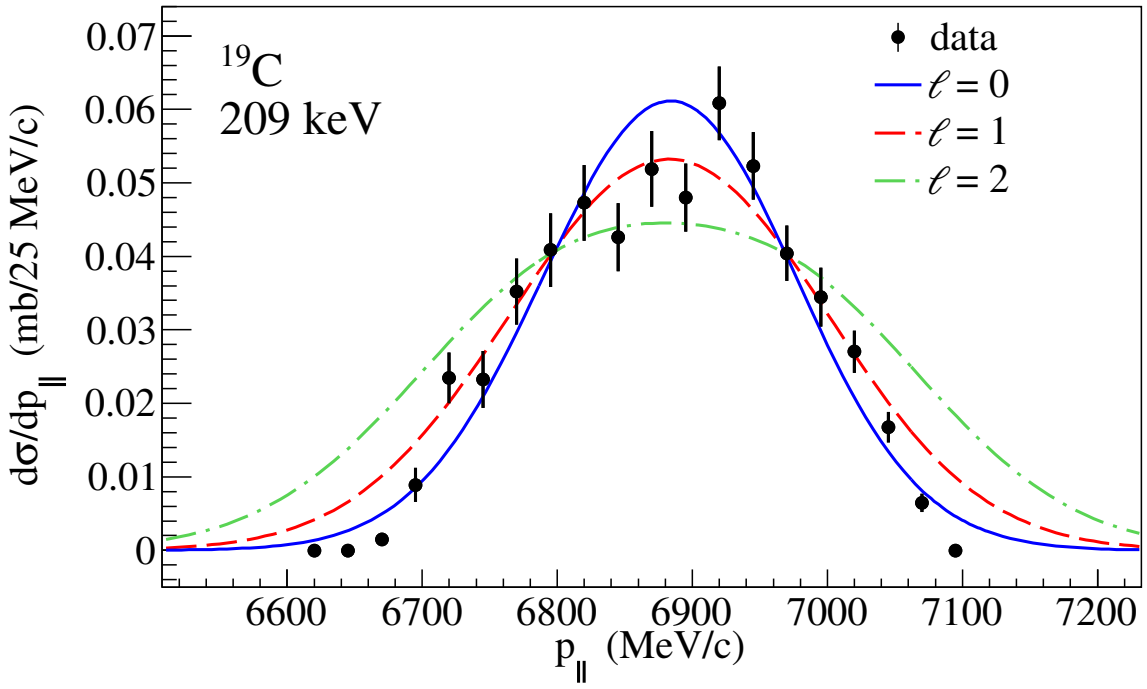

Figure 5.4: The momentum distribution along the beam axis $p_{\|}$ for the 209-keV state in ^{19}C following the one-proton knockout of ^{20}N. The black points are the data measured in the S800. Eikonal calculations are shown for s-wave (blue solid line), p-wave (red dashed line), and d-wave (green dot-dashed line) proton removal. The calculations have been normalized to the data in the region between 6710–7050 MeV/c, where the particles were fully accepted by the S800.

decay events. This spectrum was then scaled based on the average efficiency to detect gamma rays from the ^{19}C beam. Because of the long lifetime of the excited state, most decays do not occur at the target, so the efficiency was estimated based on the overall efficiency of the simulation. The result is shown by the black points in Figure 5.4. Finally, the momentum distribution for direct knockout to the ground state in ^{19}C was obtained by subtracting the excited-state distribution from the inclusive distribution. This is shown by the black points in Figure 5.5.

Theoretical momentum distributions were calculated using the eikonal prescription [23]. The output of the calculations is a symmetric distribution in the center-of-mass frame of the incoming secondary beam and target nuclei. To compare with data, several corrections

were made. Each distribution was first widened to the lab-frame width by the Lorentz factor $\gamma = 1.076$, and transformed to the measured central momentum of the ^{19}C products. The lab-frame distribution was then folded with the observed momentum of the incoming ^{20}N beam. Finally, the distribution was widened by an additional 5% to account for the difference in energy loss between the high- and low-energy portions of the beam through the beryllium target. The results are shown in Figure 5.4 for the 209-keV state and in Figure 5.5 for the ground state. Calculations were made for proton removal from s-orbitals ($\ell = 0$), p-orbitals ($\ell = 1$), and d-orbitals ($\ell = 2$). The distributions have been normalized to the experimental data. In Figure 5.4, it is clear that the data match either the $\ell = 0$ or $\ell = 1$ curves. However, the total momentum spread of the nuclei exceeds the 5% acceptance of the S800, so the shape of the distribution is cut off at high and low momentum. In the central region, where nearly all of the beam can reach the S800, the $\ell = 1$ distribution is a slightly better fit. This matches the results from the cross section-analysis, where the best agreement with theory comes from $\ell = 1$ proton removal. In Figure 5.5, the different distributions cannot be distinguished because of the large error bars, but a 2^- ground state in ^{20}N would again require $\ell = 1$ removal to reach the $1/2^+$ ground state in ^{19}C.

5.4 Discussion

Systematic errors of the inclusive and exclusive cross sections are considered separately. The errors are summarized in Table 5.3. The dominant source of error in the total cross section is due to the uncertainty in the efficiency ϵ to detect ^{19}C nuclei. The uncertainty can be broken down into two factors: the momentum acceptance of the S800, and the overall shape of the momentum distribution. Uncertainty due to the S800 acceptance occurs because total

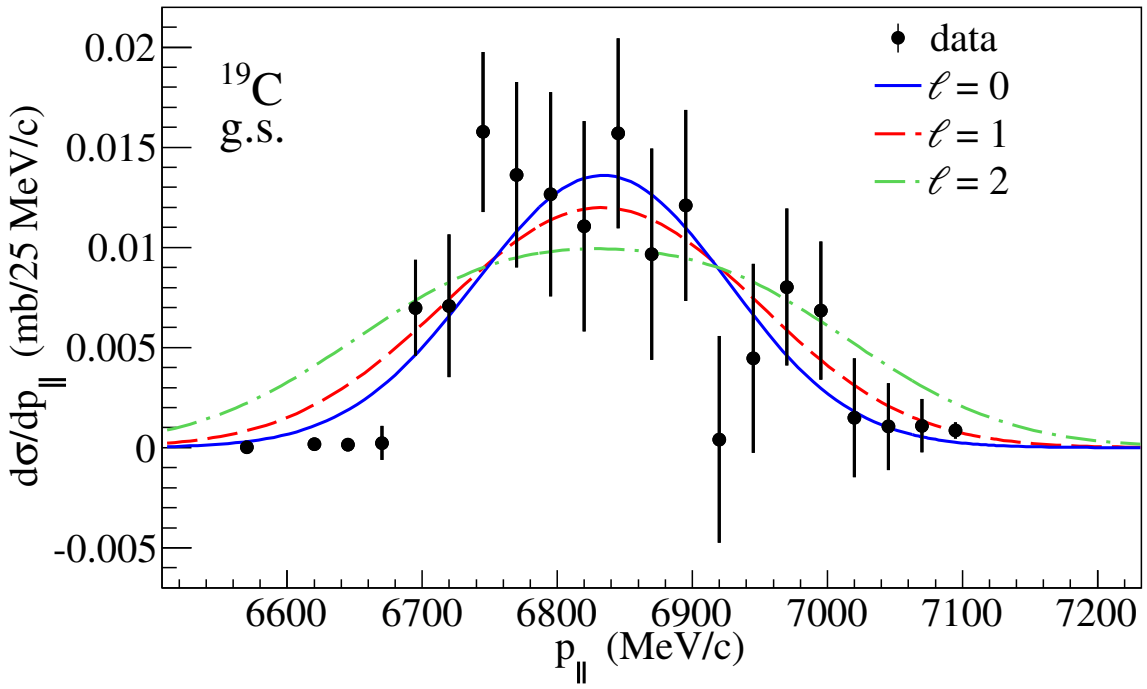

Figure 5.5: The momentum distribution along the beam axis $p_{\parallel}$ for the ground state in ^{19}C following the one-proton knockout of ^{20}N. The black points are the data measured in the S800. Eikonal calculations are shown for s-wave (blue solid line), p-wave (red dashed line), and d-wave (green dot-dashed line) proton removal. The calculations have been normalized to the data in the region between 6710–7050 MeV/c, where the particles were fully accepted by the S800.

momentum spread of the ^{19}C fragments is greater than the 5% acceptance of the S800. Because the ^{19}C beam was centered in the S800, this resulted in the beam being cut off for both the high and low energy sides of the distribution. The total cross section was calculated by matching the $\ell = 1$ theoretical momentum distribution to the experimental distribution in the central region where the acceptance is near unity. This region was defined by the magnet settings of the S800, and corresponded to 6710–7050 MeV/c. The remaining cross section from the particles which are cut off was obtained by scaling the total counts in the central region by the theoretical fraction of counts in this region. This resulted in an estimated 10% of particles which did not appear in the spectrum, and this was taken as the error on the acceptance. The shape of the momentum distribution also introduces error in the cross section determination. In the eikonal model, the distribution is symmetric; however, several previous knockout experiments have observed asymmetries in the fragment momentum distributions, appearing as tails at low energy [120–122]. Different theoretical approaches have been used to explain these tails. For removal of weakly bound neutrons from halo nuclei, coupled discretized continuum channel (CDCC) calculations have been successfully described the distributions [120], while the tail formed from removal of strongly bound nuclei has been explained as an energy dissipation mechanism during the stripping reaction [121]. Because the low-energy portion of the distribution is not observed, the possibility of a tail adds an additional estimated 10% uncertainty. Other contributions to the error in the total cross section, for example due to the gate of selecting ^{19}C in the particle identification spectrum, are much smaller and can be considered negligible.

In the calculation of exclusive cross sections, the largest error comes from determination of the in-beam efficiency of the gamma-ray detectors. Two considerations must be made: the efficiency as a function of gamma-ray energy and as a function of position of the gamma

Table 5.3: Summary of systematic errors observed for the knockout cross-section measurement. Errors for the inclusive cross section (left) and exclusive cross section to the excited $3/2^+$ state (right) are listed separately.

Inclusive		Exclusive	
Component	Error (%)	Component	Error (%)
S800 acceptance	10	Simulated absolute efficiency	9
Momentum distribution asymmetry	10	Simulated position efficiency	10
Particle identification	<1	Background determination	2

decay. The long lifetime of the $3/2^+$ state causes decays to occur, on average, about 20 cm downstream of the target. Because source calibrations for GRETINA were only made at fixed positions of the target, it was necessary to rely on simulations to determine the efficiency. As shown in Figure 3.8(a), the energy dependence is well reproduced for the line-shape configuration. However, the scaling factor required to reproduce the efficiency in the plunger configuration means that the error in the simulated efficiency can be 10%. There is also error in the simulation due to the absorption of gamma rays in the surrounding material. Because the shape of the efficiency curve is well matched for the line-shape configuration where there is no heavy degrader, this additional error is minimal. For the position dependence of the efficiency, it is not possible to compare to any real data, so there is an additional uncertainty of 10%. Another possible source of error is the determination of absolute counts in the gamma-ray spectrum, which depends on the choice of background assumed. In the present case, the error was estimated by comparing the low-energy background in coincidence with ^{9}Li and ^{18}C recoils. The difference between these two cases made a small (1%) contribution to the error.

As discussed above, all theoretical cross sections for the inclusive cross section exceed the experimental value of 0.76 mb. A similar difference between experiment and theory has been

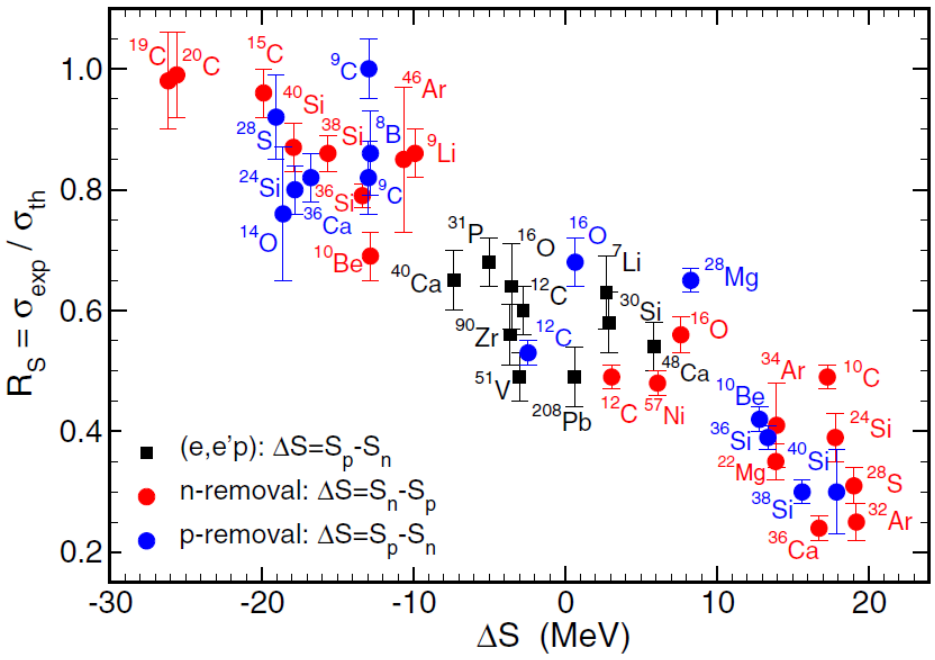

Figure 5.6: A plot showing the systematic difference between experimental and theoretical one-nucleon cross sections. The plot includes proton (blue) and neutron (red) knockout using fast beams as well as proton knockout from electron scattering (black). The reduction factor R_s is plotted as a function of ΔS, which is a measure of the difference in the Fermi energies of the protons and neutrons. Figure from Ref. [123].

found for several knockout reactions at energies near or above 100 MeV/nucleon [123]. A trend has been observed in which removal of more strongly bound nucleons results in a larger difference between the experiment and theory. This trend is shown in Figure 5.6. Here, a reduction factor $R_s = \sigma_{exp}/\sigma_{th}$ is defined as the ratio between the experimental (σ_{exp}) and theoretical (σ_{th}) cross sections. This is plotted against an asymmetry parameter ΔS for the projectile nucleus. This parameter is defined as the difference between the proton and neutron separation energies, and serves as measure of the relative Fermi surfaces of protons and neutrons. The definition of ΔS is different for proton or neutron knockout, and defines the relative binding of the removed nucleon. Therefore, points on the left are from removal of weakly bound nucleons, where the reduction factor is near unity, and points on the right are due to removal of strongly bound nucleons, where the reduction factor is much smaller. For ^{20}N, the separation energies are $S_n = 2.16$ MeV and $S_p = 17.94$ MeV [87], so that $\Delta S = 15.78$ MeV. From the theoretical calculations in Section 5.2.1, the closest value of 1.88 mb results from a 2^- ground state in ^{20}N and no bound $5/2^+$ state in ^{19}C. For this value, the reduction factor R_s is 0.40. Looking at Figure 5.6, this value falls in line with the observed trend. Other theoretical calculations which assume a different ground state in ^{20}N or a bound $5/2^+$ state in ^{19}C give cross sections nearly an order of magnitude larger, resulting in reduction factors below 0.07, much lower than any other previous value. Thus, the trend in the knockout cross section calculations supports the 2^- ground state in ^{20}N, as well as the unbound nature of the $5/2^+$ state. One point to note in Figure 5.6 is the neutron-knockout reaction from ^{20}C [80], which appears as a red point at $\Delta S = 26$ MeV and $R_s \approx 1$. This reaction also produces ^{19}C, so the theoretical calculations are similar to the present work. The two results at opposite ends of the figure highlight the observed trend as well as the need for improved theoretical framework to explain the trend.

In addition to the gamma-ray measurement [93], the current measurement provides no support for a bound $5/2^+$ state in ^{19}C. This is in line with neutron knockout reactions from ^{20}C [80, 86], including the most recent measurement [124]. Thus, there is now a consistent picture of ^{19}C which excludes a bound $5/2^+$ state.

Chapter 6

Conclusions

This work presented two experimental studies which were designed to understand the structure of the one-neutron halo nucleus ^{19}C. A lifetime measurement of the first excited state provided the first measurement of an $M1$ transition between bound states in a halo nucleus. The measured $B(M1)$ transition strength constrained the spin-parity of the excited state. Data from the one-proton knockout reaction of ^{20}N used in the same experiment also supported the spin-parity assignment of this state. The knockout reaction cross section was also used to examine the spin of the ground state in ^{20}N.

The lifetime of the first excited state at 209 keV in ^{19}C was measured using two complementary Doppler-shift techniques, the Recoil Distance Method and line-shape technique. For both methods, the lifetime was determined by fitting simulated gamma-ray spectra to the experimental spectra. The results from the two techniques were consistent, and the lifetime of the 209-keV excited state was measured to be 1.94(15) ns. This lifetime excluded a $5/2^+ \rightarrow 1/2^+$ transition and provided further support for the suggested $3/2^+$ assignment of the excited state. The calculated $B(M1; 3/2^+ \rightarrow 1/2^+)$ transition strength of $3.21(25) \times 10^{-3}$ μ_N^2, or $1.79(14) \times 10^{-3}$ W.u., indicated a strongly hindered transition, and was shown to be one of the weakest $M1$ transitions among light nuclei.

Shell model calculations were performed in order to understand the origin of the hindrance of the $3/2^+ \rightarrow 1/2^+$ transition in ^{19}C. The results of the calculations indicated that the hindrance was due to the dominance of s-wave contributions to both ground-state

and excited-state configurations. The dominance of these configurations were caused by the near degeneracy of the energies of the $1s_{1/2}$ and $0d_{5/2}$ orbitals in ^{19}C, which is a general trend for light neutron-rich nuclei. To account for the finite strength of the transition, a modified $M1$ operator incorporating a tensor component was found to play a significant role in the transition by allowing the $\Delta\ell = 2$ transition between the neutron $1s_{1/2}$ and $0d_{3/2}$ orbitals. The importance of the tensor term was shown to be a unique feature of ^{19}C, while small $B(M1)$ values observed in other *sd*-shell nuclei were due to cancellation of individual matrix elements. This work was the first measurement of a magnetic transition between bound states in a halo nucleus, and the results establish the hindered $M1$ transition as a characteristic of *s*-wave halo nuclei.

The structure of ^{19}C was also studied via a one-proton knockout reaction from a fast beam of ^{20}N. The measured inclusive cross section was compared to theoretical calculations based on the eikonal reaction model. Two sets of calculations were performed based on different assumptions for the ground-state spin of ^{20}N. The comparison was made to distinguish the possible spin-parity assignment of the ground state. The two calculations differed by an order of magnitude, offering a clear distinction between the results. The best agreement between experimental and theoretical cross sections was obtained with a 2^- ground state in ^{20}N. This state is formed from a $p_{1/2}$ proton coupled to a $5/2^+$ configuration in the ^{19}C core. This configuration in the ground state of ^{20}N indicates that the $1s_{1/2}$ and $0d_{5/2}$ orbitals are no longer degenerate in ^{20}N. The measured inclusive cross section of 0.76(10) mb was smaller than theoretical predictions, and a reduction factor was determined from the difference between the experimental and theoretical values. The reduction factor of 0.40 obtained for the 2^- ground state in ^{20}N was consistent with a general trend established by several knockout reaction studies spanning a wide range of binding energies. The data obtained in

this experiment make a valuable addition to this trend, and can aid in understanding the origin of the reduction factor.

In both the lifetime and knockout analyses, no evidence was found for the existence of a bound $5/2^+$ state in ^{19}C. No gamma-ray transition from a second state in ^{19}C was observed in the lifetime measurement, and the large increase in the knockout cross section from ^{20}N predicted from inclusion of the bound $5/2^+$ state ruled out the possibility of such a state. The results of these analyses present a consistent picture of ^{19}C, with a single bound $3/2^+$ state at 209 keV. This description is also in agreement with neutron-knockout reactions from ^{20}C, which similarly exclude such a bound $5/2^+$ state.

The present lifetime measurement can serve as a benchmark for future measurements of the magnetic response in halo nuclei. Heavier systems with deformed p-wave halos may reveal larger $M1$ strengths because of the presence of a spin-flip partner, and the present measurement establishes criteria to determine the occurrence of such a transition. The present knockout-reaction measurement demonstrates that the degeneracy of the $1s_{1/2}$ and $0d_{5/2}$ orbitals observed in ^{19}C does not persist in ^{20}N. To establish this trend among the $N = 13$ isotones more quantitatively, further studies on the excited states in ^{20}N are necessary. Such results will be important in the determination of broad trends in the nuclear structure of neutron-rich nuclei.

REFERENCES

REFERENCES

[1] "Chart of Nuclides," `http://www.nndc.bnl.gov/chart` .

[2] M.G. Mayer, Phys. Rev. **75**, 1969 (1949).

[3] K. Heyde, *Basic Ideas and Concepts in Nuclear Physics*, 2nd ed. (Institute of Physics Publishing, London, 1999).

[4] J. Suhonen, *From Nucleons to Nucleus* (Springer-Verlag, Berlin, 2007).

[5] O. Haxel, J.H.D. Jensen, and H.E. Seuss, Phys. Rev. **75**, 1766 (1949).

[6] R.F. Casten, *Nuclear Structure from a Simple Perspective* (Oxford University Press, New York, 1990).

[7] A. Ozawa, T. Kobayashi, T. Suzuki, K. Yoshida, and I. Tanihata, Phys. Rev. Lett. **84**, 5493 (2000).

[8] S.N. Liddick, P.F. Mantica, R. Broda, B.A. Brown, M.P. Carpenter, A.D. Davies, B. Fornal, T. Glasmacher, D.E. Groh, M. Honma, M. Horoi, R.V.F. Janssens, T. Mizusaki, D.J. Morrissey, A.C. Morton, W.F. Mueller, T. Otsuka, J. Pavan, H. Schatz, A. Stolz, S.L. Tabor, B.E. Tomlin, and M. Wiedeking, Phys. Rev. C **70**, 064303 (2004).

[9] T. Suzuki and T. Otsuka, Phys. Rev. C **56**, 847 (1997).

[10] H. Iwasaki, T. Motobayashi, H. Akiyoshi, Y. Ando, N. Fukuda, H. Fujiwara, Zs. Fülöp, K. I. Hahn, Y. Higurashi, M. Hirai, I. Hisanaga, N. Iwasa, T. Kijima, A. Mengoni, T. Minemura, T. Nakamura, M. Notani, S. Ozawa, H. Sagawa, H. Sakurai, S. Shimoura, S. Takeuchi, T. Teranishi, Y. Yanagisawa, and M. Ishihara, Eur. Phys. J. A **13**, 55 (2002).

[11] C. Thibault, R. Klapisch, C. Rigaud, A.M. Poskanzer, R. Prieels, L. Lessard, and W. Reisdorf, Phys. Rev. C **12**, 644 (1975).

[12] K. Tanaka, T. Yamaguchi, T. Suzuki, T. Ohtsubo, M. Fukuda, D. Nishimura, M. Takechi, K. Ogata, A. Ozawa, T. Izumikawa, T. Aiba, N. Aoi, H. Baba, Y. Hashizume, K. Inafuku, N. Iwasa, K. Kobayashi, M. Komuro, Y. Kondo, T. Kubo, M. Kurokawa, T. Matsuyama, S. Michimasa, T. Motobayashi, T. Nakabayashi, S. Nakajima, T. Nakamura, H. Sakurai,1 R. Shinoda, M. Shinohara, H. Suzuki, E. Takeshita, S. Takeuchi, Y. Togano, K. Yamada, T. Yasuno, and M. Yoshitake, Phys. Rev. Lett. **104**, 062701 (2010).

[13] I. Tanihata, H. Hamagaki, O. Hashimoto, Y. Shida, N. Yoshikawa, K. Sugimoto, O. Yamakawa, T. Kobayashi, and N. Takahashi, Phys. Rev. Lett. **55**, 2676 (1985).

[14] I. Tanihata, H. Hamagaki, O. Hashimoto, S. Nagamiya, Y. Shida, N. Yoshikawa, O. Yamakwa, K. Sugimoto, T. Kobayashi, D.E. Greiner, N. Takahashi, and Y. Nojiri, Phys. Lett. B **160**, 380 (1985).

[15] T. Kobayashi, O. Yamakawa, K. Omata, K. Sugimoto, T. Shimoda, N. Takahashi, and I. Tanihata, Phys. Rev. Lett. **60**, 2599 (1988).

[16] N.A. Orr, N. Anantaraman, S.M. Austin, C.A. Bertulani, K. Hanold, J.H. Kelley, D.J. Morrissey, B.M. Sherrill, G.A. Souliotis, M. Thoennessen, J.S. Winfield, and J.A. Winger, Phys. Rev. Lett. **69**, 2050 (1992).

[17] T. Aumann, D. Aleksandrov, L. Axelsson, T. Baumann, M.J.G. Borge, L.V. Chulkov, J. Cub, W. Dostal, B. Eberlein, Th.W. Elze, H. Emling, H. Geissel, V.Z. Goldberg, M. Golovkov, A. Grünschloß, M. Hellström, K. Hencken, J. Holeczek, R. Holzmann, B. Jonson, A.A. Korshenninikov, J.V. Kratz, G. Kraus, R. Kulessa, Y. Leifels, A. Leistenschneider, T. Leth, I. Mukha, G. Múnzenberg, F. Nickel, T. Nilsson, G. Nyman, B. Petersen, M. Pfützner, A. Richter, K. Riisager, C. Scheidenberger, G. Schrieder, W. Schwab, H. Simon, M.H. Smedberg, M. Steiner, J. Stroth, A. Surowiec, T. Suzuki, O. Tengblad, and M.V. Zhukov, Phys. Rev. C **59**, 1252 (1999).

[18] T. Nakamura, N. Fukuda, T. Kobayashi, N. Aoi, H. Iwasaki, T. Kubo, A. Mengoni, M. Notani, H. Otsu, H. Sakurai, S. Shimoura, T. Teranishi, Y.X. Watanabe, K. Yoneda, and M. Ishihara, Phys. Rev. Lett. **83**, 1112 (1999).

[19] R. Palit, P. Adrich, T. Aumann, K. Boretzky, B.V. Carlson, D. Cortina, U. Datta Pramanik, Th.W. Elze, H. Emling, H. Geissel, M. Hellström, K.L. Jones, J.V. Kratz, R. Kulessa, Y. Leifels, A. Leistenschneider, G. Münzenberg, C. Nociforo, P. Reiter, H. Simon, K. Sümmerer, and W. Walus (LAND/FRS Collaboration), Phys. Rev. C **68**, 034318 (2003).

[20] T. Kobayashi, S. Shimoura, I. Tanihata, K. Katori, K. Matsuta, T. Minamisono, K. Sugimoto, W. Müller, D.L. Olson, T.J.M. Symons, and H. Wieman, Phys. Lett. B **232**, 51 (1989).

[21] N. Kobayashi, T. Nakamura, Y. Kondo, J.A. Tostevin, Y. Utsuno, N. Aoi, H. Baba, R. Barthelemy, M.A. Famiano, N. Fukuda, N. Inabe, M. Ishihara, R. Kanungo, S. Kim, T. Kubo, G.S. Lee, H.S. Lee, M. Matsushita, T. Motobayashi, T. Ohnishi, N.A. Orr, H. Otsu, T. Otsuka, T. Sako, H. Sakurai, Y. Satou, T. Sumikama, H. Takeda, S. Takeuchi, R. Tanaka, Y. Togano, and K. Yoneda, Phys. Rev. Lett. **112**, 242501 (2014).

[22] I. Tanihata, H. Savajols, and R. Kanungo, Prog. Part. Nucl. Phys. **68** (2013).

[23] P.G. Hansen and J.A. Tostevin, Annu. Rev. Nucl. Part. Sci. **53**, 219 (2003).

[24] A. Zilges, V. Derya, D. Savran, A. Hennig, S.G. Pickstone, and M. Spieker, J. of Phys. Conf. Ser. **580**, 012052 (2015).

[25] P.G. Hansen and A.S. Jensen, Annu. Rev. Nucl. Part. Sci. **95**, 591 (1995).

[26] K. Ikeda, Nucl. Phys. A **538**, 355c (1992).

[27] H. Beer, M. Wiescher, F. Käppeler, J .Görres, and P.E. Koehler, Astrophys. J. **387**, 258 (1992).

[28] R. Reifarth, M. Heil, C. Forssén, U. Besserer A. Couture S. Dababneh, L. Dörr, J. Görres, R.C. Haight, F. Käppeler, A. Mengoni, S. O'Brien, N. Patronis, R. Plag, R.S. Rundberg, M. Wiescher, and J.B. Wilhelmy, Phys. Rev. C **77**, 015804 (2008).

[29] T. Nakamura, N. Fukuda, N. Aoi, N. Imai, M. Ishihara, H. Iwasaki, T. Kobayashi, T. Kubo, A. Mengoni, T. Motobayashi, M. Notani, H. Otsu, H. Sakurai, S. Shimoura, T. Teranishi, Y.X. Watanabe, and K. Yoneda, Phys. Rev. C **79**, 035805 (2009).

[30] W. Loveland, Phys. Rev. C **76**, 014612 (2007).

[31] J.J. Kolata, V. Guimarães, D. Peterson, P. Santi, R. White-Stevens, P.A. DeYoung, G.F. Peaslee, B. Hughey, B. Atalla, M. Kern, P.L. Jolivette, J.A. Zimmerman, M.Y. Lee, F.D. Becchetti, E.F. Aguilera, E. Martinez-Quiroz, and J.D. Hinnefeld, Phys. Rev. Lett. **81** 4580 (1998).

[32] Yu.E. Penionzhkevich, V.I. Zagrebaev, S.M. Lukyanov, and R. Kalpakchieva, Phys. Rev. Lett. **96** 162701 (2006).

[33] R. Raabe, J.L. Sida, J.L Charvet, N. Alamanos, C. Angulo, J.M. Casadjan, S. Courtin, A. Drouart, D.J.C. Durand, P. Figuera, A. Gillibert, S. Heinrich, C. Jouanne, V. Lapoux, A. Lepine, A. Musumarra, L. Nalpas, D. Pierroutsakou, M. Romoli, K. Rusek, and M. Trotta, Nature **431** 823 (2004).

[34] A. Di Pietro, P. Figuera, F. Amorini, C. Angulo, G. Cardella, S. Cherubini, T. Davinson, D. Leanza, J. Lu, H. Mahmud, M. Milin, A. Musumarra, A. Ninane, M. Papa, M.G. Pellegriti, R. Raabe, F. Rizzo, C. Ruiz, A.C. Shotter, N. Soic, S. Tudisco, and L. Weissman, Phys. Rev. C 69 044613 (2004).

[35] N. Keeley, R. Raabe, N. Alamanos, and J.L. Sida, Prog. Part. Nucl. Phys. **59**, 579 (2007).

[36] V.F. Weisskopf, Phys. Rev. **83**, 1073 (1951).

[37] A.S. Goldhaber, Phys. Lett. B **53**, 306 (1974).

[38] T. Glasmacher, Annu. Rev. Nucl. Part. Sci. **53**, 219 (1998).

[39] W.F. Mueller, J.A. Church, T. Glasmacher, D. Gutknecht, G. Hackman, P.G. Hansen, Z. Hu, K.L. Miller, P. Quirin, Nucl. Instrum. Meth. A **466**, 492 (2001).

[40] S. Paschalis, I.Y. Lee, A.O. Macchiavelli, C.M.Campbell, M. Cromaz, S. Gros, J. Pavan, J. Qian, R.M. Clark, H.L. Crawford, D. Doering, P. Fallon, C. Lionberger, T. Loew, M. Petri, T.Stezelberger, S. Zimmerman, D.C. Radford, K. Lagergren, D. Weisshaar, R. Winkler, T. Glasmacher, J.T. Anderson, and C.W. Beausang, Nucl. Instrum. Meth. Phys. Res., Sect. A **709**, 44 (2013).

[41] V. Maddalena, T. Aumann, D. Bazin, B.A. Brown, J.A. Caggiano, B. Davids, T. Glasmacher, P.G. Hansen, R.W. Ibbotson, A. Navin, B.V. Pritychenko, H. Scheit, B.M. Sherrill, M. Steiner, J.A. Tostevin, and J. Yurkon, Phys. Rev. C **63**, 024613 (2001).

[42] J.S. Winfield, S. Fortier, W.N. Catford, S. Pita, N.A. Orr, J. Van de Wiele, Y. Blumenfeld, R. Chapman, S.P.G. Chappell, N.M. Clarke, N. Curtis, M. Freer, S. Galésa, H. Langevin-Joliot, H. Laurent, I. Lhenry, J.M. Maison, P. Roussel-Chomaz, M. Shawcross, K. Spohr, T. Suomijärvi, and A. de Vismes, Nucl. Phys. A **683**, 48 (2001).

[43] A. Chester, P. Adrich, A. Becerril, D. Bazin, C.M. Campbell, J.M. Cook, D.-C. Dinca, W.F. Mueller, D. Miller, V. Moeller, R.P. Norris, M. Portillo, K. Starosta, A. Stolz, J.R. Terry, H. Zwahlen, C. Vaman, and A. Dewald, Nucl. Instrum. Meth. A **1**, 230 (2006).

[44] G.F. Knoll, *Radiation Detection and Measurement*, Fourth ed. (John Wiley & Sons, Hoboken, NJ, 2010).

[45] "XCOM: Photon Cross Sections Database," `http://www.nist.gov/pml/data/xcom` , Accessed March 3, 2016.

[46] P. Doornenbal, P. Reiter, H. Grawe, T. Saito, A. Al-Khatib, A. Banu, T. Beck, F. Becker, P. Bednarczyk, G. Benzoni, A. Bracco, A. Bürger,L. Caceres, F. Camera, S. Chmel, F.C.L. Crespi, H. Geissel, J. Gerl, M. Goórska, J. Grębosz, H. Hübel, M. Kavatsyuk, O. Kavatsyuk, M. Kmiecik, I. Kojouharov, N. Kurz, R. Lozeva, A. Maj, S. Mandal, W. Meczynski, B. Million, Zs. Podolyák, A. Richard, N. Saito, H. Schaffner, M. Seidlitz, T. Striepling, J. Walker, N. Warr, H. Weick, O. Wieland, M. Winkler, and H.J. Wollersheim, Nucl. Instrum. Meth. Phys. Res., Sect. A **613**, 218 (2010).

[47] A. Lemasson, H. Iwasaki, C. Morse, D. Bazin, T. Baugher, J.S. Berryman, A. Dewald, C. Fransen, A. Gade, S. McDaniel, A. Nichols, A. Ratkiewicz, S. Stroberg, P. Voss, R. Wadsworth, D. Weisshaar, K. Wimmer, and R. Winkler, Phys. Rev. C **85**, 041303(R) (2012).

[48] T.K. Alexander and K.W. Allen, Can. J. Phys. **43**, 1563 (1965).

[49] A. Dewald, O. Möller, and P. Petkov, Prog. Part. Nucl. Phys. **67**, 786 (2012).

[50] M. Oshima, N.R. Johnson, F.K. McGowan, C. Baktash, I.Y. Lee, Y. Schutz, and R.V. Ribas, Phys. Rev. C **33**, 1988 (1986).

[51] D. Smalley, H. Iwasaki, P. Navrátil, R. Roth, J. Langhammer, V.M. Bader, D. Bazin, J.S. Berryman, C.M. Campbell, J. Dohet-Eraly, P. Fallon, A. Gade, C. Langer, A. Lemasson, C. Loelius, A.O. Macchiavelli, C. Morse, J. Parker, S. Quaglioni, F. Recchia, S.R. Stroberg, D. Weisshaar, K. Whitmore, and K. Wimmer, Phys. Rev. C **92**, 064314 (2015).

[52] D.B. Fossan and E.K. Warburton, in *Nuclear Spectroscopy and Reactions, Part C*, edited by J. Cerny (Academic Press, New York, 1974).

[53] I.J. Thompson and F.M. Nunes, *Nuclear Reactions for Astrophysics* (Cambridge University Press, New York, 2009).

[54] R.J. Glauber, *Lectures in Theoretical Physics, Vol. 1*, ed. by W.E. Brittin, (Interscience, New York, 1959).

[55] A.E.L. Dieperink and T. de Forest, Phys. Rev. C **10**, 543 (1974).

[56] D.J. Morrissey for the NSCL Staff, Nucl. Phys. A **616**, 45c (1997).

[57] D.J. Morrissey, B.M. Sherrill, M. Steiner, A. Stolz, and I. Wiedenhoever, Nucl. Instrum. Meth. Phys. Res., Sect. B **204**, 90 (2003).

[58] D. Bazin, J.A. Caggiano, B.M. Sherrill, J. Yurkon, and A. Zeller, Nucl. Instrum. Meth. Phys. Res., Sect. B **204**, 629 (2003).

[59] P.A. Zavodszky, B. Arend, D. Cole, J. DeKamp, G. Machicoane, F. Marti, P. Miller, J. Moskalik, J. Ottarson, J. Vincent, and A. Zeller, Nucl. Instrum. Meth. Phys. Res., Sect. B **241**, 959 (2005).

[60] P.A. Zavodszky, B. Arend, D. Cole, J. DeKamp, G. Machicoane, F. Marti, P. Miller, J. Moskalik, J. Ottarson, J. Vincent, and A. Zeller, Rev. Sci. Instrum. **77**, 03A334 (2006).

[61] G. Machiocoane, D. Cole, J. Ottarson, J. Stetson, and P. Zavodszky, Rev. Sci. Instrum. **77**, 03A322 (2006).

[62] J.P. Dufour, R. Del Moral, H Emmermann, F. Hubert, D. Jean, C. Poinot, M.S. Pravikoff, A. Fleury, H. Delagrange, and K.-H. Schmidt, Nucl. Instrum. Meth. Phys. Res., Sect. A **248**, 267 (1986).

[63] H. Iwasaki, A. Dewald, T. Braunroth, C. Fransen, D. Smalley, A. Lemasson, C. Morse, K. Whitmore, and C. Loelius, Nucl. Instrum. Meth. Phys. Res., Sect. A **11**, 123 (2016).

[64] C. Morse, H. Iwasaki, A. Lemasson, T. Baugher, D. Bazin, J.S. Berryman, A. Dewald, C. Fransen, A. Gade, S. McDaniel, A.J. Nichols, A. Ratkiewicz, S.R. Stroberg, P. Voss, R. Wadsworth, D. Weisshaar, K. Wimmer, and R. Winkler, Phys. Rev. C **90**, 034310 (2014).

[65] "S800 Spectrograph," `https://groups.nscl.msu.edu/s800/Technical/Tech_frameset.htm` , Accessed May 8, 2016.

[66] J. Yurkon, D. Bazin, W. Benenson, D.J. Morrissey, B.M. Sherrill, D. Swan, and R. Swanson, Nucl. Instrum. Meth. Phys. Res., Sect. A **422**, 291 (1999).

[67] "S800 Documentation," `https://wikihost.nscl.msu.edu/S800Doc/doku.php?id=detectors` , Accessed May 8, 2016.

[68] M. Berz, K. Joh, J.A. Nolen, B.M. Sherrill, and A.F. Zeller, Phys. Rev. C **47**, 537 (1993).

[69] S. Agostinelli *et al.*, Nucl. Instrum. Meth. Phys. Res., Sect. A **506**, 250 (2003).

[70] P. Adrich, D. Enderich, D. Miller, V. Moeller, R.P. Norris, K. Starosta, C. Vaman, P. Voss, and A. Dewald, Nucl. Instrum. Meth. Phys. Res., Sect. A **598**, 454 (2009).

[71] R. Brun and F. Rademakers, Nucl. Instrum. Meth. Phys. Res., Sect. A **389**, 81 (1997).

[72] G. Cowan, *Statistical Data Analysis* (Oxford University Press, New York, 1998).

[73] T. Aumann and T. Nakamura, Phys. Scr. **T152**, 014012 (2013).

[74] T. Nakamura, S. Shimoura, T. Kobayashi, T. Teranishi, K. Abe, N. Aoi, Y. Doki, M. Fujimaki, N. Inabe, N. Iwasa, K. Katori, T. Kubo, H. Okuno, T. Suzuki, I. Tanihata, Y. Watanabe, A. Yoshida, M. Ishihara, Phys. Lett. B **331**, 296 (1994).

[75] U. Datta Pramanika, T. Aumann, K. Boretzky, B.V. Carlson, D. Cortina, Th.W. Elze, H. Emling, H. Geissel, A. Grünschloß, M. Hellström, S. Ilievski, J.V. Kratz, R. Kulessa, Y. Leifels, A. Leistenschneider, E. Lubkiewicz, G. Münzenberg, P. Reiter, H. Simon, K. Sümmerer, E. Wajda, and W. Walus, Phys. Lett. B **551**, 63 (2003).

[76] W. Geithner, S. Kappertz, M. Keim, P. Lievens, R. Neugart, L. Vermeeren, S. Wilbert, V.N. Fedoseyev, U. KÃűster, V.I. Mishin, V. Sebastian, and ISOLDE Collaboration, Phys. Rev. Lett. **83**, 3792 (1999).

[77] A. Takamine, M. Wada, K. Okada, T. Sonoda, P. Schury, T. Nakamura, Y. Kanai, T. Kubo, I. Katayama, S. Ohtani, H. Wollnik, and H.A. Schuessler, Phys. Rev. Lett. **112**, 162502 (2014).

[78] D. Suzuki, H. Iwasaki, H.J. Ong, N. Imai, H. Sakurai, T. Nakao, N. Aoi, H. Baba, S. Bishop, Y. Ichikawa, M. Ishihara, Y. Kondo, T. Kubo, K. Kurita, T. Motobayashi,

T. Nakamura, T. Okumura, T.K. Onishi, S. Ota, M.K. Suzuki, S. Takeuchi, Y. Togano, and Y. Yanagisawa, Phys. Lett. B **666**, 222 (2008).

[79] A. Bohr and B.R. Mottelson *Nuclear Structure*, (W. A. Benjamin, New York, 1969), Vol. 1.

[80] N. Kobayashi, T. Nakamura, J.A. Tostevin, Y. Kondo, N. Aoi, H. Baba, S. Deguchi, J. Gibelin, M. Ishihara, Y. Kawada, T. Kubo, T. Motobayashi, T. Ohnishi, N.A. Orr, H. Otsu, H. Sakurai, Y. Satou, E.C. Simpson, T. Sumikama, H. Takeda, M. Takechi, S. Takeuchi, K.N. Tanaka, N. Tanaka, Y. Togano, and K. Yoneda, Phys. Rev. C **86**, 054604 (2012).

[81] D. Bazin, B.A. Brown, J. Brown, M. Fauerbach, M. Hellstrom, S.E. Hirzebruch, J.H. Kelley, R.A. Kryger, D.J. Morrissey, R. Pfaff, C.F. Powell, B.M. Sherrill, and M. Thoennessen, Phys. Rev. Lett. **74**, 3569 (1995).

[82] R. Kanungo, I. Tanihata, Y. Ogawa, H. Toki, and A. Ozawa, Nucl. Phys. A **677**, 171 (2000).

[83] D. Bazin, W. Benenson, B.A. Brown, J. Brown, B. Davids, M. Fauerbach, P.G. Hansen, P. Mantica, D.J. Morrissey, C.F. Powell, B.M. Sherrill, and M. Steiner, Phys. Rev. C **57**, 2156 (1998).

[84] F.M. Marqués, E. Liegard, N.A. Orr, J.C. Angélique, L. Axelsson, G. Bizard, W.N. Catford, N.M. Clarke, G. Costa, M. Freer, S. Grévy, D. Guillemaud-Mueller, G.J. Gyapong, F. Hanappe, P.G. Hansen, B. Heusch, B. Jonson, C. Le Brun, F.R. Lecolley, F. Lefebvres, M. Lewitowicz, G. Martínez, A.C. Mueller, T. Nilsson, A. Ninane, G. Nyman, B. Petersen, F. Pougheon, K. Riisager, M.G. Saint-Laurent, Y. Schutz, M. Smedberg, O. Sorlin, L. Stuttgé, and D.D. Warner, Phys. Lett. B **381**, 407 (1996).

[85] T. Baumann, M.J.G. Borge, H. Geissel, H. Lenske, K. Markenroth, W. Schwab, M.H. Smedberg, T. Aumann, L. Axelsson, U. Bergmann, D. Cortina-Gil, L. Fraile, M. Hellström, M. Ivanov, N. Iwasa, R . Janik, B. Jonson, G. Münzenberg, F. Nickel, T. Nilsson, A. Ozawa, A. Richter, K. Riisager, C. Scheidenberger, G. Schrieder, H. Simon, B. Sitar, P. Strmen, K. SÃijmmerer, T. Suzuki, M. Winkler, H. Wollnik, and M.V. Zhukov, Phys. Lett. B **439**, 256 (1998).

[86] A. Ozawa, Y. Hashizume, Y. Aoki, K. Tanaka, T. Aiba, N. Aoi, H. Baba, B.A. Brown, M. Fukuda, K. Inafuku, N. Iwasa, T. Izumikawa, K. Kobayashi, M. Komuro, Y. Kondo, T. Kubo, M. Kurokawa, T. Matsuyama, S. Michimasa, T. Motobayashi, T. Nakabayashi, S. Nakajima, T. Nakamura, T. Ohtsubo, H. Sakurai, R. Shinoda, M. Shinohara, H. Suzuki, T. Suzuki, M. Takechi, E. Takeshita, S. Takeuchi, Y. Togano, K. Yamada, T. Yamaguchi, T. Yasuno, and M. Yoshitake, Phys. Rev. C **84**, 064315 (2011).

[87] M. Wang, G. Audi, A.H. Wapstra, F.G. Kondev, M. MacCormick, X. Xu, and B. Pfeiffer, Chin. Phys. C **36**, 1603 (2012).

[88] M. Stanoiu, F. Azaiez, F. Becker, M. Belleguic, C. Borcea, C. Bourgeois, B.A. Brown, Z. Dlouhý, Z. Dombrádi, Z. Fülöp, H. Grawe, S. Grévy, F. Ibrahim, A. Kerek, A. Krasznahorkay, M. Lewitowicz, S. Lukyanov, H. van der Marel, P. Mayet, J. Mrázek, S. Mandal, D. Guillemaud-Mueller, F. Negoita, Y.E. Penionzhkevich, Z. Podolyák, P. Roussel-Chomaz, M.G. Saint-Laurent, H. Savajols, O. Sorlin, G. Sletten, D. Sohler, J. Timár, C. Timis, and A. Yamamoto, Eur. Phys. J. A **20**, 95 (2004).

[89] Z. Elekes, Zs. Dombrádi, R. Kanungo, H. Baba, Zs. Fülöp, J. Gibelin, Á. Horváthe, E. Ideguchi, Y. Ichikawa, N. Iwasa, H. Iwasaki, S. Kanno, S. Kawai, Y. Kondo, T. Motobayashi, M. Notani, T. Ohnishi, A. Ozawa, H. Sakurai, S. Shimoura, E. Takeshita, S. Takeuchi, I. Tanihata, Y. Togano, C. Wu, Y. Yamaguchi, Y. Yanagisawa, A. Yoshida, and K. Yoshida, Phys. Lett. B **614**, 174 (2005).

[90] M. Thoennessen, S. Mosby, N.S. Badger, T. Baumann, D. Bazin, M. Bennett, J. Brown, G. Christian, P.A. DeYoung, J.E. Finck, M. Gardner, E.A. Hook, B. Luther, D.A. Meyer, M. Mosby, W.F. Rogers, J.K. Smith, A. Spyrou, and M.J. Strongman, Nucl. Phys. A **912**, 1 (2013).

[91] Y. Satou, T. Nakamura, N. Fukuda, T. Sugimoto, Y. Kondo, N. Matsui, Y. Hashimoto, T. Nakabayashi, T. Okumura, M. Shinohara, T. Motobayashi, Y. Yanagisawa, N. Aoi, S. Takeuchi, T. Gomi, Y. Togano, S. Kawai, H. Sakurai, H.J. Ong, T.K. Onishi, S. Shimoura, M. Tamaki, T. Kobayashi, H. Otsu, Y. Matsuda, N. Endo, M. Kitayama, M. Ishihara, Phys. Lett. B **660**, 320 (2008).

[92] R. Kanungo, Z. Elekes, H. Baba, Zs. Dombrádi, Zs. Fülöp, J. Gibelin, Á. Horváth, Y. Ichikawa, E. Ideguchi, N. Iwasa, H. Iwasaki, S. Kawai, Y. Kondo, T. Motobayashi, M. Notani, T. Ohnishi, A. Ozawa, H. Sakurai, S. Shimoura, E. Takeshita, S. Takeuchi, I. Tanihata, Y. Togano, C. Wu, Y. Yamaguchi, Y. Yanagisawa, A. Yoshida, and K. Yoshida, Nucl. Phys. A **757**, 315 (2005).

[93] K. Whitmore, D. Smalley, H. Iwasaki, T. Suzuki, V.M. Bader, D. Bazin, J.S. Berryman, B.A. Brown, C.M. Campbell, P. Fallon, A. Gade, C. Langer, A. Lemasson, C. Loelius, A.O. Macchiavelli, C. Morse, T. Otsuka, J. Parker, F. Recchia, S.R. Stroberg, D. Weisshaar, and K. Wimmer, Phys. Rev. C **91**, 041303(R) (2015).

[94] H. Iwasaki, A. Lemasson, C. Morse, A. Dewald, T. Braunroth, V.M. Bader, T. Baugher, D. Bazin, J. S. Berryman, C. M. Campbell, A. Gade, C. Langer, I.Y. Lee, C. Loelius, E. Lunderberg, F. Recchia, D. Smalley, S. R. Stroberg, R. Wadsworth, C. Walz, D. Weisshaar, A. Westerberg, K. Whitmore, and K. Wimmer, Phys. Rev. Lett. **112** 142502 (2014).

[95] P. Voss, T. Baugher, D. Bazin, R.M. Clark, H.L. Crawford, A. Dewald, P. Fallon, A. Gade, G.F. Grinyer, H. Iwasaki, A.O. Macchiavelli, S. McDaniel, D. Miller, M. Petri,

A. Ratkiewicz, W. Rother, K. Starosta, K.A. Walsh, D. Weisshaar, C. Forssén, R. Roth, and P. Navrátil, Phys. Rev. C **86**, 011303(R) (2012).

[96] M. Petri, S. Paschalis, R.M. Clark, P. Fallon, A.O. Macchiavelli, K. Starosta, T. Baugher, D. Bazin, L. Cartegni, H.L. Crawford, M. Cromaz, U. Datta Pramanik, G. de Angelis, A. Dewald, A. Gade, G.F. Grinyer, S. Gros, M. Hackstein, H.B. Jeppesen, I.Y. Lee, S. McDaniel, D. Miller, M.M. Rajabali, A. Ratkiewicz, W. Rother, P. Voss, K.A. Walsh, D. Weisshaar, M. Wiedeking, B.A. Brown, C. Forssén, P. Navrátil, and R. Roth, Phys. Rev. C **86**, 044329 (2012).

[97] P.M. Endt, At. Data Nucl. Data Tables **55**, 171 (1993).

[98] M. Petri, P. Fallon, A.O. Macchiavelli, S. Paschalis, K. Starosta, T. Baugher, D. Bazin, L. Cartegni, R.M. Clark, H.L. Crawford, M. Cromaz, A. Dewald, A. Gade, G.F. Grinyer, S. Gros, M. Hackstein, H.B. Jeppesen, I.Y. Lee, S. McDaniel, D. Miller, M.M. Rajabali, A. Ratkiewicz, W. Rother, P. Voss, K.A. Walsh, D. Weisshaar, M. Wiedeking, and B.A. Brown, Phys. Rev. Lett. **107**, 102501 (2011).

[99] "Evaluated Nuclear Structure Data File," `http://www.nndc.bnl.gov/ensdf` , Accessed March 2014.

[100] Y. Fujita, Y. Shimbara, I. Hamamoto, T. Adachi, G.P.A. Berg, H. Fujimura, H. Fujita, J. GÃűrres, K. Hara, K. Hatanaka, J. Kamiya, T. Kawabata, Y. Kitamura, Y. Shimizu, M. Uchida, H.P. Yoshida, M. Yoshifuku, and M. Yosoi, Phys. Rev. C 66, 044313 (2002)

[101] W.A. Richter, S. Mkhize, and B.A. Brown, Phys. Rev. C **78**, 064302 (2008).

[102] E.K. Warburton and B.A. Brown, Phys. Rev. C **46**, 923 (1992).

[103] T. Suzuki and T. Otsuka, Phys. Rev. C **78**, 061301(R) (2008).

[104] C. Yuan, T. Suzuki, T. Otsuka, F. Xu, and N. Tsunoda, Phys. Rev. C **85**, 064324 (2012).

[105] T. Suzuki, R. Fujimoto, and T. Otsuka, Phys. Rev. C **67**, 044302 (2003).

[106] D.J. Millener and D. Kurath, Nucl. Phys. A **255**, 315 (1975).

[107] T. Otsuka, T. Suzuki, M. Honma, Y. Utsuno, N. Tsunoda, K. Tsukiyama, and M. Hjorth-Jensen, Phys. Rev. Lett. **104**, 012501 (2010).

[108] B.A. Brown and B.H. Wildenthal, Annu. Rev. Nucl. Part. Sci. **38**, 29 (1988).

[109] C.S. Sumithrarachchi, D.W. Anthony, P.A. Lofy, and D.J. Morrissey, Phys. Rev. C **74**, 024322 (2006).

[110] D. Sohler, M. Stanoiu, Zs. Dombrádi, F. Azaiez, B.A. Brown, M.G. Saint-Laurent, O. Sorlin, Yu.-E. Penionzhkevich, N.L. Achouri, J.C. Angélique, M. Belleguic,

C. Borcea, C. Bourgeois, J.M. Daugas, F. De Oliveira-Santos, Z. Dlouhy, C. Donzaud, J. Duprat, Z. Elekes, S. Grévy, D. Guillemaud-Mueller, F. Ibrahim, S. Leenhardt, M. Lewitowicz, M.J. Lopez-Jimenez, S.M. Lukyanov, W. Mittig, J. Mrázek, F. Negoita, Zs. Podolyák, M.G. Porquet, F. Pougheon, P. Roussel-Chomaz, H. Savajols, G. Sletten, Y. Sobolev, C. Stodel, and J. Timár, Phys. Rev. C **77**, 044303 (2008).

[111] P.G. Thirolf, B.V. Pritychenko, B.A. Brown, P.D. Cottle, M. Chromik, T. Glasmacher, G. Hackman, R.W. Ibbotson, K.W. Kemper, T. Otsuka, L.A. Riley, H. Scheit, Phys. Lett. B **485**, 16 (2000).

[112] M.J. Strongman, A. Spyrou, C. R. Hoffman, T. Baumann, D. Bazin, J. Brown, P.A. DeYoung, J.E. Finck, N. Frank, S. Mosby, W.F. Rogers, G.F. Peaslee, W.A. Peters, A. Schiller, S.L. Tabor, and M. Thoennessen, Phys. Rev. C **80**, 021302(R) (2009).

[113] C.R. Hoffman, B.P. Kay, and J.P. Schiffer, Phys. Rev. C **89**, 061305(R) (2014).

[114] S. Bedoor, A.H. Wuosmaa, J.C. Lighthall, M. Alcorta, B.B. Back, P.F. Bertone, B.A. Brown, C.M. Deibel, C.R. Hoffman, S.T. Marley, R.C. Pardo, K.E. Rehm, A.M. Rogers, J.P. Schiffer, and D.V. Shetty, Phys. Rev. C **88**, 011304(R) (2013).

[115] C.R. Hoffman, M. Albers, M.Alcorta, S. Almaraz-Calderon, B.B. Back, S.I. Baker, S. Bedoor, P.F. Bertone, B.P. Kay, J.C. Lighthall, T. Palchan, R.C. Pardo, G. Perdikakis, K.E. Rehm, A.M. Rogers, D. Santiago-Gonzalez, C. Yuan, and J.P. Schiffer, Phys. Rev. C **88**, 044317 (2013).

[116] L. Chulkov, G. Kraus, O. Bochkarev, P. Egelho, H. Geissel, M. Golovkov, H. Irnich, Z. Janas, H. Keller, T. Kobayashi, G. Mtinzenberg, E Nickel, A. Ogloblin, A. Ozawa, S. Patra, A. Piechaczek, E. Roeckl, W. Schwab, K. Sümmerer, T. Suzuki, I. Tanihata, and K. Yoshida, Nucl. Phys. A **603**, 219 (1996).

[117] O.V. Bochkarev, L.V. Chulkov, P. Egelhof, H. Geissel, M.S. Golovkov, H. Irnich, Z. Janas, H. Keller, T. Kobayashi, G. Kraus, G. Müunzenberg, F. Nickel, A.A. Ogloblin, A. Ozawa, A. Piechaczek, E. Roeckl, W. Schwab, K. Sümmerer, T. Suzuki, I. Tanihata, K. Yoshida, Eur. Phys. J. A **1**, 15 (1998).

[118] J.W. Negele, Phys. Rev. C **1**, 1260 (1970).

[119] L. Ray, Phys. Rev. C **20**, 1857 (1979).

[120] J.A. Tostevin, D. Bazin, B.A. Brown, T. Glasmacher, P.G. Hansen, V. Maddalena, A. Navin, and B.M. Sherrill Phys. Rev. C **66**, 024607 (2002).

[121] A. Gade, D. Bazin, C.A. Bertulani, B.A. Brown, C.M. Campbell, J.A. Church, D.C. Dinca, J. Enders, T. Glasmacher, P.G. Hansen, Z. Hu, K.W. Kemper, W.F. Mueller, H. Olliver, B.C. Perry, L.A. Riley, B.T. Roeder, B.M. Sherrill, J.R. Terry, J.A. Tostevin, and K.L. Yurkewicz Phys. Rev. C **71**, 051301(R) (2005).

[122] K.L. Yurkewicz, D. Bazin, B.A. Brown, J. Enders, A. Gade, T. Glasmacher, P.G. Hansen, V. Maddalena, A. Navin, B.M. Sherrill, and J.A. Tostevin Phys. Rev. C **74**, 024304 (2006).

[123] J.A. Tostevin and A. Gade, Phys. Rev. C **90**, 057602 (2014).

[124] Zs. Vajta, Zs. Dombrádi, Z. Elekes, T. Aiba, N. Aoi, H. Baba, D. Bemmerer, Zs. Fülöp, N. Iwasa, Á. Kiss, T. Kobayashi, Y. Kondo, T. Motobayashi, T. Nakabayashi, T. Nannichi, H. Sakurai, D. Sohler, S. Takeuchi, K. Tanaka, Y. Togano, K. Yamada, M. Yamaguchi, and K. Yoneda Phys. Rev. C **91**, 064315 (2015).